

DIFFUSION OF RECEPTORS ON MACROPHAGE
PLASMA MEMBRANES

CHARACTERIZING THE LATERAL DIFFUSION OF TLR2
AND CD14 RECEPTORS ON MACROPHAGE
PLASMA MEMBRANES

By

SARA MAKAREMI, M.E.Sc

A Thesis

Submitted to the School of Graduate Studies

in Partial Fulfilment of the Requirements

for the Degree

Doctor of Philosophy

McMaster University DOCTOR OF PHILOSOPHY (2019) Hamilton, Ontario
(Biomedical Engineering)

TITLE: Characterizing the Lateral Diffusion of TLR2 and CD14 Receptors on
Macrophage Plasma Membranes

AUTHOR: Sara Makaremi, M.E.Sc (University of Western Ontario)

SUPERVISORS: Dr. Jose Moran-Mirabal and Dr. Dawn M.E. Bowdish

NUMBER OF PAGES: xiii 150

LAY ABSTRACT

The immune system is highly dependent on a specialized subset of white blood cells known as macrophages that are capable of clearing damaged and dead cells as well as a wide range of invading micro-organisms. Specific receptor proteins present on the membrane of macrophages are involved in the recognition of particles and subsequent signaling to recruit other immune cells or to promote healing and wound repair. To date, a variety of fluorescence-based microscopy methods have been used to study the dynamics of cell membrane components. The mobility of several membrane receptors in macrophages has been studied using microscopy techniques, which have provided valuable insights into their function. However, there is still insufficient information about the behavior of two key receptors (TLR2 and CD14) that participate in signaling in response to bacterial products. This thesis aims to answer three major questions with regard to receptor mobility (*i.e.*, diffusion) within macrophage membrane: 1) Which type of fluorescence-based microscopy technique is more suitable for measuring the mobility of TLR2 and CD14 receptors on macrophage membranes? 2) What is the impact of different surface topographies on TLR2 diffusion in adhered macrophages, as well as cell shape, and the ability of macrophages to internalize particles? 3) Does aging alter TLR2 mobility in the membrane of macrophages? The following chapters provide detailed answers to these questions. In brief, we have demonstrated that TLR2 and CD14 diffusion measurements in adhered macrophages highly depend on the membrane section chosen. In addition, our results show that micro- and nanostructured surface topographies alter the shape of adhered macrophages and yield higher bacteria internalization, while the diffusion of TLR2 is not changed. When comparing macrophages derived from young and old mice, we find similar diffusion rate of TLR2 in macrophages of the two age groups.

ABSTRACT

Among the central constituents of the innate immune system are macrophages, which are known for phagocytosis or ‘eating’ foreign particles or pathogens. Macrophages express several cell-surface proteins including transmembrane and membrane-anchored receptors, which play a vital role in their response to pathogenic stimuli. The plasma membrane is a highly fluid and dynamic environment, which facilitates the diffusion of lipids and proteins within the plane of the membrane. This study aims to measure the lateral diffusion of two types of plasma membrane receptors on macrophages, toll-like receptor II (TLR2) and cluster of differentiation 14 (CD14), to answer three main research questions: 1) Which type of fluorescence-based microscopy techniques is best suited for measuring the lateral diffusion of TLR2 and CD14 on macrophage plasma membrane? 2) Does culturing macrophages on different surface topographies impact the diffusion of TLR2 in the plasma membrane and its pro-inflammatory response, along with morphological changes? 3) Does aging alter the lateral diffusion of TLR2 in the plasma membrane of macrophages? To date, a variety of fluorescence-based methods have been developed to study the dynamics of cell membrane constituents. These techniques are based on either ensemble or single particle measurements. We have used single particle tracking methods to track the mobility of fluorescently labeled membrane receptors on murine bone marrow-derived macrophages. Total internal reflection fluorescence microscopy (TIRF) was used to visualize and capture the dynamics in live cells. Using a custom routine algorithm we detected, localized, and tracked the particles to calculate their diffusion coefficient, extracted from the mean-squared displacement as the most common measure of diffusion. We also measured the diffusion coefficient using an ensemble-based technique known as Raster Image Correlation Spectroscopy (RICS) with a confocal laser-scanning microscope. The use of confocal eliminates the out-of-focus signal and enables measurements that are confined to a narrow plane in the cell. Also, the ability of RICS to separate the slow and immobile fractions of particles makes it possible to detect heterogeneities in diffusion. To our knowledge, this is the first study that has utilized both SPT and RICS to directly compare receptors’ diffusion in different membrane sections. Moreover, this is the first study that has examined the diffusion of receptors on macrophages adhered to different surface topographies, and the first that has investigated the receptors’ diffusion in young and old macrophages.

ACKNOWLEDGEMENTS

First and foremost, I would like to express my sincerest gratitude and appreciation to my supervisors, Dr. Jose Moran-Mirabal and Dr. Dawn Bowdish for providing me with the opportunity to pursue doctoral studies in the school of Biomedical Engineering at McMaster University. I would like to thank them for their exceptional supervision, tremendous support and encouragement, and their excellent guidance through the past five years. Working in their research groups has been an invaluable learning experience. My sincere gratitude also goes to my supervisory committee member Dr. Kathryn Grandfield for her insightful suggestions and comments during our annual meetings.

My sincere appreciation goes to Dr. Michelle Digman, Dr. Suman Ranjit, and Dr. Enrico Gratton for their supervision and professional training during my internship at the laboratory of fluorescence dynamics (LFD), University of California Irvine. The LFD workshop provided me with firsthand observation of the most advanced fluorescence microscopy techniques for live cell imaging. I am also thankful to Dr. Harald Stover and Dr. Ray Truant for providing access to the confocal microscopes at McMaster and Dr. Noori Akhtar-Danesh for assisting with statistical interpretation of the results.

I have had the privilege of working alongside many inspiring students at McMaster. I owe much gratitude to Markus Rose who taught me the fundamentals of diffusion in physics as well as the mathematics and principles of single particle tracking. I would also like to thank Mouhanad Babi for his technical advice on microscopy image processing, and for helping create the graphic design of our cover image featured on *Advanced Materials Interfaces* (vol. 6, no. 21, 2019). I further acknowledge and appreciate the hard work and devotion of Helen Luu, Justin Boyle, Dr. Yujie Zhu, Christine Cerson, and Daniel Levin to our collaborative project.

My gratitude extends to all other past and present members of my research groups: Dr. Kyle Novakowski, Dr. Dessi Loukov, Jessica Breznik, Dr. Christian Schulz, Dr. Kevin Saem, Dr. Ayodele Fatona, Xuiping Ding, Taylor Stimpson, Peter Nalivayko, Elnur Shayhidin, Dr. Janine Strehmel, Grace Teskey, Mohammad Malik, Dr. Allison Kennedy, Erica De Jong, Jessica Wallace, and Dr. Pat Schenck. Thank you all for your valuable friendship. It was an unforgettable experience to work with and learn from you.

To all my friends outside the research labs, thank you for your kindness and support during the past five years. Your friendship has made this journey so much more meaningful.

Last but not least, I wish to express my heartfelt thanks to my family for their endless love, support, and patience, for which I am eternally grateful. To my parents, thank you for supporting and encouraging me to reach my goals. To my brother, thank you for always reminding me the importance of determination and perseverance. To my husband, thank you for your kindness and support, as well as your exceptional patience and understanding. This journey would not have been possible without your constant encouragement and inspiration.

In memory of my uncle, *Morteza*

I wish you could see how far I have come.
I know you would be proud.

Table of Contents

Chapter 1.....	1
1.1 Biomembranes.....	2
1.1.1 <i>Membranes in Life</i>	2
1.1.2 <i>Structure and Function of the Plasma Membrane</i>	2
1.1.3 <i>Diffusion — the “Dance” in the Plasma Membrane</i>	5
1.2 Methods to Measure Diffusion.....	8
1.2.1 <i>Fluorescence Recovery After Photobleaching</i>	8
1.2.2 <i>Fluorescence Correlation Spectroscopy</i>	11
1.2.3 <i>Image Correlation Spectroscopy</i>	17
1.2.4 <i>Single Particle Tracking</i>	37
1.3 New Developments and Perspectives	48
1.4 Macrophages	52
1.4.1 <i>Origins and Phenotypes</i>	52
1.4.2 <i>Phagocytosis</i>	53
1.4.3 <i>Plasma Membrane Receptors</i>	54
1.5 Research Objectives	56
1.6 Overview	56
1.7 References	58
Chapter 2.....	74
2.1 Introduction.....	75
2.2 Experimental Section.....	77
2.2.1 <i>Cell Culture</i>	77
2.2.2 <i>Fluorescence Staining</i>	77
2.2.3 <i>Single Particle Tracking (SPT)</i>	78
2.2.4 <i>Raster Image Correlation Spectroscopy (RICS)</i>	79
2.3 Results.....	81
2.3.1 <i>Single Particle Tracking</i>	81
2.3.2 <i>Raster Image Correlation Spectroscopy</i>	84
2.4 Discussion	86
2.5 Conclusion.....	88
2.6 Reference	90
Chapter 3.....	94
3.1 Introduction.....	95
3.2 Experimental Section.....	96
3.2.1 <i>Substrate Preparation</i>	96
3.2.2 <i>White Light Interferometry</i>	97
3.2.3 <i>Water Contact Angle Measurements</i>	97
3.2.4 <i>Macrophage Culture</i>	97
3.2.5 <i>Scanning Electron Microscopy</i>	98
3.2.6 <i>Epifluorescence Imaging</i>	98
3.2.7 <i>Fractal Analysis</i>	99
3.2.8 <i>Streptococcus pneumoniae Internalization Assay</i>	99
3.2.9 <i>Interleukin-6 (IL-6) Enzyme-linked Immunosorbent Assay (ELISA)</i>	100
3.2.10 <i>Diffusion Measurements</i>	100
3.2.11 <i>Cell Viability Test</i>	101
3.2.12 <i>Statistical Analysis</i>	101

3.3 Results	102
3.3.1 Surface Characterization	102
3.3.2 Cell Morphology	103
3.3.3 <i>Streptococcus pneumoniae</i> Internalization Assay	106
3.3.4 IL-6 Cytokine Secretion	108
3.3.5 Membrane Diffusion – TLR2	108
3.4 Discussion	110
3.5 Conclusion	113
3.6 References	114
Chapter 4.....	118
4.1 Introduction	119
4.2 Experimental Section	120
4.2.1 Macrophage Culture	120
4.2.2 Polystyrene Beads/Bacterial Internalization Assay	121
4.2.3 Cell Staining and Counting.....	122
4.2.4 Diffusion Measurements.....	122
4.2.5 Statistical Analysis	123
4.3 Results	123
4.3.1 Internalization Assay.....	123
4.3.2 TLR2 Diffusion	124
4.4 Discussion	127
4.5 Conclusion	128
4.6 References	129
Chapter 5.....	133
5.1 Summary and Conclusions	134
5.2 Future Directions	135
Supporting Information for Chapter 2	137
Supporting Information for Chapter 3	144

List of Abbreviations

AFM	Atomic force microscopy
AP-2	Adaptor protein
APCs	Antigen presenting cells
ARICS	Arbitrary-region raster image correlation spectroscopy
ATCC	American Type Culture Collection
BCL2	B cell CLL/lymphoma 2
BMDM	Bone marrow-derived macrophages
CCL18	C-C motif chemokine ligand 18
CD	Cluster density
CD14	Cluster of differentiation 14
CHO	Chinese hamster ovary
CLSM	Confocal laser-scanning microscopy
CPD	Cumulative probability distribution
DA	Degree of aggregation
DAMPs	Damage associated molecular patterns
DAPI	4,6-diamidino-2-phenylindole dihydrochloride
Dkk1	Dickkopf1
ECM	Extracellular matrix
ELISA	Enzyme-linked immunosorbent assay
EMCCD	Electron multiplying charge couple device
FBS	Fetal bovine serum
FCFS	Fluorescence cross-correlation spectroscopy

FCS	Fluorescence correlation spectroscopy
Fc γ R	Fc γ receptors
FDA	Fractal dimension for the area
FDP	Fractal dimension perimeter
FRAP	Fluorescence recovery after photobleaching
GPI	Glycosylphosphatidylinositol
HILO	Highly inclined and laminated optical
HSCs	Hematopoietic stem cells
ICCS	Image cross-correlation spectroscopy
ICS	Image correlation spectroscopy
IFN- γ	Interferon-gamma
IgG	Immunoglobulin G
IL-4	Interleukin-4
ITIR-FCS	Imaging total internal reflection fluorescence correlation spectroscopy
LFA-1	Lymphocyte function-associated antigen 1
LPS	Lipopolysaccharide
LRP6	Low-density-lipoprotein-receptor related protein 6
LTA	Lipoteichoic acid
MARCO	Macrophage receptor with collagenous structure
mEGFP	Monomeric enhanced green fluorescence protein
MOI	Multiplicity of infection
MSD	Mean-squared displacement
NF- κ B	Nuclear factor kappa B
NSOM	Near-field scanning optical microscopy

PAMPs	Pathogen associated molecular patterns
PCL	Poly(ϵ -caprolactone)
PDMS	Poly(dimethylsiloxane)
PICS	Particle image correlation spectroscopy
PLA	Poly(lactic acid)
PRRs	Pattern recognition receptors
PS	Polystyrene
PSF	Point spread function
PTFE	Poly(tetrafluoroethylene)
P-V	Peak-to-valley
Qdot	Quantum dot
RFU	Relative fluorescence unit
RICS	Raster image correlation spectroscopy
RMS	Root mean square
ROI	Region of interest
SAD	Sum-absolute difference
sCMOS	Scientific complementary metal-oxide-semiconductor
SEM	Scanning electron microscopy
SIM	Structured illumination microscopy
smFRAP	Single molecule fluorescence recovery after photobleaching
SPT	Single particle tracking
STED	Stimulated emission depletion
STICS	Spatio-temporal image correlation spectroscopy

tBID	Truncated BH3-interacting domain
TCR	T cell receptor
TICS	Temporal image correlation spectroscopy
TIRF	Total internal reflection fluorescence
TLR	Toll-like receptors
TNF α	Tumor necrosis factor alpha
VSV-G	Vesicular stomatitis virus-G
WCA	Water contact angle
WLIM	White light interferometry microscopy
XTC	<i>Xenopus laevis</i> tissue culture
ZMWs	Zero mode waveguides
2c2f lsFCS	Dual color dual-focus line-scanning fluorescence correlation spectroscopy
50S	50 nm structured SiO ₂

DECLARATION OF ACADEMIC ACHIEVEMENT

This thesis is written based on three research studies conducted for publication in peer-reviewed journals, as well as a review section for consideration as a book chapter. Chapter 1 (Section 1.1-1.3) has been submitted to *Springer* for publication as part of a book and is currently under review. Chapter 2 is prepared for submission to the journal *Communications Biology*. The study described in Chapter 3 has been published (*Advanced Materials Interfaces*, vol. 6, no. 21, 2019). Chapter 4 is part of a manuscript in preparation for publication.

I hereby declare that I have been the primary contributor to the experimental design, analysis, interpretation, and manuscript preparation for the majority of the work contained in this thesis, in consultation from Dr. Jose Moran-Mirabal and Dr. Dawn Bowdish. I would like to gratefully acknowledge the contributions of all my colleagues and their collaborative work for our findings presented in this thesis:

Chapter 2: Markus Rose wrote the Python program for tracking single molecules, and assisted with data analysis. Dr. Suman Ranjit and Dr. Michelle Digman assisted with interpretation of the data obtained from SimFCS software.

Chapter 3: Helen Luu performed the contact angle measurements, fractal analysis, phagocytosis assay, and ELISA. Justin P. Boyle imaged the fluorescently stained cells with bacteria. Dr. Yujie Zhu performed the processing of the white light interferometry data. Christine Cerson assisted with cell counting.

Chapter 4: Christine Cerson assisted with quantification of beads and bacteria. Elnur Shayhidin helped with fluorescence staining of bacteria.

Chapter 1

Introduction and Research Aims

This chapter reviews both conventional and recently developed fluorescent-based microscopy techniques to study the dynamics of membrane components in live cells. In addition, it provides an introduction to macrophages and their plasma membrane receptors. Finally, the research questions addressed in the following chapters, and an overview of this thesis are introduced.

The background information provided in this chapter (Section 1.1-1.3) is submitted for consideration as a book chapter and is currently under review for the book titled: “Handling, Measurement, and Visualization Tools for Single Cell Analysis”, Springer, editors: Joseph, M.K. Irudayaraj, and Jose M. Moran-Mirabal.

1.1 Biomembranes

1.1.1 Membranes in Life

The cell, the fundamental unit of life, is separated from its surrounding environment by a membrane envelope known as the plasma membrane; through this barrier it takes up nutrients and excretes waste to sustain the essential dynamics of cellular processes. The plasma membrane serves as a semi-permeable barrier between two aqueous environments, the cell interior (cytosol) and the extracellular environment, and has numerous other functions crucial to cellular homeostasis, such as maintaining specific pH and ionic conditions inside the cell, mediating transport into and out of the cell, or transducing signaling cascades triggered by binding events at the membrane [1]. The essential role of the plasma membrane is evident as membrane disruption and influx of extracellular materials into the cytosolic environment precedes cell death [1].

Eukaryotic cells in particular, are highly compartmentalized and have different organelles in charge of specific functions. Each organelle is bound within a membrane, thus confining the specialized metabolic pathways related to each organelle. Biological membranes have a similar structure although they may have major differences in their composition, depending on which cell or organelle they originate from.

1.1.2 Structure and Function of the Plasma Membrane

The basic structure of the plasma membrane is that of a bilayer composed of a mixture of phospholipids, where the hydrophilic phosphate-linked head groups face the aqueous environment, and the hydrophobic hydrocarbon chains face the lumen of the bilayer (Figure 1.1). The membrane bilayer is in principle two molecules thick (~5 nm) and spans a continuous surface area of hundreds of square micrometers [2]. The first documented description of a bilayer arrangement for lipids in the plasma membrane dates back to 1925 when two Dutch physicians, Gorter and Grendel, isolated membrane lipids from red blood cells and compared the area occupied by a monolayer of these lipids spread on a Langmuir trough with the average surface area of red blood cells [3]. Erythrocytes lack internal membranes and consequently they are the easiest source of pure plasma membrane. The area from Gorter and Grendel's lipid extract was found to

be twice the predicted value, leading to the conclusion that membranes are formed by lipid bilayers rather than monolayers [3].

Our current understanding of the structure and dynamics of the plasma membrane is framed by the well-known “fluid mosaic” model proposed by Singer and Nicholson in 1972 [4]. This model improved on the earlier “trilamellar” model of Danielli and Davson, proposed in 1935 [5], that described a plasma membrane with a central fluid layer of disordered lipid-like molecules sandwiched by a bilayer of ordered phospholipids. In the “fluid mosaic” model, there is no core layer and the lipid environment is described as fluid and homogenous, with proteins that are free to diffuse laterally within the plane of the membrane [4]. Subsequent studies showed that the plasma membrane is not homogenous and the diffusion of proteins is much slower than predicted by Singer and Nicholson. The “fluid mosaic” model was improved upon in 1988 by Meer and Simons [6], who proposed the “lipid raft” model in which groups of lipids arranged into cholesterol- and sphingolipid-rich areas create semisolid state domains, termed lipid rafts [7]. These rafts are formed transiently in the plasma membrane, and their nanoscale sizes are below the resolution of traditional optical techniques [7].

The plasma membrane of eukaryotes consists of four major classes of phospholipids: phosphatidylcholine, phosphatidylethanolamine, phosphatidylserine, and sphingomyelin. The distribution of these phospholipids in the two halves of the plasma membrane is asymmetrical (Figure 1.1). The outer leaflet mostly contains phosphatidylcholine and sphingomyelin, whereas phosphatidylethanolamine and phosphatidylserine are mainly found in the inner leaflet. Phosphatidylinositol is also present in the inner leaflet, but at lower abundance. The negatively charged head groups of phosphatidylserine and phosphatidylinositol in the inner leaflet result in a negative charge on the inner half of membrane which faces the cytosol (Figure 1.1) [8]. During the life of a cell the lipid distribution continuously changes as the cell undergoes different activation states [9]. The “flip-flop” of a phospholipid happens between the two halves of the membrane when the polar part of a phospholipid can pass through the hydrophobic interior of the membrane and flips over to the other leaflet [10]. This process is called transverse diffusion and is significantly slower than the lateral diffusion of lipids (Section 1.1.3).

Phospholipids are synthesized on the surface of the smooth endoplasmic reticulum and are rapidly distributed to the membranes throughout the cell [1]. Removal of membrane segments in processes such as endocytosis is balanced by fusion of vesicles that recover and replenish the lost membrane [1]. Any empty space or hole in the plasma membrane is occupied and sealed spontaneously by the neighboring lipids that associate with one another to maintain the energetically favored organization of the lipid bilayer. This enables the membrane to fuse immediately after vesicle formation, phagocytosis, and related processes [1]. An optimal surface pressure of $\sim 30 \text{ mN}\cdot\text{m}^{-1}$ is maintained in the cell membrane by controlling the lipid packing density [2]. Any compression and tension above the optimal packing of lipids that may excessively decrease or increase the lipid spacing is energetically unfavorable. This mechanism prevents rupture due to osmotic swelling and buckling due to compression, making the membrane a highly resilient structure to environmental stressors [2].

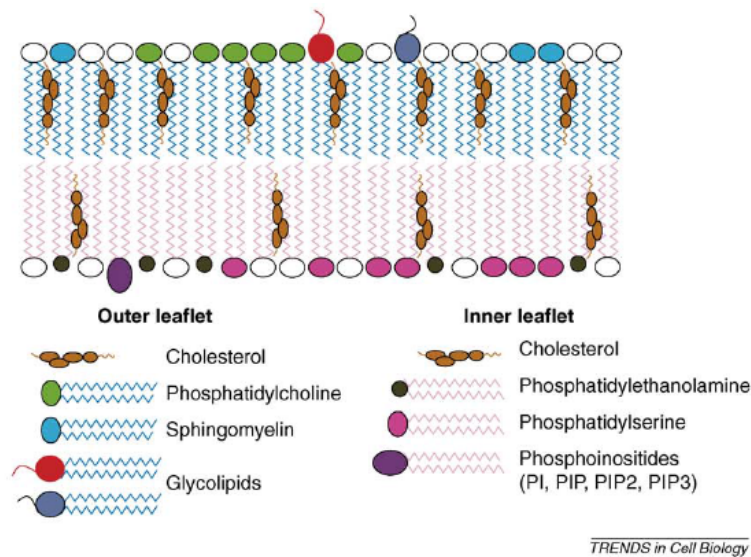


Figure 1.1 Major components of plasma membrane and their asymmetrical distribution; top layer facing the extracellular matrix, bottom layer facing the cytosol [2].

In addition to phospholipids, the plasma membrane contains glycolipids and cholesterol. Glycolipids reside in the outer leaflet and constitute approximately 2% of lipids of most plasma membranes in eukaryotic cells [8]. Cholesterol, on the other hand, is found in abundance with molar concentrations comparable to those of phospholipids. It is a major constituent of animal cell membranes and is mostly present in the outer

leaflet. Cholesterol is from a family of organic compounds containing multiple fused carbon rings known as steroids, and is highly hydrophobic. It plays a pivotal role in the structure of plasma membrane, where it modulates its fluidity and permeability by controlling the lateral mobility and the packing of fatty acid chains [8].

Integral and peripheral membrane proteins constitute approximately 50% of the cross-sectional area of the plasma membrane [2]. Integral proteins, also known as transmembrane proteins, span the full width of the phospholipid bilayer and contain domains that protrude from the membrane on both sides, reaching the aqueous environments. In contrast, peripheral membrane proteins lack hydrophobic domains and do not penetrate the bilayer. Instead, their polar regions interact with the polar heads of phospholipids or the protruding domains of integral proteins [1]. These proteins can be dissociated from the membrane using polar reagents, extreme pH or high salt concentrations that screen electrostatic interactions but do not disrupt the phospholipid bilayers, and are soluble in aqueous buffers [8]. The distribution of proteins in the inner and outer leaflets is also asymmetrical. Some types of proteins freely diffuse through the membrane, while others appear to be anchored to a specific region of the membrane. In addition to lipids and proteins, the plasma membrane of many cells contains carbohydrates that act as recognition sites for other cells and molecules. These carbohydrates are bound (covalently) to the protruding surface of lipids (glycolipids) and proteins (glycoproteins) [1].

All biological membranes, from different cells or organelles, have a similar structure although they may have major differences in their lipid composition. Phospholipids can greatly differ in their acyl chain length, degree of unsaturation (double bonds) in their acyl chain, and the polar head groups present. Additionally, cholesterol content (up to 25% of all lipid content) can vary between different biological membranes [1]. Despite these differences in composition, biological membranes share similar diffusive behavior.

1.1.3 Diffusion — the “Dance” in the Plasma Membrane

Membrane-residing species are highly mobile and have a heterogeneous distribution along and across the membrane bilayer. Although phospholipids and proteins do not move at an appreciable rate between the two halves of the bilayer, they experience

significant lateral diffusion along the plane of the plasma membrane. Frye and Edidin reported the first evidence of diffusion in the plasma membrane in 1970 [11], which provided support for the “fluid mosaic” model. They analyzed the distribution of membrane proteins on a human-mouse cell hybrid after fusing the two cells. Fluorescently labeled antibodies specific to proteins of human and mouse origin were used to distinguish the source of each protein. After incubation at 37°C, both protein types were completely intermixed over the cell surface, indicating that they diffused freely within the plasma membrane [11].

The diffusion rates of lipids and proteins in reconstituted artificial bilayers are typically higher than those observed in biological membranes of comparable lipid composition, often by more than an order of magnitude [12]. This discrepancy indicates that the diffusion of membrane proteins and lipids is not completely free in the plane of the bilayer. Diffusion is not only controlled by physical barriers such as the cortical cytoskeleton [13,14] and membrane “crowding” with proteins [15], but also by electrostatic interactions between charged components [16] and the overall heterogeneous nature of membrane composition. These barriers to free diffusion can be classified into three main groups: physical obstacles, electrostatic interactions, and partitioning phenomena that preferentially retain or exclude certain membrane components [17]. In plasma membranes, these barriers are highly dynamic and constantly remodeled to allow or limit diffusion as required by the cell. Trimble *et al.* have comprehensively discussed the diffusion barriers in the plasma membrane and interested readers are referred to their review for a detailed description of these mechanisms [17].

Cytoskeleton: The membrane-associated cortical cytoskeleton can alter not only the lateral diffusion of transmembrane proteins in the inner leaflet, but can also limit the mobility of outer leaflet lipid-anchored proteins [17–19]. The “picket fence” model [20] of the plasma membrane describes this type of diffusion barrier by the cytoskeleton-anchored “fences” and tethered proteins to the actin mesh as “pickets” that create confinement zones or “corrals” in the membrane (Figure 1.2-A). These barriers are not permanent and are continuously rearranged as the cytoskeleton is remodeled.

Membrane-membrane junctions: The areas where two separate membranes are in contact with each other can restrict the diffusion of proteins and lipids. This can be observed in

tight junctions and the sites of contact between membranes of organelles [6,21]. For instance, the endoplasmic reticulum generates contact with the plasma membrane and the membranes of other organelles, which in turn impacts the free diffusion of membrane proteins within each membrane (Figure 1.2-B) [22–24].

Extracellular matrix: Interactions of membrane components with the extracellular matrix (ECM) can also impede the lateral diffusion in the plasma membrane. This type of diffusion barrier is frequently reported for integrins that bind tightly to ECM proteins (Figure 1.2-C) [25].

Protein clusters: Large and relatively immobile clusters of membrane proteins and lipids can block the passage of diffusing components (Figure 1.2-D). Molecular aggregates trapped in the corrals formed by the picket fences can act as slow moving islands and are obstacles to free diffusion of monomeric proteins or lipids.

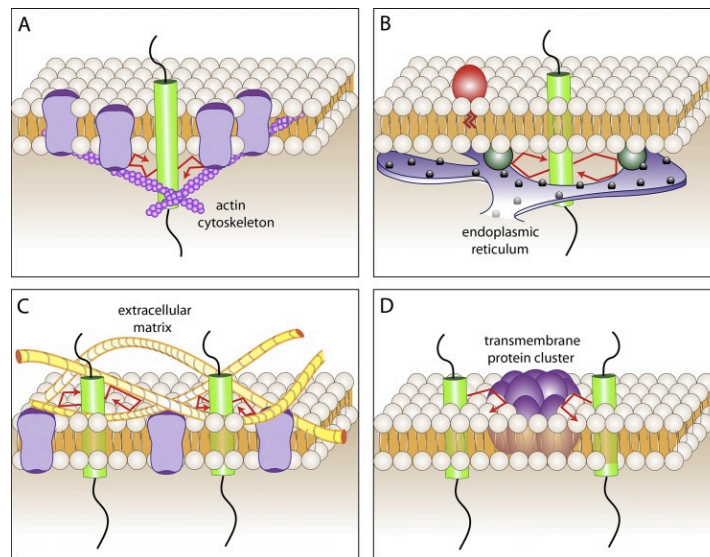


Figure 1.2 Illustration of physical barriers to the diffusion of membrane proteins and lipids. A) cortical actin cytoskeleton “fences” and transmembrane proteins (purple) tethered to actin as “pickets” can inhibit diffusion; B) contact between plasma membrane and the membrane of endoplasmic reticulum (studded purple) can block the diffusion of proteins in either membranes; C) extracellular matrix components such as fiber meshes (yellow) can impede diffusion; D) large immobile clusters of proteins (purple) or lipids can block the passage of diffusing molecules. Green cylinders represent freely mobile transmembrane proteins while the purple ones in A, C, and D are relatively immobile [17].

In addition to physical barriers, *electrostatic interactions* can also impede free diffusion in the membrane. Proteins and lipids of like charges are repelled while opposite charges are

attracted [16] (Figure 1.3-A). The presence of a charged immobile protein can deflect or slow down the diffusion of mobile molecules. Moreover, *hydrophobic interactions* can result in partitioning of proteins into saturated lipid- or cholesterol-rich domains, known as “rafts”, which can hinder diffusion (Figure 1.3-B) Membrane sites with *high curvature*, such as the tip of a filopodia, can also alter the diffusion of proteins and lipids by changing the surface potential. The reduced packing of the convex surface in the outer leaflet can expose hydrophobic regions, while the inner leaflet is tightly packed [9] (Figure 1.3-C). In addition, *hydrophobic mismatch* in the membrane where the length of acyl chains is significantly different from the size of transmembrane proteins can restrict the diffusion of certain proteins into specific areas of the membrane (Figure 1.3-D) [9,17].

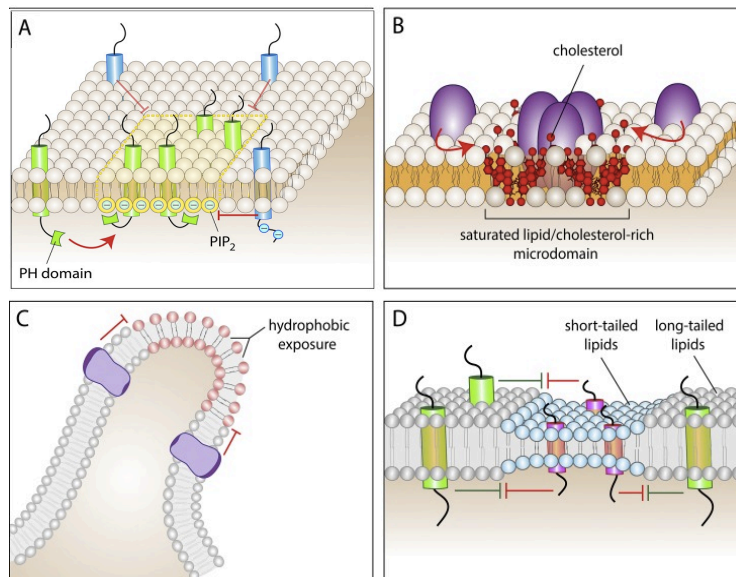


Figure 1.3 Schematic illustration of mechanisms that can impede diffusion of membrane proteins and lipids. A) attraction (blue) and repulsion (green) of charged proteins, B) partitioning of proteins into saturated lipid- or cholesterol-rich (red) domains, C) sharp curvature in the membrane causes crowding in the inner leaflet and spacing in the outer layer that can alter diffusion, D) membrane sites with short acyl chains (blue) accommodate proteins with shorter transmembrane domains (pink) and exclude proteins that are longer. This hydrophobic mismatch can restrict access of proteins or lipids into certain areas [17].

1. 2 Methods to Measure Diffusion

1.2.1 Fluorescence Recovery After Photobleaching

Fluorescence recovery after photobleaching (FRAP) is conventionally used as an ensemble method to measure the diffusion of lipids and proteins in biological and

biomimetic membranes. It is a perturbation-based technique that uses a brief intense excitation to irreversibly photobleach fluorophores in a designated small area. By monitoring the fluorescence recovery over time, the diffusion coefficient and the mobile fraction of the fluorescently tagged species can be determined. The recovery rate depends on both the diffusion of fluorescent molecules and potential binding and unbinding events within the region of interest (ROI). The constant turnover of proteins within a cell allows bleached fluorescent proteins to be replaced by newly recruited ones, leading to the recovery of fluorescence. FRAP measurements are only reliable for instances where the membrane does not exhibit dynamic protrusions and the cell does not undergo significant displacement over the length of the experiment. Moreover, the biological system under study should be at equilibrium before photobleaching.

Two important parameters accessible by FRAP measurements are the mobile fraction and half-time of recovery. The mobile fraction (F_M) is the proportion of bleached molecules that are replaced by their fluorescent counterparts during the recovery period. As a result, the mobile fraction can be calculated from the ratio of fluorescence intensity at the end of the time-lapse (F_∞) and the initial intensity ($F_{Initial}$) before perturbation, corrected by the experimental bleaching (F_0). Freely diffusing proteins or lipids have typical mobile fractions of $\sim 100\%$. If binding occurs or diffusion is hindered, the theoretical value of 100% recovery cannot be achieved in practice and the recovery reaches a plateau below this value by the end of the time frame of the experiment (Figure 1.4-B). Recovery values $> 100\%$ are indicative of growth of the membrane under study or directed transport into the observation volume. The recovery rate depends on the size of the biological system under observation and the stability of the interactions with large or fixed proteins [26].

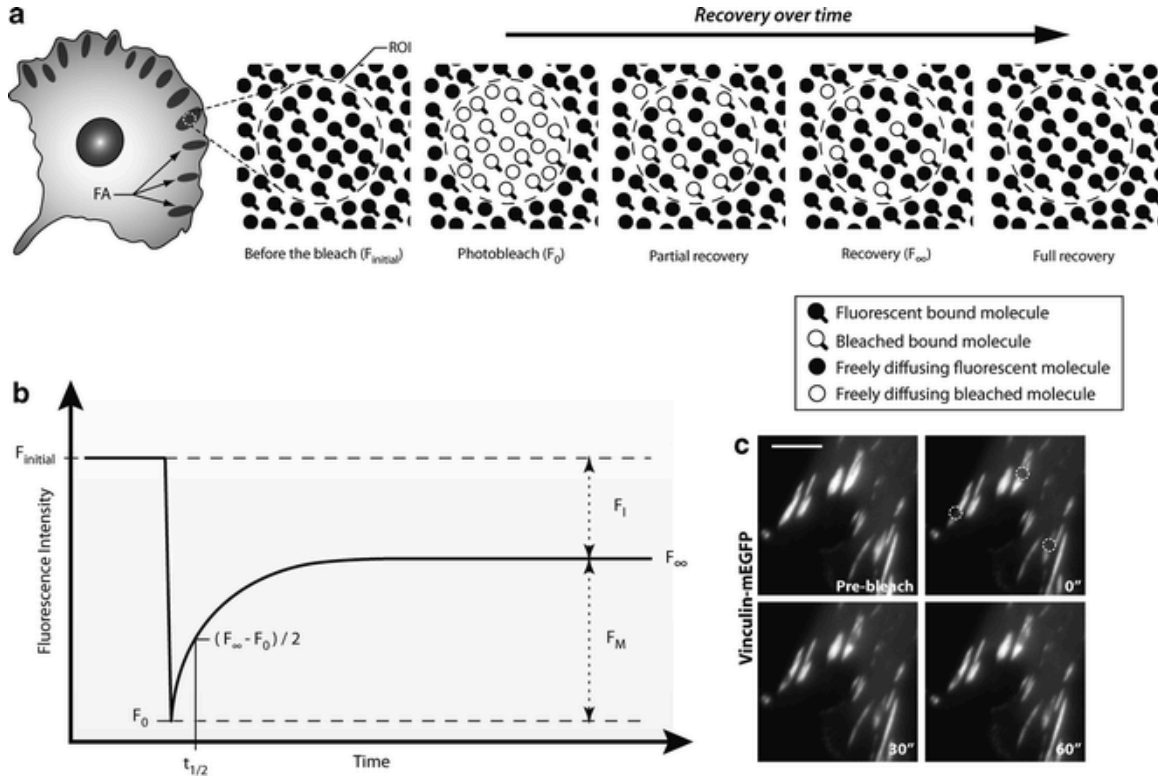


Figure 1.4 A) Schematic representation of a FRAP experiment on a focal adhesion of a cell, B) plot of fluorescent intensity as a function of time and the important parameters that can be used to calculate diffusion, C) FRAP experiment on a focal adhesion of NIH 3T3 cells transiently expressing vinculin-mEGFP. Dashed circles denote bleached areas at $t = 0$. Scale bar = $5 \mu\text{m}$ [27].

The half-time of recovery ($t_{1/2}$) is defined as the time required for the fluorescence to reach half of its maximum recovery intensity and can be used to calculate the diffusion coefficient. The experimental data is first fitted using a simple exponential equation:

$$F_t = F_M(1 - e^{-\tau t}). \quad (1.1)$$

Substitution of F_t with $\frac{1}{2}F_M$ results in the following expression for the half-time of recovery:

$$t_{1/2} = \frac{\ln(0.5)}{-\tau}. \quad (1.2)$$

The mathematical model for fitting fluorescence recovery in a uniformly bleached circular area has been described by Soumpasis [28], and interested readers are referred to

the original manuscript for its complete derivation. For a circular bleached area with diffusion-dominated recovery, the change in fluorescence with respect to time is described by:

$$F(t) = F(0) + C \exp\left(-\frac{2\tau_D}{t}\right) \left[I_0\left(-\frac{2\tau_D}{t}\right) + I_1\left(-\frac{2\tau_D}{t}\right) \right], \quad (1.3)$$

where $F(0)$ is the intensity immediately after bleaching pulse, C is the difference between the asymptotic value of the intensity at $t = \infty$ and $F(0)$, I_0 and I_1 are modified Bessel functions, and τ_D is the characteristic diffusion time given by:

$$\tau_D = \frac{\omega^2}{4D}, \quad (1.4)$$

where D is the diffusion coefficient, and ω is the radius of the bleached area. A similar analysis can be performed for two populations of diffusing molecules with two different diffusion coefficients [29].

FRAP has been utilized in various experiments on biological membranes for investigation of the diffusive behavior of proteins and lipids. A few examples of these studies include the lateral diffusion and exocytosis of membrane proteins in neurons [30] and diffusion of GFP-GPI expressed on the membrane of CHO-K1 [29]. Figure 1.4-C shows an example of a FRAP experiment on a focal adhesion plaque on NIH 3T3 murine fibroblast transiently expressing the monomeric enhanced green fluorescence protein (mEGFP). The circles indicate the vinculin-mEGFP bleached ROI at the onset of bleaching. The images captured at 30 and 60 seconds show that full recovery is not achieved within 1 min [27].

1.2.2 Fluorescence Correlation Spectroscopy

1.2.2-1 Single-Point FCS

Fluorescence Correlation Spectroscopy (FCS), also known as single-point FCS, measures diffusion by monitoring the fluctuations of fluorescence intensity that arise from labeled molecules within a fixed illumination volume. This technique measures the average duration of fluctuations at a very small point in space, typically corresponding to diffraction limited illumination in a two-dimensional plane. The recorded fluctuations can

be the result of blinking, changes in orientation or conformation of molecules, and translational diffusion in and out of the illumination volume. Single-point FCS provides high temporal resolution with data acquisition up to sub-nanosecond sampling from the molecular dynamics in a femtoliter volume [31]. However, minimizing the average number of molecules in the focal volume is essential so that the passage of molecules in and out of the volume creates large enough fluctuations in the intensity to be detectable. For a femtoliter observation volume a concentration of $\sim 10^{-10}$ M to $\sim 10^{-9}$ M molecules is typically used.

The theory of FCS is based on Poisson statistics. For random discrete events, the number of fluorophores in the observation volume can be described by a Poisson distribution, $P(n, N) = \frac{N^n}{n!} e^{-N}$, where $P(n, N)$ is the probability of having n fluorescent molecules present in the volume, knowing that N is the average number of molecules in the volume. The changes in the occupation number of the volume result in fluctuations in the fluorescence intensity. The rate of these changes depends on how fast the fluorescent molecules diffuse in and out of the volume, which can be determined from the amplitude and frequency distribution of the fluctuations. The fluorescence intensity at a given time $F(t)$ is compared with the intensity at a slightly later time $F(t+\tau)$ for delay times τ (Figure 1.5-A), typically in the range of 10^{-2} to 10^2 ms [31]. The same calculation for a range of delay times over the entire time sequence results in the autocorrelation function $G(\tau)$ (Figure 1.5-B), which contains information on the diffusion coefficient and the average number of fluorescent entities present in the observation volume. The derivation of the FCS autocorrelation function was originally described by Elson, Magde, and Webb [32], [33]. The normalized 2-dimensional autocorrelation function for the fluctuation of intensity signal is calculated by:

$$G(\tau) = \frac{\langle F(t).F(t+\tau) \rangle}{\langle F(t) \rangle^2} = \frac{\langle \delta F(t).\delta F(t+\tau) \rangle}{\langle F(t) \rangle^2} + 1, \quad (1.5)$$

where τ is the time lag (delay time relative to earlier time points) and the fluorescence fluctuation is calculated from $\delta F(t) = F(t) - \langle F(t) \rangle$. The angular brackets denote averaging intensities over the entire time sequence.

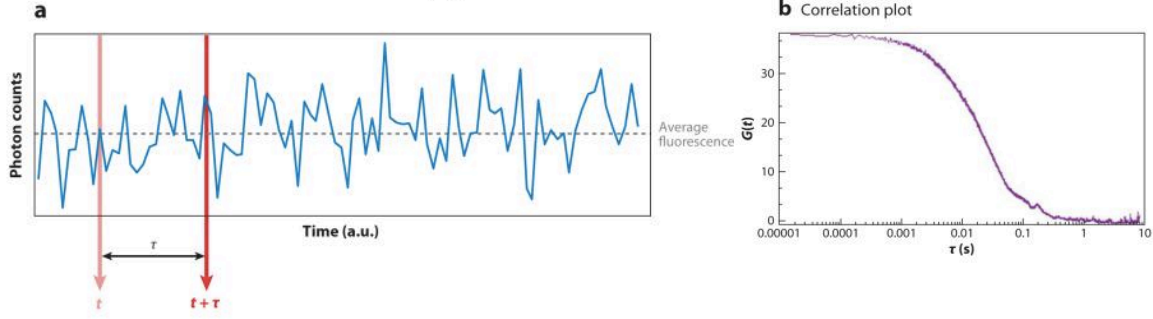


Figure 1.5 A) Fluorescence intensity fluctuations over time obtained from photon counts, the fluctuation at each time is correlated with the fluctuation at different time lags, B) Autocorrelation function $G(\tau)$ as a function of time lag is plotted for analysis of intensity fluctuations [34].

The change in the concentration of diffusing particles as a function of time in 3D is described by:

$$C(r, t) = \frac{1}{(4\pi Dt)^{3/2}} \exp\left(-\frac{r^2}{4Dt}\right), \quad (1.6)$$

where $C(r, t)$ is the concentration, which is proportional to the probability of finding a particle at position r at time t if the particle was at the origin $r = 0$ at time $t = 0$, propagating with diffusion coefficient D . If the concentration is sampled at one position such as in single-point FCS, the autocorrelation function of the fluorescence decays with a characteristic time that depends on the diffusion coefficient and the size of the illumination volume, as described by:

$$G(\tau) = G(0) \left(1 + \frac{\tau}{\tau_D}\right)^{-1} \left(1 + \left(\frac{\omega_0}{u}\right)^2 \frac{\tau}{\tau_D}\right)^{-1/2}, \quad (1.7)$$

where $G(0)$ is the amplitude at $\tau = 0$, the beam waist ω_0 and half-length u refer to the axial distance at which an ellipsoid illumination profile decreases to e^{-2} of its maximum value. The translational motion is characterized by the diffusion coefficient, which can be calculated using the known beam waist and the average duration of the fluctuation τ according to: $\tau_D = \omega_0^2/4D$, where τ_D is determined by fitting the analytical autocorrelation function to the experimental curve.

Using FCS it is possible to examine diffusion, chemical reactions, molecular rotations, conformational changes, blinking, fluorescence lifetime, and fluorescence resonance energy transfer [34]. Since the first FCS experiment by Magde, Elson, and Webb in 1972 on the binding of ethidium bromide to double-stranded DNA [32], FCS has been utilized in many membrane-related studies such as investigations of membrane

potential effect on IL-2 and IL-15 receptor mobility within the plasma membrane of T cells [35], diffusion of cell membrane proteins on primary lymphocytes [36], oligomerization of the poly(Q) proteins in COS-7 cells [37], and the molecular mobility of G protein-coupled receptors [38]. An important limitation of this technique is that it cannot provide information on the fluctuations that occur outside the illuminated spot. In addition, it provides limited information about processes that involve slower protein dynamics within large slowly moving structures, and simultaneous cell imaging cannot be performed [39].

1.2.2-2 Fluorescence Cross-Correlation Spectroscopy

Single-point FCS can be used to acquire and compare fluctuation data from more than one channel, a technique referred to as Fluorescence Cross-Correlation Spectroscopy (FCCS). For two independent channels measuring fluorescence signals F_i and F_j , equation (1.5) can be modified to account for intensity fluctuations of the two channels according to:

$$G_{ij}(\tau) = \frac{\langle \delta F_i(t) \cdot \delta F_j(t+\tau) \rangle}{\langle F_i(t) \rangle \cdot \langle F_j(t) \rangle}. \quad (1.8)$$

As described in Figure 1.6, only fluctuations that occur simultaneously in both channels due to the passage of the complex (containing a fluorescent element for each of the channels) in the illumination volume contribute to the cross-correlation.

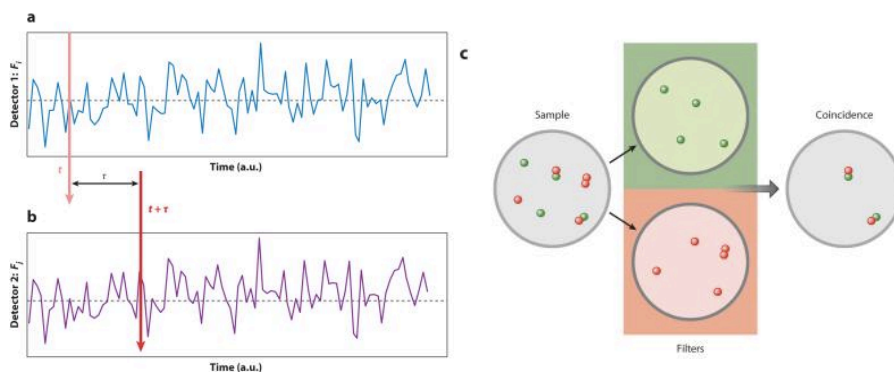


Figure 1.6 A) and B) fluctuations in the fluorescence intensity recorded by two independent detectors for C) a sample that contains fluorophores emitting in two colors, some of them forming a complex. Cross-correlation is determined by simultaneous occurrence of fluctuations in both channels as a result of the passage of the complex in the illumination volume [34].

FCFS has been applied in several investigations on the interactions of membrane components including diffusion properties of peptide-oligonucleotide complexes on the plasma membrane of PC12 cells [40], diffusion of membrane proteins and liposomes forming proteoliposomes [41], and interactions of B cell CLL/lymphoma 2 (BCL2) proteins with truncated BH3-interacting domain death agonist (tBID) on the mitochondrial membrane [42]. There are challenges associated with experiments using FCFS to evaluate membrane dynamics [43,44]. Long measurement times can lead to photobleaching of labeled molecules, and the membrane under study has to be stable with respect to the illumination volume to avoid distortions of the correlation curves. False positive cross-correlation can occur due to membrane movement, when fluctuations of two labeled molecules are correlated in the absence of any complex formation. These complications can be circumvented using scanning FCS, as described in the next section.

1.2.2-3 Scanning FCS

The major limitation of single-point FCS is that it contains only local information about fluctuations occurring inside the measured point. Consequently, scanning FCS was developed to add the missing spatial scale. In this method the illumination volume is moved in a periodic pattern (linear or circular) in the region of interest on the membrane with a scanning speed that allows capturing the molecules at almost the same point during successive scans. The intensity fluctuations recorded along the path can then provide spatial information about the dynamics. If molecules move away from their original location in a time frame comparable to the scanning period, then the intensity fluctuation for the initially recorded location decays between successive scans. The correlation of one point with the same point visited again in subsequent scans is called the carpet approach and its temporal resolution depends on the scanning period, which is typically on the order of a millisecond. In contrast, the correlation of adjacent points along the scanning path yields microsecond resolution and is called raster image correlation spectroscopy, described in Section 1.2.3-4.

The FCS methods described in previous sections can be combined to develop a dual-color dual-focus line-scanning fluorescence correlation spectroscopy (2c2f lsFCS) [45] that incorporates the advantages of the three FCS modalities. The use of two spectral

excitation and detection channels for scanning two lines simultaneously makes this technique insensitive to slow movements of the sample [45]. In addition, photobleaching is minimized using the line scanning approach as the illumination volume does not dwell on each spot for a long time and only crosses the membrane briefly (~ 2 ms) [45]. 2c2f lsFCS has been applied to quantify ligand and receptor concentrations and diffusion coefficients within cell membrane [45]. In the plasma membrane of living HEK293T cells, the interactions of Dickkopf1 (Dkk1) and Dickkopf2 (Dkk2) glycoproteins with their cognate receptor, low-density-lipoprotein-receptor related protein 6 (LRP6), have also been analyzed using 2c2f lsFCS. The autocorrelation and dual-focus cross-correlation functions obtained from each of the red and green channels (Figure 1.7) were used to quantify the diffusion coefficient and concentration of the LRP6-mCherry receptor and Dkk1-GFP, respectively. The receptor's diffusion coefficient was calculated to be $0.18 \pm 0.06 \mu\text{m}^2 \cdot \text{s}^{-1}$ with a concentration of $25 \pm 12 \mu\text{m}^{-2}$ (*i.e.*, area density in the membrane), while the receptor-ligand complex (GFP-LRP6-mCherry) was found to have a diffusion coefficient of $0.20 \pm 0.02 \mu\text{m}^2 \cdot \text{s}^{-1}$ with a concentration of $26 \pm 5 \mu\text{m}^{-2}$ in the membrane. This information from unbound and bound proteins can provide insight into the binding affinities of ligands and receptors. Moreover, performing this experiment on different regions of the plasma membrane can uncover the effect of ligand concentration gradients in binding events [45].

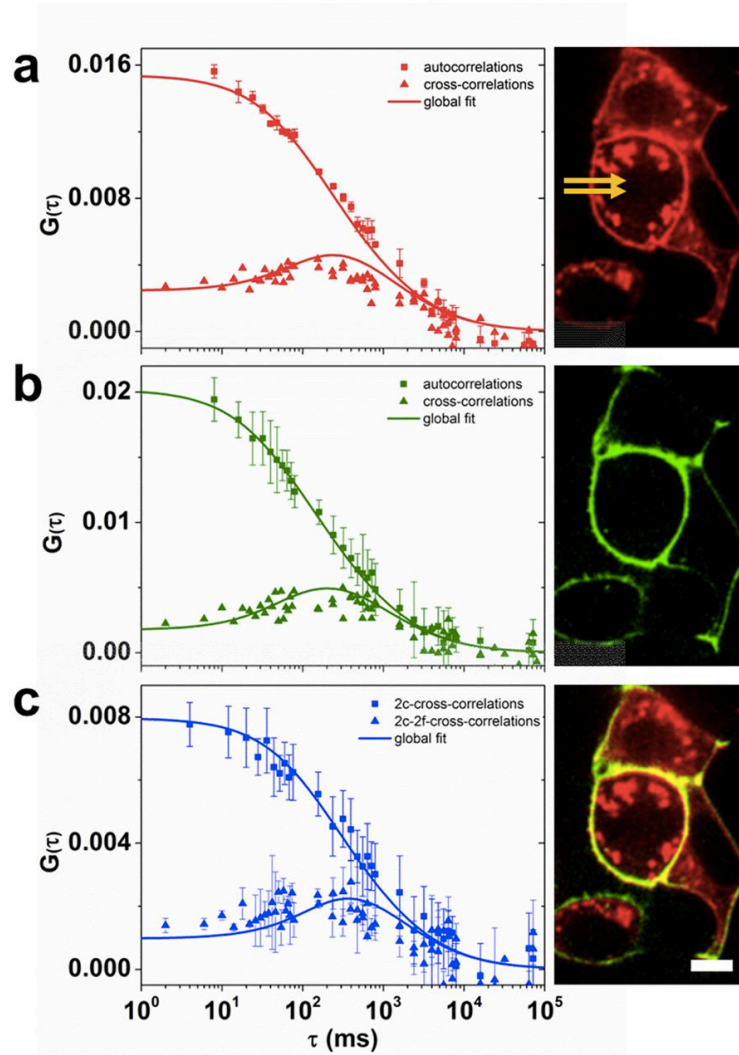


Figure 1.7 A) Autocorrelation and dual-focus cross-correlation functions and fluorescence image obtained from the red channel for the fusion protein of human LRP6 with mCherry (LRP6-mCherry), the two line scan locations are marked by yellow arrows, B) autocorrelation and dual-focus cross-correlation functions and fluorescence image obtained from the green channel for fusion proteins of human Dkk1 with GFP (Dkk1-GFP), C) dual-color cross-correlation and dual-color dual-focus cross-correlation functions and dual-color image. Error bars indicate standard deviations from multiple data sets. Scale bar = 15 μm [45].

1.2.3 Image Correlation Spectroscopy

1.2.3-1 Spatial Image Correlation Spectroscopy

Image correlation spectroscopy (ICS), originally described by Petersen *et al.* in 1993, is the imaging analog of scanning FCS, which can measure the size and number of protein aggregates and the oligomerization states in the plasma membrane [46–48]. In contrast to FCS, ICS is based on fluctuations of fluorescence as a function of space across

an image. Over the past two decades, the original ICS method has been further extended to include both the spatial and temporal domains as well as the analysis in k-space and time [49]. This section introduces ICS and the mathematical image processing methods that have been derived from the original implementation, which all serve as complementary tools to analyze changes in the distribution of cluster size and density, as well as diffusion and flow of molecules within biological membranes.

All ICS-based techniques use information of the intensity fluctuations recorded in the pixels of fluorescent images. A correlation function is first calculated from the fluorescent image series with intensities recorded as a function of space and time $i(x, y, t)$. The correlation function is then fit to an analytical model to extract the parameters of interest. Most ICS-based methods can be described by the generalized spatio-temporal correlation function provided by equation (1.9) [47]. The equations introduced in the following sections are derivations of the original function described by:

$$r_{ab}(\xi, \eta, \tau) = \frac{\langle \delta i_a(x, y, t) \delta i_b(x + \xi, y + \eta, t + \tau) \rangle}{\langle i_a(x, y, t) \rangle_t \langle i_b(x, y, t + \tau) \rangle_{t + \tau}}, \quad (1.9)$$

where $i(x, y, t)$ is the intensity at pixel (x, y) in the image recorded at time t . The fluorescence intensity fluctuation $\delta i(x, y, t)$ is calculated as:

$$\delta i(x, y, t) = i(x, y, t) - \langle i(x, y, t) \rangle_t, \quad (1.10)$$

where $\langle i(x, y, t) \rangle_t$ is the average intensity of the image at time t . The variables ξ and η represent spatial increments in the x and y directions, respectively, and τ is the time lag. The subscripts a and b refer to two different emission wavelength detections. For the autocorrelation of a single detection channel, $a = b$; and therefore, the subscripts can be omitted.

The variance of the signal fluctuation is equal to the value of the correlation function at its zero-lag amplitude according to:

$$\lim_{\xi \rightarrow 0, \eta \rightarrow 0, \tau \rightarrow 0} r(\xi, \eta, \tau) = \frac{\langle (i(x, y, t) - \langle i(x, y, t) \rangle_t)^2 \rangle}{\langle i(x, y, t) \rangle_t^2} = \frac{\langle (\delta i)^2 \rangle}{\langle i \rangle^2} = \frac{1}{\langle n_p \rangle}, \quad (1.11)$$

where $\langle n_p \rangle$ indicates the independent fluorescent particles per beam area that can be converted to cluster density (CD) by:

$$CD = \frac{\langle n_p \rangle}{\pi \omega_0^2}, \quad (1.12)$$

where ω_0 is the radius of the point spread function (PSF). If the beam radius is known (through calibration measurements), it is possible to calculate the beam area and hence the surface density of fluorescent molecules from the zero-lag autocorrelation amplitude.

Given that the average intensity of an image is proportional to the number of fluorophores present in the beam area, the degree of aggregation (DA) is defined as the ratio of the average intensity $\langle i \rangle$ and CD:

$$DA = \frac{\langle i \rangle}{CD} = c \frac{\langle n_m \rangle}{n_p}, \quad (1.13)$$

where c is a proportionality constant that depends on the spectral characteristics of the fluorophore and the efficiency of the imaging system to collect light. DA can be also calculated as a function of time for an image series to measure changes in the aggregation state of proteins.

In the original implementation of ICS, a spatial autocorrelation function is calculated from an image or ROI by correlating it with itself as a function of pixel shifts in the x and y directions (Figure 1.8-A). Therefore, the normalized spatial autocorrelation function for the intensity fluctuation of an image in a series, recorded at time t with no time lag ($\tau = 0$), is defined by:

$$r(\xi, \eta, 0)_t = \frac{\langle \delta i(x, y, t) \delta i(x + \xi, y + \eta, t) \rangle}{\langle i(x, y, t) \rangle_t^2}, \quad (1.14)$$

where the angular brackets denote spatial averaging over the entire image. The two dimensional spatial correlation can be computed efficiently using fast Fourier transform methods, and interested readers are referred to the original paper for full derivation of the relevant equations [47]. The average size and distribution of plasma membrane protein aggregates that are larger or comparable in size to the PSF can be determined by the spatial correlation operation applied to the intensity values of pixels in the image (Figure 1.8-B).

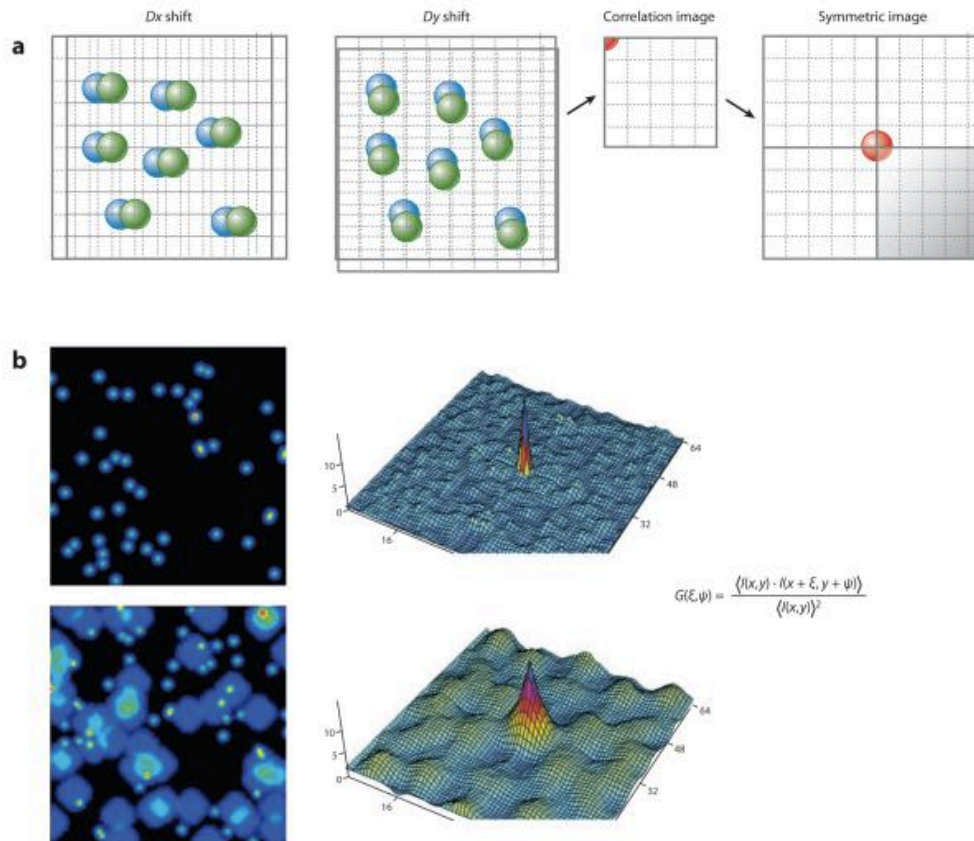


Figure 1.8 A) Schematic representation of the spatial correlation operation for an image shifted by Dx and Dy . The intensity at each pixel in the original frame is multiplied by the intensity of the displaced frame, and the summation of all products are calculated and divided by the squared average intensity. This value is assigned to pixel (1, 0) in the correlation image. Repeating this process for all possible displacements in x and y direction will generate the spatial correlation which is 50% of the size of the original image. B) The spatial correlation for smaller image features will be smaller compared to large particles or aggregates [34].

ICS has been used to study the aggregation of several membrane receptors including the platelet-derived growth factor $\beta 2$ receptors on the membrane of fibroblasts [47,50], as well as the distribution of clathrin associated adaptor protein (AP-2) involved in endocytosis on the plasma membrane [51]. In addition, image cross-correlation spectroscopy (ICCS) [47,52] has been developed using dual-color fluorescence microscopy to investigate co-localization of two different molecules such as the distribution of α -actinin and $\alpha 5$ -integrin on Chinese hamster ovary (CHO) cells [53]. In ICCS the spatial or temporal intensity fluctuations from two different fluorescent molecules are analyzed by computing the cross-correlation function between two images. A non-zero spatial cross-correlation function indicates that the proteins reside in the same

complex, while a non-zero temporal cross-correlation indicates a moving complex. The concept of temporal image correlation spectroscopy is explained in Section 1.2.3-2.

The accuracy and precision of ICS measurements depend on the number of sampling points and the background noise [54]. In general, analyzing larger and more homogenous ROIs in a sample results in more accurate correlations. Although ICS can be performed on regions as small as 16×16 px² (~ 1.5 μm^2 , PSF of ~ 5 pixels), larger ROIs are recommended for reliable statistics [54]. Discontinuities in the fluorescence intensity, such as the edge of a cell, should be minimized as they can introduce significant perturbations in the correlation function. Furthermore, an unbiased estimate of the number density can be achieved only if the correct amount of background intensity is subtracted from images, both for single measurements [54] and population averages [47].

1.2.3-2 Temporal Image Correlation Spectroscopy

Spatial ICS can provide a measure of density and aggregation state of macromolecules in biological membranes; however, information on the dynamics of molecules cannot be extracted. Temporal image correlation spectroscopy (TICS) correlates the intensity fluctuations in time through the image series to measure the dynamics. This is the same concept as the carpet approach in scanning FCS, described in Section 1.2.2-3. In TICS, the intensity of each pixel is correlated in time with the intensity of the same pixel coordinate in the next frame to analyze the changes in intensity at each pixel (Figure 1.9). The rate of decay of the correlation function reflects the average decay time of the fluctuations as fluorescent entities move in and out of the area defined by the beam focus.

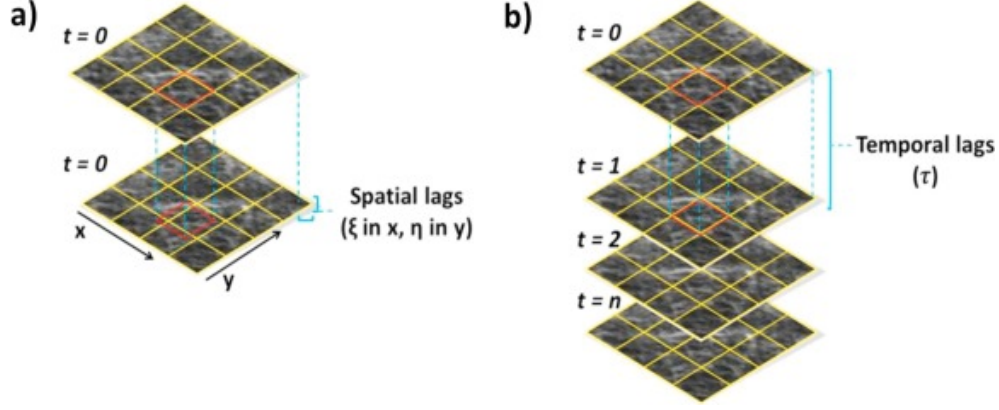


Figure 1.9 A) Spatial correlation of a dataset with itself (autocorrelation) at a given time t results in perfect correlation, whereas shifting the image relative to the reference image by ξ and η results in a spatial correlation, B) temporal correlation of a series of images, by correlating the same pixel coordinate through multiple images [55].

The normalized intensity fluctuation temporal autocorrelation function of an image series can be obtained from the original equation (1.9), with no shift in space ($\xi=0, \eta=0$):

$$r(0, 0, \tau) = \frac{\langle \delta i(x, y, t) \delta i(x, y, t + \tau) \rangle}{\langle i(x, y, t) \rangle_t \langle i(x, y, t + \tau) \rangle_{t + \tau}}, \quad (1.15)$$

where the time lag τ is determined from the interval between consecutive frames. This function is computed using fast Fourier transform methods [47]. A discrete approximation of the temporal autocorrelation function for an image series can be obtained from:

$$r(0, 0, s) = \frac{1}{N-s} \sum_{c=1}^{N-s} \frac{1}{XY} \sum_{x=1}^X \sum_{y=1}^Y \frac{\delta i(x, y, c) \delta i(x, y, c+s)}{\langle i(x, y, c) \rangle_c \langle i(x, y, c+s) \rangle_{c+s}}, \quad (1.16)$$

where X and Y are the number of pixels in the x and y direction of the image frame, respectively. N is the total number of frames in the image series, s is the discrete analog of τ , and c is a dummy variable. The calculated temporal correlation function is then fit to the analytical decay model derived for the sample. Three parameters can be determined from a time correlation function: *amplitude*, which is inversely proportional to the number of particles; *shape of decay*, which describes the mode of transport (*i.e.*, diffusion or flow); and *rate of decay*, which determines how fast the dynamic process is occurring.

For samples with 2D diffusion, the diffusion coefficient D can be calculated from:

$$D = \frac{\langle \omega_0 \rangle}{4\tau_D}, \quad (1.17)$$

where $\langle \omega_0 \rangle$ is the mean radius of the excitation beam and τ_D is the characteristic diffusion time.

Similarly, the characteristic flow time τ_f from the correlation decay model of a sample with 2D flow can be used to measure the flow speed $|v|$ according to:

$$|v| = \frac{\langle \omega_0 \rangle}{\tau_f}, \quad (1.18)$$

TICS has been applied to several studies on membrane dynamics, such as the analysis of protein flow in the peripheral basal membrane of CHO cell expressing EGFP-labeled α -actinin [56], the lateral mobility of GFP- $\alpha 5$ integrin adhesion receptors on the basal membrane of CHO fibroblasts [52], and interactions of α -actinin and $\alpha 5$ -integrin on CHO as part of the formation and disassembly of adhesion complexes during cell migration [53]. Cross-correlation has been applied to measure translational diffusion of transferrin receptors in the membrane of 3T3 fibroblasts and HEp2 carcinoma cells [57].

TICS can resolve multiple populations undergoing diffusion and flow simultaneously, as well as to detect the fraction of particles that are immobile; however, the ability to extract multiple populations is limited by a number of factors including the relative concentrations and quantum yields of the different fluorescent species [58]. TICS is better suited for the study of slow moving proteins in membranes, as the characteristic fluctuation time must be longer than the frame rate. In other words, to correlate the intensities of the same molecule in two subsequent frames, the fluorophores captured within a focal area must be scanned in almost the same position in the next frame. Using standard imaging rates ~ 0.1 -30 Hz, TICS can measure the diffusion of membrane proteins but is incapable of capturing the faster diffusion of lipid molecules or cytoplasmic components [52]. In Section 1.2.3-4, we will describe Raster Image Correlation Spectroscopy (RICS), a related technique that can be used to measure faster transport processes.

1.2.3-3 Spatio-temporal Image Correlation Spectroscopy

As discussed in the previous section, TICS can measure diffusion and flow speed of moving particles; however, the velocity (*i.e.*, the magnitude and direction of flow) cannot be determined from temporal correlations. The spatio-temporal image correlation spectroscopy (STICS) is an extension of TICS, which does not separate the spatial fluctuation correlation from the temporal one for the analysis of flow direction [56]. The STICS correlation function can be derived from the original ICS equation (1.9), and is described by:

$$r(\xi, \eta, \tau) = \frac{\langle \delta i(x, y, t) \delta i(x + \xi, y + \eta, t + \tau) \rangle}{\langle i \rangle_t \langle i \rangle_{t + \tau}}, \quad (1.19)$$

where ξ and η represent spatial shifts in the x and y directions, respectively, and τ is the time lag. The angular brackets in the denominator denote averaging intensity over images at time t and $t + \tau$ in the time series, while the numerator is an average over all pixel fluctuations in pairs of images separated by τ .

The spatial correlation at zero-time lag yields a correlation function centered at the origin. As τ increases, for fluorescent molecules undergoing diffusion or flow, the peak will change shape or position from the center. For a diffusion process, in the absence of flow, the peak remains at the center while its width increases, whereas in the presence of flow the correlation function moves from the zero-lag center as a function of time lag (Figure 1.10-A). The velocity of the flow can then be determined by monitoring the center of the 2D average spatial correlations for every time lag. The x and y components of the velocity vector can be obtained from linear regression of the x and y coordinates of the peak location of the spatial correlation as a function of time (Figure 1.10-C).

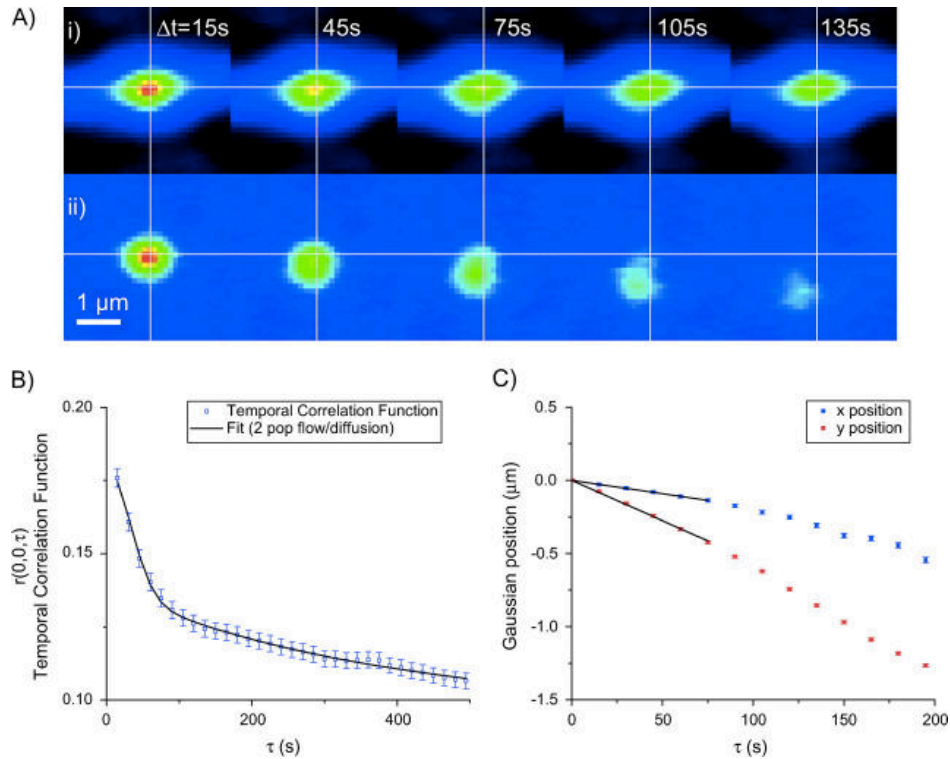


Figure 1.10 A) STICS analysis of protein flow in the peripheral basal membrane of CHO cell expressing EGFP-labeled α -actinin. The space-time correlation functions as a function of time i) with and ii) without removal of the immobile population show the flow direction is visible after filtering the immobile fraction. B) TICS analysis best fit yields two population model of flow/diffusion with $v_{ICS} = (7.7 \pm 0.8) \times 10^{-3} \mu\text{m/s}$ and $D = (6 \pm 1) \times 10^{-5} \mu\text{m}^2/\text{s}$. C) linear regression of the x and y Gaussian center positions as a function of time lag yields the velocity vector components $v_x = (1.8 \pm 0.3) \times 10^{-3} \mu\text{m/s}$ and $v_y = (5.5 \pm 0.2) \times 10^{-3} \mu\text{m/s}$, respectively [56].

STICS has been used to extract diffusion parameters of GFP-tagged transmembrane transferrin receptor that is transiently confined by the cytoskeleton [59], and to analyze protein flow in the peripheral basal membrane of CHO cell expressing EGFP-labeled α -actinin (Figure 1.10) [56]. In the STICS approach, it is necessary to remove the immobile fraction of particles prior to performing the analysis for flow, as they interfere with the accurate tracking of the spatial correlation peak (Figure 1.10-A). The immobile population is usually eliminated by subtracting the mean of the image series from each image. Using Fourier transform to filter the zero-frequency components in time can efficiently remove the contribution of immobile populations and makes detection of flow possible, even in the presence of a large fraction (>90%) of immobile species [56].

1.2.3-4 Raster Image Correlation Spectroscopy

Raster Image Correlation Spectroscopy (RICS) measures the fluctuations in the intensity –caused by the movement of fluorescent molecules– at the pixel level in an image and makes use of this data to calculate diffusion coefficients [60]. By measuring the intensity at one pixel for a very brief period of time followed by measuring the intensity of adjacent pixels immediately after, there will be a correlation in the intensity fluctuations between these pixels with a certain time delay as a fluorescent molecule moves to its neighboring pixels [60]. The spatial correlation depends on the rate of diffusion, the pixel dwell time, and the size of pixels. For immobile particles, the fluctuations do not extend to the neighboring pixels and the correlation shows a distribution that is different to that of mobile particles. Similarly, slow and fast diffusing particles can be distinguished by their spatial correlations. This concept is demonstrated in Figure 1.11. Since confocal laser-scanning microscopy (CLSM) is used for RICS, adjacent pixels along the line of scan (horizontal) are a few to several hundred microseconds apart (pixel dwell time), while pixels over successive lines (vertical) are typically a few milliseconds apart (line scan time dependent on the number of pixels), as shown in Figure 1.11. Therefore, there is an inherent time structure in each acquired frame and the intensities of pixels contained in one frame can be correlated to determine the characteristic correlation decay times corresponding to various dynamic processes, such as diffusion or binding of fluorescent particles. A series of 50-100 frames that are seconds to minutes apart are usually captured with no delay between frames. The stack of images not only provides more reliable statistics but also is useful for correction of photobleaching effects and separating the immobile fraction for RICS analysis.

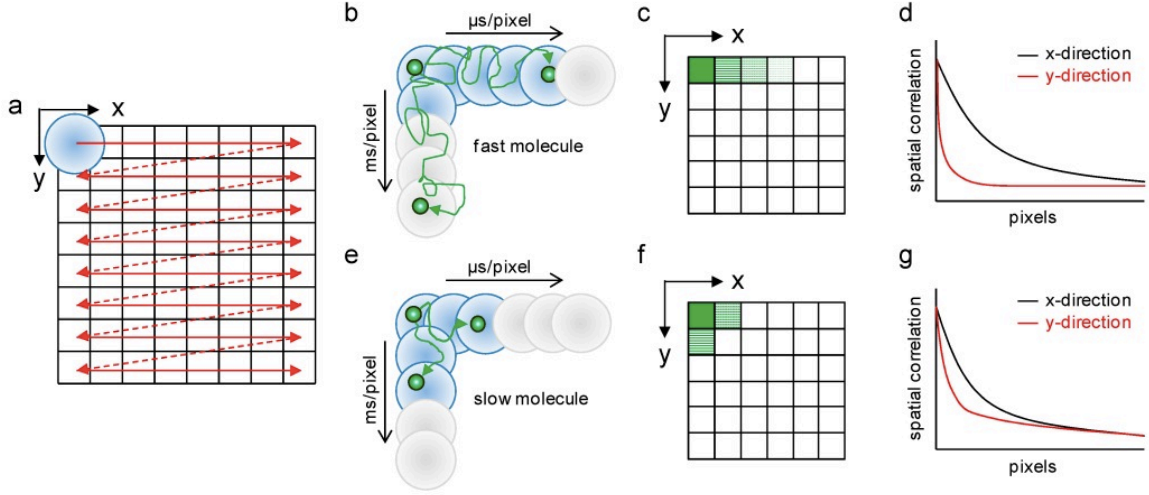


Figure 1.11 A) Schematic representation of raster scanning of an image frame with a laser beam moving pixel by pixel and line by line until the full frame is captured, B) emissions from a fast diffusive molecule that is moving in the direction of the laser scan is captured in neighboring pixels, C) the intensity gradient seen in adjacent pixels where the fast diffusing fluorescent molecule was captured, D) spatial correlation in the x and y direction for fast diffusive molecules, E) the intensity gradient does not extend further along the line of scan for slow diffusion, F) emissions from a slow molecule that is moving in the direction of the laser scan is captured only in a few neighboring pixels in the x direction, but also in the y direction, G) spatial correlation in the x and y direction for slow molecules [61].

The RICS theory has been previously described in detail by Digman *et al.* [39,60,62]. Here, we only briefly reiterate the principles of RICS. The scanning function that relates time with space, *i.e.*, the spatio-temporal correlation rather than the simple temporal correlations of conventional FCS, is defined as:

$$\tau(\xi, \psi) = \tau_p \xi + \tau_l \psi \quad , \quad (1.20)$$

where τ_p and τ_l denote pixel dwell time and line time of scan, respectively. The ξ and ψ variables are the spatial displacements (in pixels) in the horizontal and vertical direction of scan in the image, respectively. The normalized spatial autocorrelation function for the fluorescence intensity fluctuation is defined as:

$$G_s(\xi, \psi) = \frac{\langle \delta I(x, y) \delta I(x + \xi, y + \psi) \rangle_{x, y}}{\langle I(x, y) \rangle_{x, y}^2} = G(\xi, \psi) S(\xi, \psi) \quad , \quad (1.21)$$

where $I(x, y)$ is the detected fluorescence intensity at each pixel and $\delta I(x, y) = I(x, y) - \langle I(x, y) \rangle_{x, y}$ is the fluorescence intensity fluctuations around the mean intensity. Using the characteristic diffusion correlation time $\tau_D = \omega_0^2 / 4D$ the autocorrelation function for 3D diffusion is:

$$G(\xi, \psi) = \frac{\gamma}{N} \left(1 + \frac{4D(\tau_p \xi + \tau_l \psi)}{\omega_0^2}\right)^{-1} \left(1 + \frac{4D(\tau_p \xi + \tau_l \psi)}{\omega_z^2}\right)^{-1/2}. \quad (1.22)$$

For 2D diffusion, the last factor in the above equation is omitted. In this function, D is the diffusion coefficient, N is the average number of molecules in the illumination volume, and ω_0 and ω_z are the lateral and axial waists of the laser beam at the point of focus. The geometric factor γ accounts for the non-uniform illumination of the excitation volume and is equal to 0.3535 for a 3D and 0.5 for a 2D Gaussian point spread function [63].

$G(\xi, \psi)$ is the autocorrelation function as a result of molecular diffusion only. Since the PSF spans over several pixels in the imaging plane, the correlation for the contribution of the scan itself should be also taken into account, as shown in equation (1.21). For square pixels with dimension $\delta r \times \delta r$ the correlation for the scan is given by:

$$S(\xi, \psi) = \exp\left(\frac{\left[\frac{(\xi \delta r)^2}{\omega_0^2} + \frac{(\psi \delta r)^2}{\omega_0^2}\right]}{1 + \frac{4D(\tau_p \xi + \tau_l \psi)}{\omega_0^2}}\right). \quad (1.23)$$

The original RICS approach was based on 2-photon excitation and photon counting to measure diffusion in 3D [39,62]. Nowadays, commercial CLSM with one-photon excitation and analog detection provides an efficient way to measure molecular diffusion in 3D and in 2D [64,65]. The reduction of out-of-focus signal using CLSM enables measurements that are confined to a narrow plane in the cell. In addition, the ability of RICS to separate the slow and immobile fractions makes it possible to detect heterogeneities in diffusion [39,62,65]. Figure 1.12 illustrates an example of a diffusion map obtained from RICS for the fluorescent lipid analog DiI-C₁₈(5) (1,1'-dioctadecyl-3,3,3',3'-tetramethyl-indodicarbocyanine perchlorate) in the plasma membrane of oligodendrocytes, *i.e.*, the myelin-producing cells of the central nervous system [66]. The diffusion map provided by RICS analysis of 32×32 pixel ROIs reveals that the diffusion of DiI-C₁₈(5) varies from $0.4 \mu\text{m}^2 \text{s}^{-1}$ (dark blue) to $26.5 \mu\text{m}^2 \text{s}^{-1}$ (red) in different areas of membrane [66].

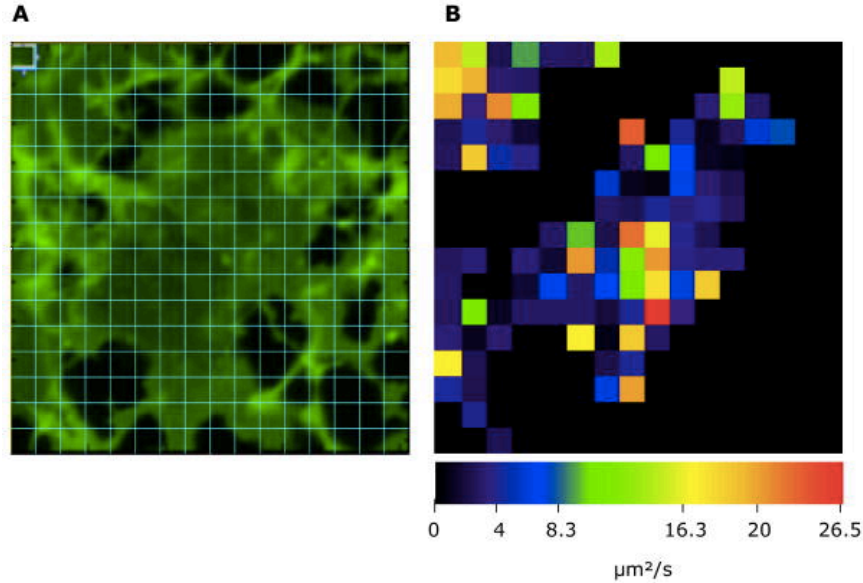


Figure 1.12 A) Raster-scan image (512×512 pixels) of a primary oligodendrocyte labeled with DiI- $C_{18}(5)$ with the grid pattern showing the sub-regions (32×32 pixels) for RICS analysis, B) diffusion map of DiI- $C_{18}(5)$ in the plasma membrane obtained from RICS analysis of 100 frames, encompassing a range from $0.4 \mu\text{m}^2 \text{s}^{-1}$ (dark blue) to $26.5 \mu\text{m}^2 \text{s}^{-1}$ (red) due to heterogeneity in diffusion. Pixel size of 54.9 nm and pixel dwell time of $1.6 \mu\text{s}$ was used for 100 frames [66].

RICS is also frequently utilized to measure the diffusion coefficient of proteins in live cells [62,65,67-69]. Figure 1.13 shows an example of a diffusion measurement of the adhesion protein Paxillin-EGFP in CHOK1 cells, which is seen as bright finger-like structures [62]. The RICS measurement was performed on the cytosol area where the protein is soluble, yielding a diffusion coefficient of $8.3 \mu\text{m}^2 \text{s}^{-1}$ using a pixel dwell time of $8 \mu\text{s}$ and pixel size of $0.09 \mu\text{m}$. The 2D and 3D autocorrelation functions are shown in Figure 1.13-D and 1.13-E, respectively. Figure 1.13-D was obtained after removing the immobile fraction (see also Figure 1.13-C). The immobile features yield a dominant correlation pattern in which the fast diffusing particles are difficult to detect. Therefore, filtering out the immobile or slowly moving particles is key to achieving reliable statistics. Figure 1.13-E shows the 3D autocorrelation function $G(\xi, \psi)$ and the residuals after fitting the experimental data [62].

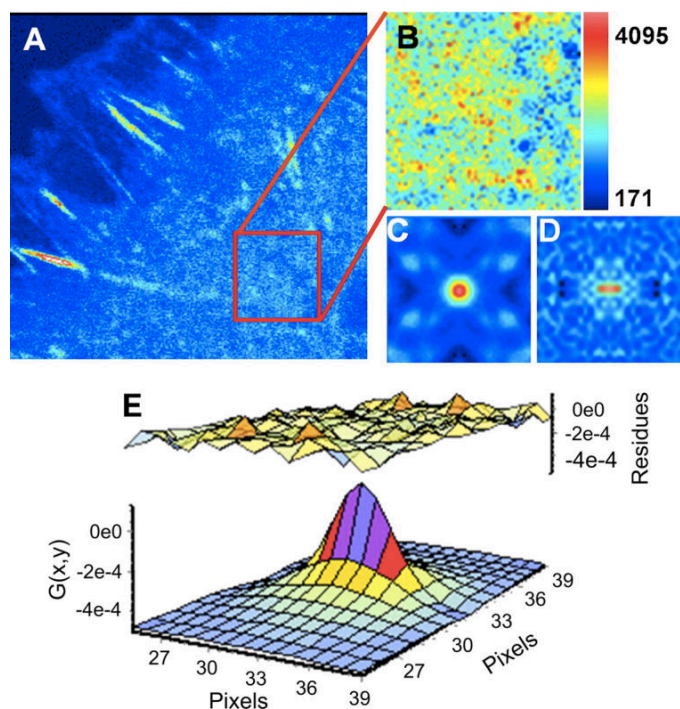


Figure 1.13 A) CHOK1 cell expressing paxillin-EGFP, B) 64×64 ROI in the cytosolic part free of focal adhesion structures, C) 2D spatial autocorrelation before subtraction of immobile structures, D) 2D spatial autocorrelation after subtraction of immobile structures, E) fit of the spatial correlation function in D [62].

In addition to measuring diffusion, RICS can also be used to distinguish binding and unbinding processes by analyzing changes in the diffusion coefficients [68]. Moreover, interactions between biomolecules can be detected through correlation of intensity fluctuations measured simultaneously in two channels. This technique is known as cross-correlation raster image spectroscopy and is based on fluctuations occurring concurrently in two separate channels [67]. Furthermore, raster-scan image data can be analyzed using statistical methods such as number and brightness [70] to further uncover the aggregation state of molecules. All these features make RICS a versatile technique for measuring fast as well as slower dynamic processes in biological membranes using standard CLSM.

1.2.3-5 Arbitrary-Region Raster Image Correlation Spectroscopy

The traditional algorithm used in RICS analysis only accepts $n \times n$ ROIs, where n is the number of pixels (typically > 64). However, the complex shape of many cells and the small size of organelles make it difficult to perform the analysis with square ROIs. While decreasing n ameliorates this problem [66,71], it leads to poor statistics and inaccurate

spatial correlation of the sample. The recently developed arbitrary-region raster image correlation spectroscopy (ARICS) is an adapted version of ICS that can use ROIs of any shape. Instead of using the classically defined ROI in the shape of a square or rectangle, it uses algorithms for manually drawing an arbitrary ROI. This is particularly useful for masking unwanted regions such as background and areas that are not related to the experiment (*e.g.*, the nucleus). Figure 1.14 compares the conventional and arbitrary ROI approach [72]. For the cell image in Figure 1.14-A, the normal ROI encompasses the full image including the whole cell and its extracellular region (Figure 1.14-B). In contrast, the arbitrary ROI mask (Figure 1.14-D) generated by intensity thresholds highlights the cytosol of the cell and excludes its nucleus and surrounding environment. Figures 1.14-C and E show that there are significant differences in the spatial autocorrelation obtained from the two methods [72].

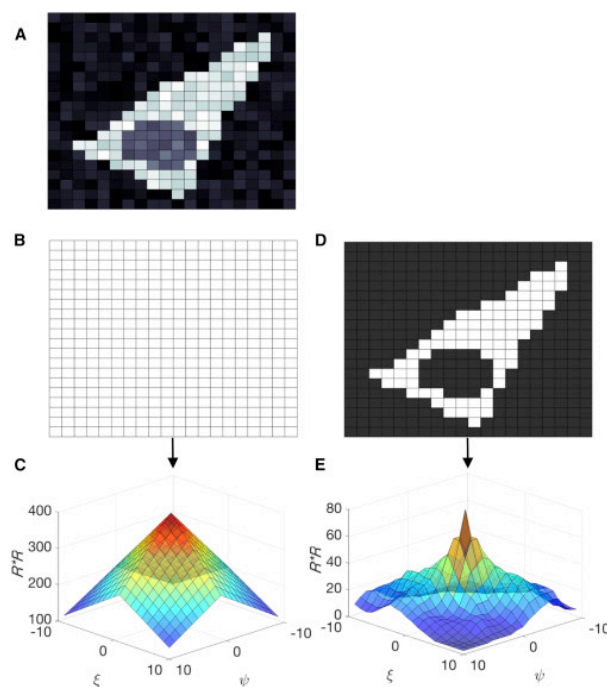


Figure 1.14 A) Schematic image of a cell exhibiting fluorescence intensity in the cytosol, B) conventional square ROI encompassing the entire image including the cell and its surrounding environment, C) spatial autocorrelation of the square ROI, D) binary image generated from arbitrary ROI mask by applying an intensity threshold to include only the cytosolic region of cell, E) spatial autocorrelation of the cytosolic region [72].

The ARICS region-specific analysis has been used to measure the diffusion behavior in HeLa cells co-expressing cytosolic Venus fluorescent protein and membrane-targeted

MyrPalm-YFP (Figure 1.15) [72]. The cytosol and the membrane were analyzed separately using ARICS and the spatial autocorrelation function was obtained for each region in the cell, yielding diffusion coefficients of $D = 0.3 \pm 0.1 \mu\text{m}^2 \text{s}^{-1}$ and $D = 30 \pm 7 \mu\text{m}^2 \text{s}^{-1}$ in the membrane and cytosol, respectively [72].

ARICS's applications are not limited to those mentioned above. For example, heterogeneities within the sample, such as aggregates that are too bright or dim, or organelles diffusing through the image that are considered to be artifacts in the series of frames, can be easily detected and removed to make RICS measurements much more reliable. This can be achieved by adding a predetermined threshold (acceptable range for pixel intensity, maximum fluctuation from the average intensity, etc.). The principles of ARICS can also be applied to cross-correlation analysis of two or more channels as well as other fluctuation-based methods such as ICS and STICS that analyze spatial fluctuations [72].

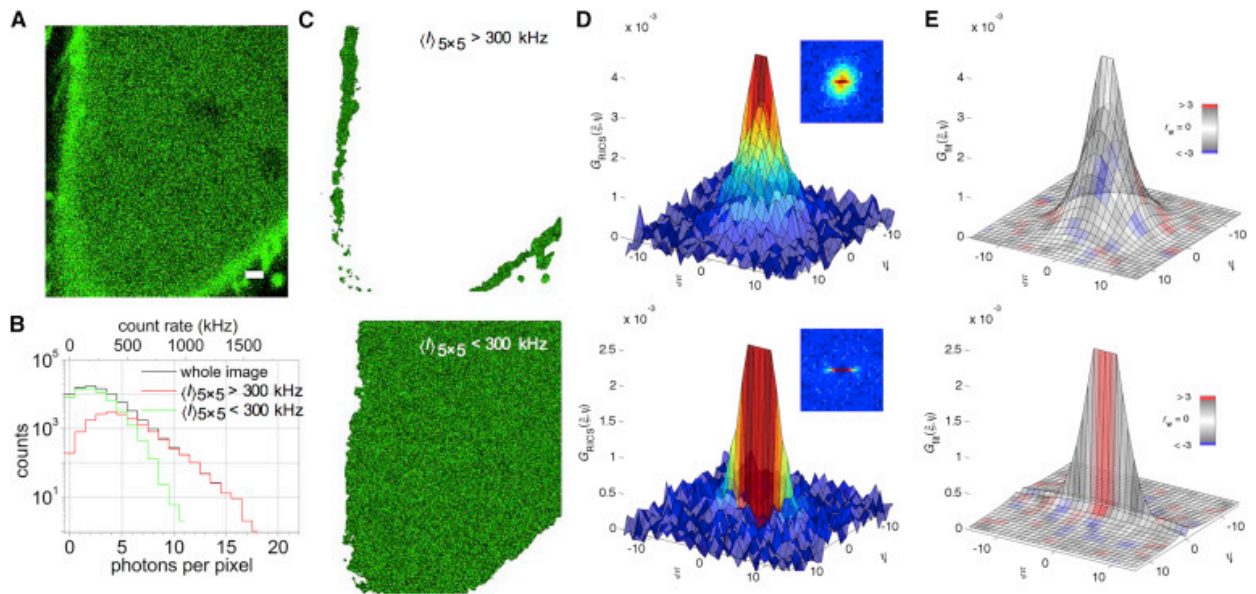


Figure 1.15 A) Image frame (from series of 100 frames) captured from a HeLa cell coexpressing cytosolic Venus fluorescent protein and membrane-targeted MyrPalm-YFP. Scale bar = 1 μm . B) Intensity distribution histogram of all pixels in the frame (black) and arbitrary ROI with two intensity thresholds to separate the photon counts for membrane (green) and cytosol (red), C) Membrane (top) and cytosol (bottom) regions are selected after image processing original frames using intensity thresholds, D) Region-specific spatial autocorrelation function for membrane (top) and cytosol (bottom), E) Residuals of the fit to the average autocorrelation functions are shown with color codes [72].

1.2.3-6 Stimulated Emission Depletion-FCS/RICS

FCS and RICS techniques require fluorophore concentrations in the nanomolar range so that the amplitudes of fluorescence fluctuations are sufficiently large to be detected; however, these concentrations are too dilute to observe most biological processes. Thus, in spite of the very small fL observation volumes created by confocal microscopes, the number of molecules under observation in most biological studies exceeds the optimum concentration, making the use of these techniques challenging. The use of stimulated emission depletion (STED) in combination with FCS [73,74] or RICS [75] can decrease the observation volume significantly so that 10-100 times higher fluorophore concentrations can be measured. Moreover, the higher spatial resolution of STED-FCS and STED-RICS enables the study of smaller subcellular regions.

Using STED in a confocal setup, the specimen is illuminated by the excitation beam overlaid with a second, red-shifted depletion beam inducing stimulated emission of electronically excited fluorophores (Figure 1.16-A). Appropriate phase modulation of the depletion beam creates a zero node region in the center of the focal volume where fluorophores emit fluorescence and their emission is captured by the detector. In contrast, the fluorophores outside the zero node are exposed to the STED beam and are transferred back to their ground state (non-fluorescent) by means of stimulated emission. The size of the observation volume can be adjusted by the intensity of the STED beam. Increasing the STED power decreases the observation volume and as a result larger fluctuations and correlation amplitudes can be generated (Figure 1.16-B, D). The lateral size of the non-depleted region, the effective observation area, with diameter d_{STED} is determined by:

$$d_{STED} = \frac{d}{\sqrt{1 + A \frac{I_{STED}}{I_s}}}, \quad (1.24)$$

where d is the diameter of the diffraction-limited excitation spot, A is a geometrical parameter that takes into account the shape of the STED laser beam, I_{STED} is the STED laser intensity, and the I_s is the saturation intensity which depends on the depletion efficiency of the fluorescent label used. Theoretically, the spatial resolution can be enhanced without limit; however, in practice a lateral resolution of 20-50 nm

has been achieved for studies on cells [76], which is due to photophysical limitations of the fluorophores.

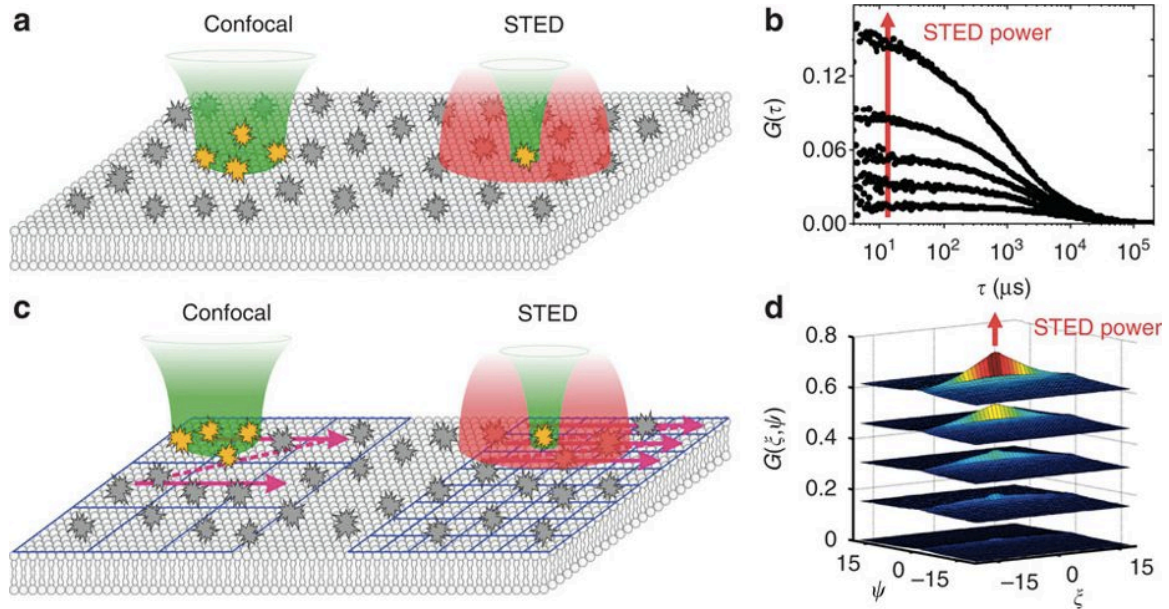


Figure 1.16 A) FCS measurement (left) compared with STED-FCS (right) with a significantly decreased observation volume, B) the amplitude of the autocorrelation function increases as the STED power increases, C) RICS measurement (left) compared with STED-RICS (right) with a significantly decreased observation volume, D) RICS spatial correlation function with autocorrelation amplitude increasing as a result of higher STED power [75].

A comparison of STED-RICS and conventional RICS is shown in Figure 1.17 for three different biological samples [75]. Figure 1.17-A is the overview of an RBL-2H3 mast cell with its FcεRI receptors bound to IgE labeled with Atto647N in the plasma membrane. The region in the white rectangle is displayed as a close-up STED image and a regular confocal image, showing that the bound complex is not homogeneously distributed in the membrane. STED-RICS and RICS correlation functions are shown for comparison in Figure 1.17-B and 1.17-C showing that the RICS analysis could not be performed. In the second sample, the focal adhesions, β1-integrin, of *Xenopus laevis* tissue culture (XTC) cells are immunostained with the monoclonal antibody 8C8 labeled with Atto647N. STED-RICS resulted in a slow diffusion coefficient of $0.08 \pm 0.04 \mu\text{m}^2 \text{s}^{-1}$ (24°C) which is evident in the wider $G(\xi, \psi)$ along the ψ axis (Figure 1.17-E). In contrast, $G(\xi, \psi)$ obtained from the confocal RICS is not suitable for quantitative analysis (Figure 1.17-F). In the third sample shown in Figure 1.17-G the

STED-RICS measurements yield a faster diffusion coefficient of $D=1.6\pm 0.4 \mu\text{m}^2 \text{s}^{-1}$ (24°C) for Atto647N-DPPE-BSA complex in the plasma membrane of XTC cells. In contrast, the confocal RICS failed to analyze this region due to high concentration of fluorescent markers and the small size of the region of interest. These examples demonstrate that the higher spatial resolution of STED-RICS enables dynamic measurements in smaller regions of the membrane that would otherwise remain uncovered by RICS analysis.

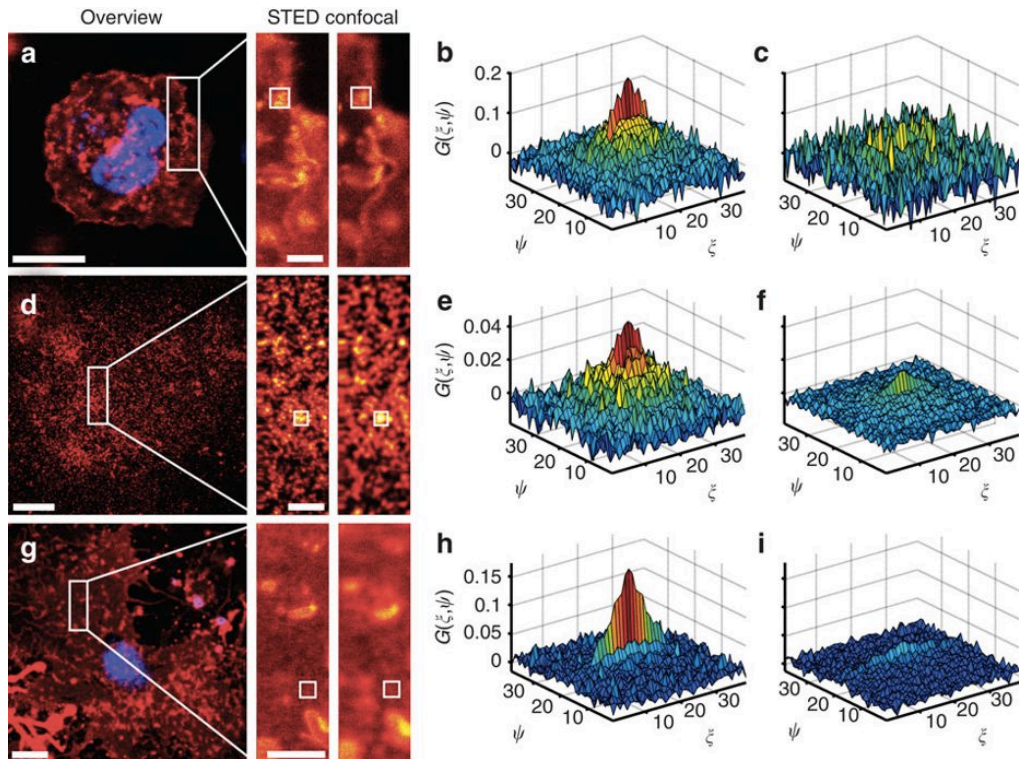


Figure 1.17 A) Fluorescence image (overview) of an RBL-2H3 mast cell with its plasma membrane FcεRI receptors bound to Atto647N-labeled IgE (red channel) and the close-up in STED and confocal modes, B) STED-RICS and C) RICS correlation functions from the small ROI (62×62 pixels) marked by a white square. FcεRI diffusion $D = 0.5 \pm 0.2 \mu\text{m}^2 \text{s}^{-1}$ (37°C) was obtained using STED intensity of 200 mW, pixel size of 16 nm, and dwell time of 10 μs , D) fluorescence image (overview) of a *Xenopus laevis* tissue culture (XTC) cell immunostained with monoclonal anti- $\beta 1$ -integrin IgG 8C8 labeled with Atto647N (red channel), E) STED-RICS and F) RICS correlation functions from the small ROI (38×38 pixels) marked by a white square. Slower diffusion $D = 0.08 \pm 0.04 \mu\text{m}^2 \text{s}^{-1}$ (24°C) was obtained for $\beta 1$ -integrin using a STED intensity of 100 mW, pixel size of 16 nm, and dwell time of 20 μs . G) fluorescence image (overview) of an XTC cell labeled with Atto647N-DPPE-BSA (red channel), H) STED-RICS and I) RICS correlation functions from the small ROI (50×50 pixels) marked by a white square. Faster diffusion $D = 1.6 \pm 0.4 \mu\text{m}^2 \text{s}^{-1}$ (24°C) was obtained using a STED intensity of 200 mW, pixel size of 10 nm, and dwell time of 10 μs . Scale bars: 10 μm (overview) and 2 μm (close-ups) [75].

The correlation analysis in STED-RICS is similar to the RICS approach explained in Section 1.2.3-4. The autocorrelation function $G(\xi, \psi)$ is calculated and the data is fit with the equation:

$$G(\xi, \psi) = \frac{\gamma}{N} G_D(\xi, \psi) G_S(\xi, \psi) G_K(\xi, \psi), \quad (1.25)$$

where, N is the average number of particles in the observation volume and $\gamma=0.35$ is a correction factor for 3D Gaussian intensity profile for the non-uniform illumination of the excitation volume [62]. The term $G_D(\xi, \psi)$ accounts for free 2D diffusion and is determined by:

$$G_D(\xi, \psi) = \left(1 + \frac{(\tau_p \xi + \tau_l \psi)}{\tau_D}\right)^{-1}, \quad (1.26)$$

where τ_p and τ_l are the pixel dwell time and line time, and ξ and ψ are the spatial displacements (in pixels) in the horizontal and vertical direction of scan, respectively, by which the correlations are computed. τ_D denotes the average transit time of particles as a result of diffusion. Knowing τ_D and the width of the observation volume ω_0 , the diffusion coefficient D can be calculated from $\tau_D = \omega_0^2 / 4D$.

The scanning term $G_S(\xi, \psi)$ accounts for the displacement of the observation volume and is determined by [62]:

$$G_S(\xi, \psi) = \exp\left(-\frac{\left(\frac{2\xi\delta p}{\omega_0}\right)^2 + \left(\frac{2\psi\delta p}{\omega_0}\right)^2}{2\left[1 + \frac{(\tau_p \xi + \tau_l \psi)}{\tau_D}\right]}\right), \quad (1.27)$$

where δ_p denotes the pixel size. Finally, the kinetic term $G_K(\xi, \psi)$ takes into account the transitions of the dye to a dark state with a lifetime of 30–150 μs for the lipid-dye system [77]

$$G_K(\xi, \psi) = 1 + K \exp\left(-\frac{(\tau_p \xi + \tau_l \psi)}{\tau_K}\right), \quad (1.28)$$

where K denotes the amplitude of the kinetic term with dark-state lifetime τ_K .

Similar to STED-RICS, STED-FCS has been applied in several studies on biological membranes, including the study of compartmentalization of phospholipid

diffusion in the plasma membrane [78] and diffusion measurements of lipids and GPI-anchored proteins in actin-free plasma membrane [79]. As previously described for RICS, STED-RICS data can also be analyzed using number and brightness method [70] to determine the aggregation states of diffusing molecules [75]. Moreover, despite being technically challenging, dual color cross-correlation STED-RICS can be implemented for the study of interactions between two fluorescently labeled molecules [75].

1.2.4 Single Particle Tracking

The techniques that were discussed in previous sections provide ensemble average information on the dynamics of molecules. In contrast, single particle tracking (SPT) provides detailed information on the mobility of individual molecules with a spatial resolution that is limited by the signal to noise ratio of the particle, but typically falls within < 20 nm. SPT is usually performed on images acquired with a total internal reflection fluorescence (TIRF) microscope, where multiple images from the field of view are captured sequentially. The intensities of all the pixels in each frame are acquired simultaneously and isolated particles are captured for relatively long periods of time with frame rates up to 40 kHz [18]. The images are then analyzed to precisely locate the center of the emission profile of each fluorescent particle in every frame, and the trajectories are built by linking the positions of particles in consecutive frames. Mathematical analysis of the trajectories can then provide a quantitative estimation of the diffusion coefficient and useful insight into the type of motion under observation.

TIRF microscopy (Figure 1.18), also known as evanescent wave microscopy, enables imaging biological samples in an aqueous environment and observation of a thin region within a specimen, usually less than 200 nm, above the glass surface [80]. This is achieved by exciting only the fluorophores that are near the solid surface, while keeping the fluorophores that are far from the region of interest intact. Consequently, TIRF can reduce the background fluorescence, and minimize exposure of cells to light for live cell imaging [81]. For total internal reflection to occur, light must be traveling from a higher to a lower index of refraction media and the angle of incidence should be greater than the critical angle, given by $\theta_c = \sin^{-1}\left(\frac{n_2}{n_1}\right)$ (where $n_2 > n_1$, Figure 1.18). As light illuminates the specimen, it is internally reflected, creating an evanescent field above the

substrate surface (Figure 1.18). The exponentially decaying field produced in n_1 can excite fluorophores in a thin region near the surface while avoiding excitation of a large number of fluorophores farther from the surface. Examples of transparent medium n_2 are the glass coverslip and tissue culture plastic, while n_1 is a liquid medium such as water or the cell cytoplasm. The penetration depth created by the evanescent field can be calculated from:

$$d = \frac{\lambda_0}{4\pi(n_1^2 \sin^2 \theta - n_2^2)^{1/2}}, \quad (1.29)$$

where d is the penetration depth, λ_0 is the laser wavelength, θ is the incident angle, and n_1 and n_2 are the index of refraction for water and glass, respectively.

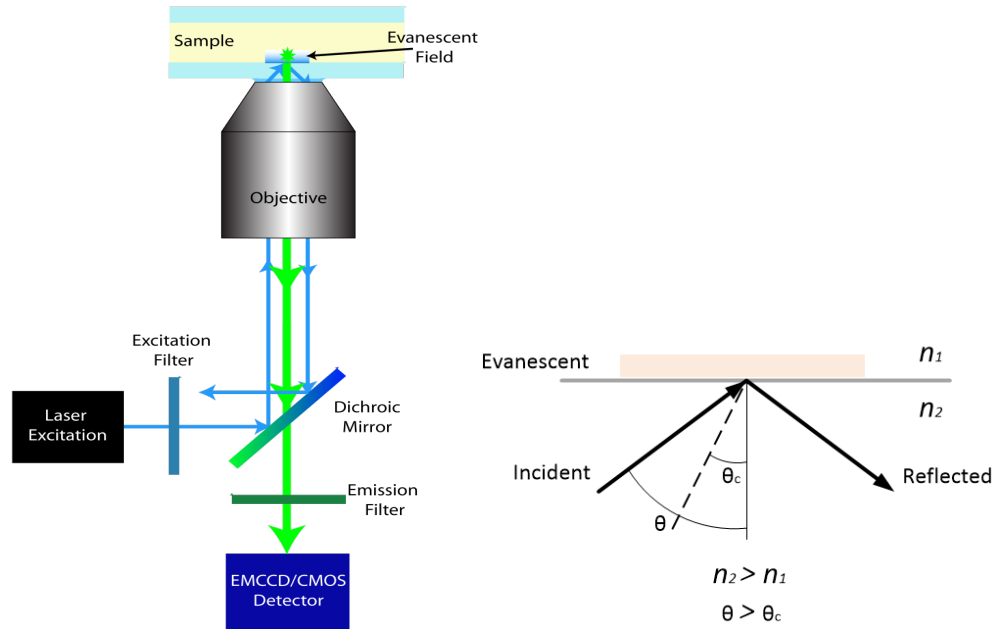


Figure 1.18 Total internal reflection microscope setup and evanescent field [82].

The raw data for SPT experiments consists of a time series of diffraction-limited images of the emission profile of fluorescent particles. The single particle tracking analysis can be then performed in four major steps described below: particle identification, particle localization, tracking, and analyzing the trajectories.

1) *Particle Identification*. Although recent developments in optics and cameras have minimized the noise generated in microscopy imaging, image processing using appropriate filters will simplify the computational work needed to distinguish features

from noise. Gaussian, Wiener, deconvolution, and top-hat filters are a few examples of prefiltering methods applied to images for single particle tracking analysis [83]. The particles are then identified from background noise using parameters such as the peak intensity, total intensity, radius of gyration, and eccentricity of particles [84].

2) *Particle Localization*. The particles or molecules visualized in SPT are usually smaller than the resolution of the microscope and appear as bright spots with intensity distributions that depend on the response of the optical system to a point source, known as the point-spread function. The emission from even the smallest single fluorophores spans over multiple pixels; therefore, a key step in SPT analysis is to localize fluorescent particles with sub-diffraction resolution. A rough estimation of the position of each particle can be obtained by searching for the pixel with the highest intensity value, which was traditionally performed manually or in a computer-assisted fashion [85]. Nowadays, image processing algorithms such as cross-correlation, sum-absolute difference (SAD), calculation of the center-of-mass (centroid) or Gaussian fitting [86] of the intensity profile to an approximation of the PSF can yield an accuracy of ~ 10 nm for localization of particles [87]. The pixel size of images is typically 30-150 nm depending on the magnification and the physical size of the pixels in the electron multiplying charge couple device (EMCCD) or scientific complementary metal-oxide-semiconductor (sCMOS) camera. Therefore, the centroid should be located to 1/3rd or 1/15th of a pixel in order to achieve an accuracy of 10 nm [87]. Figure 1.19 demonstrates how the accuracy of localization can be determined. Using weighted least-square fit to the data with a 2D Gaussian function the estimated centroid position can be found (Figure 1.19-C), along with the width of the emitter profile in the imaging plane. The difference between the average localization (green cross) and the actual particle position (red cross) gives the localization accuracy (Figure 1.19-E). In contrast, the localization precision refers to the standard deviation of the estimation of the particle's actual position around its mean, and can be commonly referred to as the localization "resolution" or uncertainty.

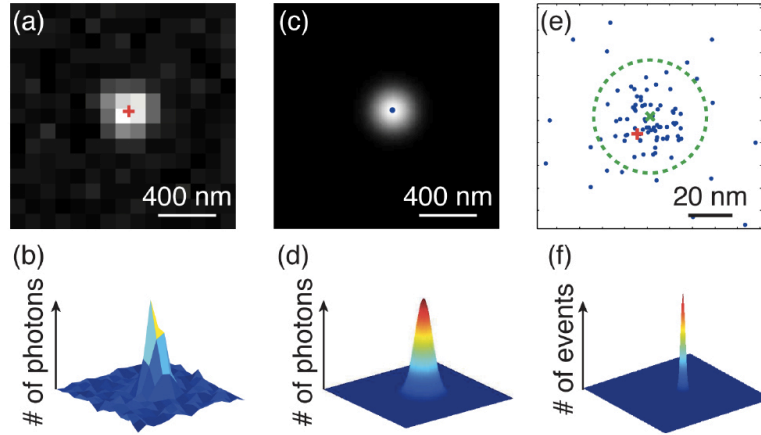


Figure 1.19 A) Simulated diffraction-limited image of an isotropic fluorescent emitter with Poisson noise and detector pixelation, the red cross represents the actual position of the emitter, B) photon count histogram of image A), C) and D) result of a weighted least-square fit to the data using a 2D Gaussian function with the blue dot denoting the estimated centroid position, E) estimate positions (blue dots) obtained from different images of the same emitter, the green cross in the center and the green circle denote the average of localizations and the standard deviation respectively, F) probability distribution of individual localizations [88].

3) *Tracking*. Once the particles' coordinates are found, an algorithm is needed to determine which particle in an image can be linked to a particle in a subsequent frame. When the particles are sparse enough, this can be achieved by linking the localizations based on the “nearest-neighbor distance” criterion. In this case, for each particle found in a given frame, its distance to all the localizations in the next frame are calculated and the pair with the minimum distance is selected as the most likely occurrence of the same particle in the following frame. The trajectories are reconstructed by performing this process for all the particles in each frame. However, the linking process is not straightforward as the particles may permanently or temporarily disappear due to blinking or photobleaching. The algorithm must take into account the possibility of these events and should stop generating linkages when no localizations are found within a given search radius.

At high densities, the complexity is further increased by the possibility of particles' trajectories crossing each other. As a result, the more advanced algorithms are based on multi-particle tracking, meaning that all the trajectories are simultaneously reconstructed and an optimization strategy is used to resolve the conflicts between competing linkages. In addition, information from multiple frames can be used to improve linking. In this

approach, building trajectories can be treated as a combinatorial optimization problem with a factorial complexity [89]. This requires a cost function or metric, including all linking possibilities, which must be minimized. In addition to particle coordinates, information about emitter intensity, PSF shape, and the type of motion can be incorporated in the linking algorithm to further increase tracking reliability [90,91]. To date, several tracking algorithms have been developed based on these approaches [89], [90,92–94]. Although most SPT algorithms have two separate steps for localization and tracking, recently developed programs are based on simultaneous detection and tracking of particles where the information from localizations in each frame are constantly used to update the detection and tracking of particles in successive frames [95].

4) *Analysis*. Once tracks of suitable lengths are generated, they must be analyzed to extract meaningful observables, such as particle speed or diffusion coefficient. The most common approach to analyze the trajectories, interpret, and classify the type of motion is the mean-squared displacement (MSD) analysis, which describes the average distance explored by a particle as a function of the time lag t_{lag} . For a particle j diffusing in 3D, if the position coordinates $\mathbf{x}_j = \{x_j, y_j, z_j\}$ are sampled at N discrete times, the MSD for a single trajectory is calculated as:

$$MSD(t_{lag} = m\Delta t) = \frac{1}{N-m} \sum_{i=1}^{N-m} [x_j(t_i + m\Delta t) - x_j(t_i)]^2. \quad (1.30)$$

For Brownian motion, the MSD can be related to the diffusion coefficient through the relation:

$$MSD(t_{lag}) = 2dDt_{lag}, \quad (1.31)$$

where D is the translational diffusion coefficient and d represents the dimensionality of the space in which the motion takes place.

For an SPT algorithm with random error in localization and tracking, the equation of the plot for Brownian motion in two dimensions is given by:

$$MSD(t_{lag}) = 4Dt_{lag} + 2\sigma^2, \quad (1.32)$$

where σ^2 is the variance of the experimental noise. The diffusion coefficient D can be determined from the slope of the plot (Figure 1.20-B). The MSD at large t_{lag} has poor

statistics and deviates from linearity. Estimation of the diffusion coefficient can be obtained from fitting to the short t_{lag} region of the MSD plot [96].

Other types of motion, such as anomalous diffusion and directed motion, are also commonly observed in biological systems and can be described by:

$$MSD(t_{lag}) = 2dKt_{lag}^a \quad (1.33)$$

$$MSD(t_{lag}) = 2dDt_{lag} + (vt_{lag})^2, \quad (1.34)$$

where K is a generalized diffusion constant, a is the anomalous exponent ($a > 1$ super-diffusion, $a < 1$ sub-diffusion), and v is the speed in an active transport such as molecular motors.

For restricted motion, the MSD cannot be defined without information of the exact shape of the confining region; however, confinements generally result in a plateau in the MSD curve at large t_{lag} , which can be mathematically described by:

$$MSD(t_{lag}) = \frac{L^2}{3} \left(1 - \exp\left(-\frac{t_{lag}}{\tau}\right) \right), \quad (1.35)$$

where L is the linear dimension of the confined region and τ represents a characteristic equilibrium time after which the effect of boundaries appears for diffusion in 2D.

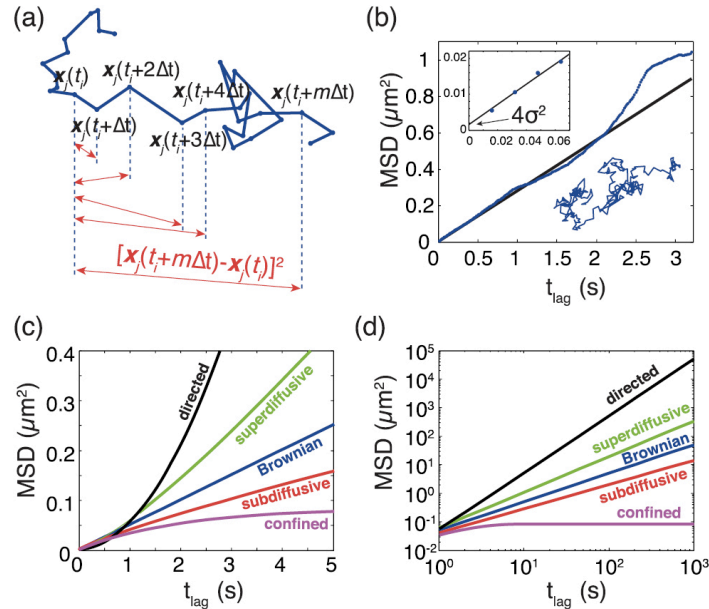


Figure 1.20 A) Calculation of the squared displacement of a 2D trajectory for a given initial time t_i and lag time, B) time averaged MSD for a single particle trajectory in 2D, C) MSD plot showing different types of diffusion, D) MSD plot in log-scale [88].

SPT has been utilized in numerous studies probing the dynamics of biological membranes. A few examples of these studies include the detection and tracking of phagocytic $\text{Fc}\gamma$ receptors ($\text{Fc}\gamma\text{R}$) on plasma membrane of macrophages [97,98], the transmembrane integrin mobility in monocytes [99,100], and the diffusion of lipids in epithelial cells [101]. In addition, SPT with multi-color imaging has been used in various experiments to study the interaction of two or more membrane components [98,100,102–104]. As demonstrated in the following examples, both single- and multi-color SPT not only uncover the trajectories of molecules in the plasma membrane but can also extract information about different populations of molecules undergoing different types of motion with dissimilar diffusion coefficients. Single molecule detection has been used to track the mobility of immunoreceptors to differentiate the immobile, slow, and fast diffusing receptors. As shown in Figure 1.21, the lateral mobility of the transmembrane integrin nanoclusters lymphocyte function-associated antigen 1 (LFA-1) was tracked on the plasma membrane of resting monocytes [99]. Trajectories of LFA-1 nanoclusters labeled with the neutral mAb TS2/4 (Figure 1.21-A) were generated from a series of movies through single molecule detection on an epifluorescence microscope. The individual trajectories revealed a large heterogeneity in lateral mobility of the nanoclusters, with a combination of highly mobile, slow, and restricted diffusive behavior (Figure 1.21-D). Diffusion coefficients of 10^{-3} to $10^{-1} \mu\text{m}^2/\text{s}$ and $\sim 5\%$ immobile fraction (Figure 1.21-E) were obtained from the analysis of individual trajectories using mean-squared displacement (MSD). The type of diffusion (Brownian, hindered, anomalous) was determined using applied cumulative probability distribution (CPD) and it was found that slow and fast diffusive nanoclusters (Figure 1.21-F) presented Brownian motion with diffusion coefficients of $D=1.4\pm 0.1\times 10^{-2} \mu\text{m}^2 \text{s}^{-1}$ and $D=5.6\pm 0.2\times 10^{-2} \mu\text{m}^2 \text{s}^{-1}$, respectively. This result indicates that the LFA-1 nanoclusters that are formed on resting monocytes prior to ligand binding are primarily mobile [99], in contrast to earlier reports of immobile LFA-1 in resting T cells [105,106].

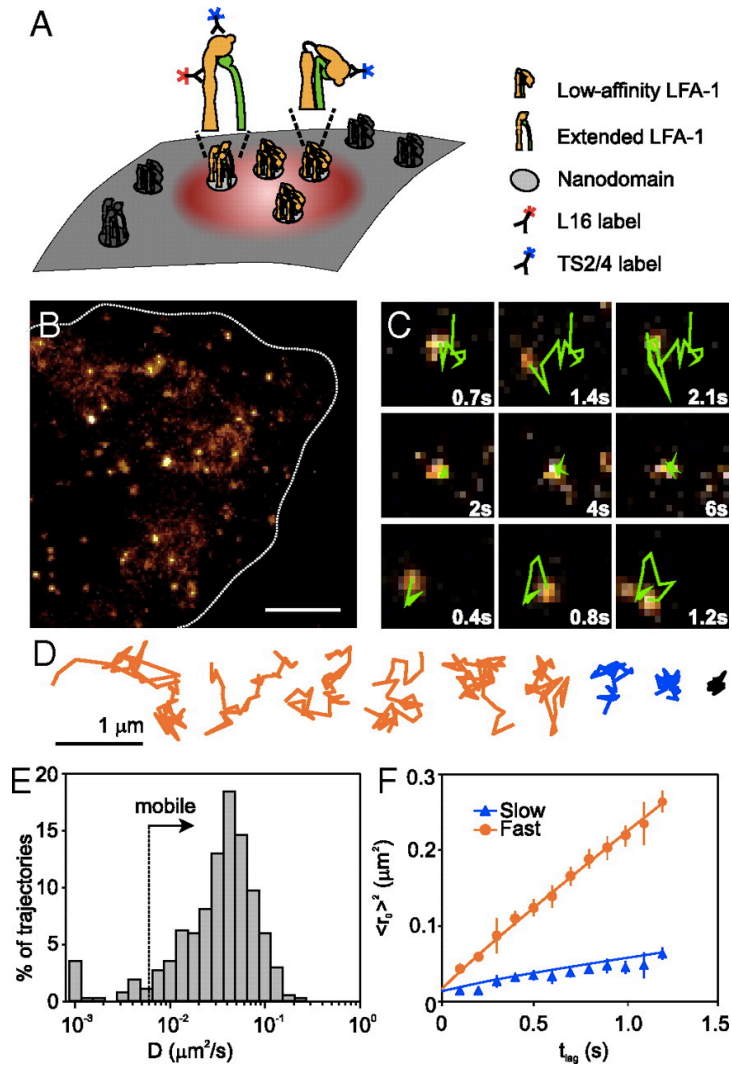


Figure 1.21 A) Schematic representation of LFA-1 nanoclusters diffusing randomly on resting monocytes, B) an image captured from a series of frames (100 ms per frame) showing the bright TS2/4-LFA-1 nanoclusters (scale bar= 5 μ m), C) selected time lapse images of LFA-1 nanoclusters for a fast (top), immobile (middle), and slow (bottom) diffusive behavior, D) selected trajectories of LFA-1 nanoclusters showing fast (orange), slow (blue), and immobile (black), E) normalized frequency distribution of diffusion calculated for 370 trajectories from 128 cells in multiple experiments, F) squared displacement of the mobile nanoclusters (157 trajectories) at different time lags calculated using cumulative probability distribution [99].

Multi-color single particle detection in TIRF mode has enabled visualization of the dynamics of multiple receptors simultaneously on the plasma membrane, as shown in Figure 1.22 for Jurkat, an immortalized human T-cell line. The dynamics of CD3 ϵ , a subunit of T cell receptor (TCR) microcluster, and CD45 were visualized on T cells expressing CD3 ζ -EGFP (a marker protein for TCR). The cells were immobilized onto a glass surface using biotinylated anti-CD3 ϵ antibodies, streptavidin, and lipid bilayer

in order to preserve the intrinsic mobility of membrane proteins [107]. CD3 ζ -EGFP (green), quantum dot (Qdot) 655-labeled CD3 ϵ (red), and Qdot 585-labeled CD45 (blue) were visualized in the fluorescence images (Figure 1.22-B). Qdots were chosen for fluorescent labeling as they enable clear visualization of single molecules as well as tracking for extended period of time [108]. The diffusion was measured at different regions of TCR microclusters (*i.e.*, inside, outside, and boundary), and the distributions of diffusion coefficients of CD3 ϵ and CD45 were fitted by the dual-normal distribution corresponding to the two-state diffusion model (Figure 1.23) [109]. The multi-color single molecule tracking revealed that the mobility of CD3 ϵ and CD45 molecules were faster outside and at the boundary of the microclusters than inside these domains.

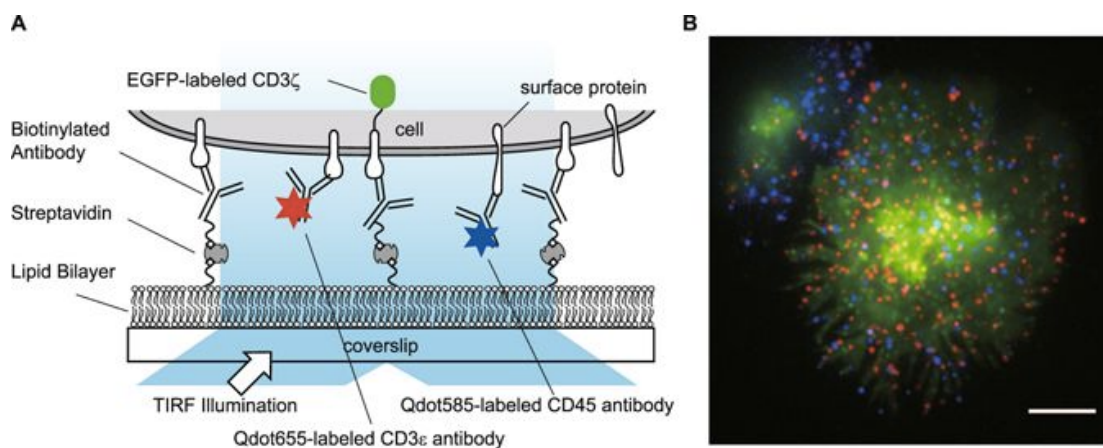


Figure 1.22 A) Schematic representation of a T cell expressing CD3 ζ -EGFP immobilized onto a glass surface using biotinylated anti-CD3 ϵ antibodies and planar lipid bilayers, B) TIRF image of three-color single molecule tracking of CD3 ζ -EGFP (green), Qdot 655-labeled CD3 ϵ (red), and Qdot 585-labeled CD45 (blue) in live Jurkat T cells. Scale bar: 5 μ m [109].

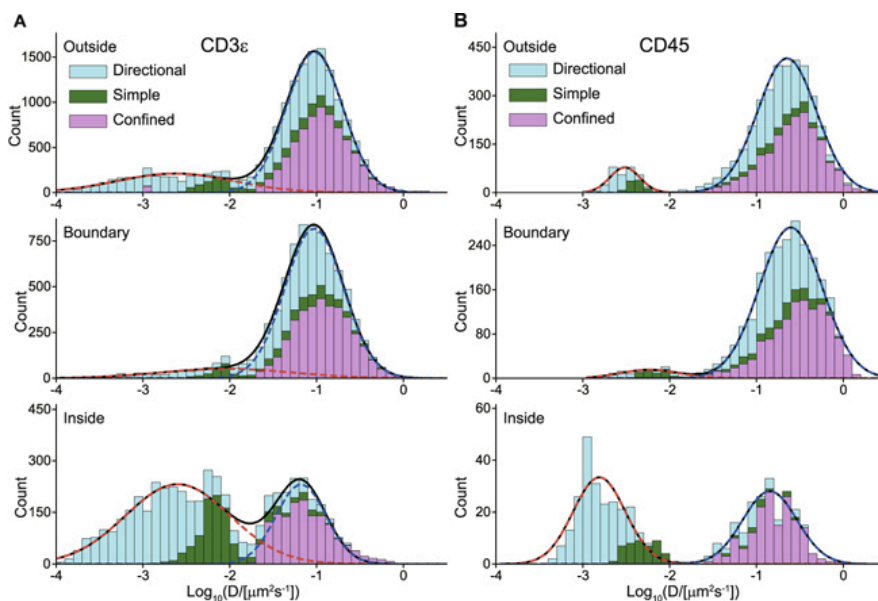


Figure 1.23 A) CD3 ϵ , and B) CD45 mobility states are shown using logarithmic scale distributions of the diffusion coefficients obtained from inside, at the boundary, and outside of the microclusters on immobilized T cells, using moving sub-trajectory analysis [109]. Three types of diffusion were present: simple (green), directional (cyan), and confined (magenta). The histograms of the three diffusion types were fitted by the dual normal distribution (black line), which consist the slow (dashed line, red) and fast (dashed line, blue) diffusion [109].

Multi-color SPT can also reveal correlations between diffusing molecules such as protein-protein interactions within the plasma membrane. Co-localization, as the name of the technique implies, is based on localization of molecules moving together since co-diffusion is indicative of a physical link or indirect interaction between two molecules. Information about the duration of the interaction can be extracted from the length of time in which the trajectories of two molecules exhibit correlated motion. Dual-color SPT has been applied in several investigations to visualize the dynamic interactions of membrane receptors [100,102,110,111]. The real-time dynamic observation of CD9 co-localization on the plasma membrane of PC3, human prostatic carcinoma cell line, is illustrated in Figure 1.24 [112]. Two molecules were considered to have co-diffusion when there was an overlap of their fluorescence signal for at least one pixel during seven frames (700 ms). The co-localization results of CD9 were classified as Brownian diffusion, similar to the motion of isolated CD9 molecules, with no significant change in diffusion coefficient of CD9-CD9 complex [112].

SPT studies described in this chapter demonstrate the importance of deciphering single molecule behavior to understand the interactions of membrane constituents. The main limitation of using TIRF microscopy for SPT experiments is that only the basal membrane of cells adhered to the surface can be excited within the narrow evanescent field, and the apical membrane and cytoplasm cannot be examined. To overcome this limitation, highly inclined and laminated optical (HILO) sheet illumination is implemented [113], which makes use of a large refraction to create a highly inclined incident beam that is laminated as a thin optical section at the specimen. This results in the reduction of background fluorescence since only a thin layer of the cell is illuminated; however, it can be applied only in the center of the object field with a limited depth range. Additionally, SPT requires sparse labeling for particle localization as the molecular separations have to be larger than the particle's diffraction-limited size. However, SPT is continuously going through tremendous expansion, benefiting from development of advanced optical techniques and enhanced labeling strategies to facilitate more precise tracking of individual molecules at the nanoscale.

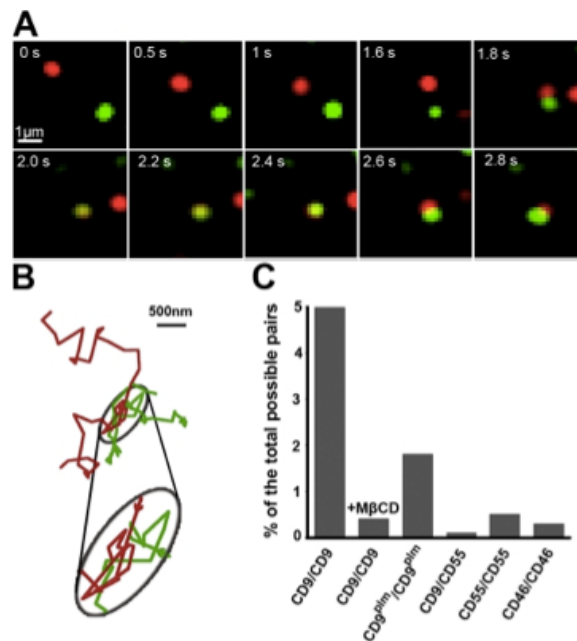


Figure 1.24 A) Time lapse showing a simultaneous single-molecule tracking of two spectrally distinct labeled CD9 molecules using a Fab fragment conjugated with Atto647N (red) or with Cy3B (green), B) Representative trajectories of CD9 co-localization where the fluorescence signal of two particles overlap at least for one pixel (160 nm), C) Different combinations of proteins were tested: CD9/CD9 on cells with/without treatment with MβCD, CD9^{plm}/CD9^{plm}, and irrelevant pairs such as CD9/CD55, CD55/CD55, and CD46/CD46 [112].

information on diffusion behavior, spatial distribution, and type of confinement, all in one experiment. In addition, point-FRAP coupled with FCS has been performed for precise quantification of diffusion and binding [121], while single molecule illumination combined with single molecule fluorescence recovery after photobleaching (smFRAP) has been used to determine diffusion coefficients with a spatial resolution of <10 nm [122]. Non-optical techniques such as atomic force microscopy (AFM) can also be combined with fluorescence microscopy techniques to examine the integration of lipid membranes upon contact, using AFM-FCS [123] and AFM-SPT [124]. These combined techniques not only can provide simultaneous access to a wealth of information on transport and binding in the membrane, but can also enable ensemble averaging and single particle measurements to be performed on a given sample in one experiment; therefore, they can serve as complementary tools to describe the behavior of membrane components.

With the advent of super-resolution optical microscopy methods such as single-molecule localization methods, stimulated emission depletion (STED), and near-field scanning optical microscopy (NSOM), new combinations of fluorescence-based techniques are expected to emerge. As described in Section 1.2.3-6, STED-FCS and STED-RICS have been developed to improve the spatial resolution down to ~ 40 nm [75]. Similarly, NSOM has been combined with FCS to detect anomalous diffusion on cell membranes with spatial resolution of 120 nm [125]. On the other hand, structured illumination microscopy (SIM) [126,127] increases the resolution by exploiting interference patterns from a series of excitation light illuminated through two grids overlaid at an angle. This technique doubles the resolution of traditional light microscopy and is rapidly gaining in popularity. In addition, photonic nanostructures have been developed that can confine illumination on a sub-wavelength scale to reach sub-diffraction volumes, using nanometric apertures with radii of 50 nm to 250 nm milled in a metallic film, known as zero mode waveguides (ZMWs) [128]. This method has been combined with FCS to probe model lipid membranes [129,130] and cell membranes [131,132]. All these approaches can overcome the diffraction limit and enable visualization with a higher resolution compared with conventional light microscopy techniques.

A number of comparative studies have been conducted to determine the accuracy and differences in diffusion measurements obtained from different techniques, which helps inform on the advantages and limitations for each technique. FCS and FRAP have been compared on the same lipid membrane section by simultaneous measurements acquired from both techniques [29]. This direct comparison enabled the detection of transient changes in molecular diffusion induced by the FRAP bleaching pulse. The discrepancies in the diffusion coefficient obtained from these two methods were attributed to the bleach correction and fitting, which introduce large uncertainties in FRAP results [29]. Similarly, a comparison of diffusion measurements by line-scanning FCS and SPT on a supported lipid bilayer has shown statistically significant difference ($D_{\text{FCS}} = 3.4 \pm 0.4 \mu\text{m}^2 \text{s}^{-1}$ vs. $D_{\text{SPT}} = 2.4 \pm 0.3 \mu\text{m}^2 \text{s}^{-1}$) that result from the limited dynamic range of each technique, *i.e.*, FCS range > actual diffusion > SPT range, yielding an underestimated D_{SPT} and an overestimated D_{FCS} [133]. In contrast, in a different study on SPT and ITIR-FCS, comparable results were obtained from these techniques with respect to the diffusion coefficients extracted from different types of motions [120]. On the other hand, it is reported that FCS yields higher diffusion coefficients compared with RICS ($D_{\text{FCS}} = 10.0 \pm 0.7 \mu\text{m}^2 \text{s}^{-1}$ vs. $D_{\text{RICS}} = 8 \pm 2 \mu\text{m}^2 \text{s}^{-1}$), with both measurements taken from the membrane of giant unilamellar vesicles [134]. This discrepancy was attributed to membrane curvature in vesicles, which can cause the scanning illumination volume to cross irregular portions of the membrane. An earlier comparative study on FCS, FRAP, SPT, and ITIR-FCS applied to supported lipid bilayer showed that diffusion measurements obtained from these techniques were within the same range [115]. Direct comparison of different methods for measuring diffusion is not trivial, as several factors such as concentration of molecules, detection of immobile particles, and the accessible dynamic ranges for each technique must be taken into account. For example, the required molecular concentration for SPT is much lower than FCS, *i.e.*, $N \ll 1$ vs. $1 \leq N \leq 10$, respectively [133,135]. Consequently, SPT and FCS can be compared only if the chosen concentration is in the higher range of what SPT can measure, and in the lower range of FCS detection limit [133]. Each technique has their specific strengths, and the choice of method depends on the particular application. The results of these

comparative studies can help with the selection of appropriate techniques for specific measurements on the membranes.

Despite rapid advances in fluorescence microscopy, a number of challenges still remain that can impact measurements of biological membranes. To date, analysis of biological membrane components using fluorescence microscopy techniques has been limited to a very small number of fluorophores. Only two or three molecular targets can be distinguished and analyzed simultaneously in a given sample due to spectral overlap between different fluorophores and fluorescent proteins. However, the cell is crowded with multiple types of macromolecules and their spatial relations and interactions should be determined in order to fully understand the underlying mechanisms of various biological events. To reduce the spectral crosstalk in fluorescence imaging, alternating the lasers with different excitation wavelengths can be a feasible solution for dual-color imaging [136]; however, the complexity of the set-up increases when adding more colors. Qdots are more frequently used to label three or more target molecules because of their narrow emission spectra [88], although spectrally separated cameras are required [137]. A limitation of Qdots is their relatively large size (typically ~15-20 nm in diameter) compared with organic dyes, which lead to steric hindrance and reduced mobility of receptor-label complex [138]. Moreover, the blinking of Qdots makes single particle tracking more challenging as their abrupt dark state can terminate the tracking. Further advancements in fluorescence probes are envisioned to overcome these challenges in the near future, through development of fluorophores of different colors and emission spectra that can be excited with similar wavelength.

Over the past few decades, fluorescence microscopy techniques have received much attention in areas of medical sciences such as proteomic, immunofluorescence, and genomic sequencing. These techniques have led to significant discoveries related to the function, structure, and binding interactions [68] of proteins and molecular motors [139], the clustering of immunoreceptors and their signaling cascades [98,140,141], and chromosome segregation [142,143], transcription [144], translation [145], replication [146], and DNA repair [144,147], just to name a few. It must be highlighted that the fluorescence microscopy techniques discussed in this chapter are not limited to the characterization of mammalian cells and have been frequently

utilized in studies on bacterial membrane proteins [148–151] and plant cells [152,153]. Thus, advanced fluorescence microscopy techniques enable visualization of real-time dynamics in all biological membranes at the molecular level and provide quantitative information that can enhance our understanding of these subcellular observations.

1.4 Macrophages

1.4.1 Origins and Phenotypes

The immune response to microbial pathogens relies on both the innate and adaptive mechanisms. The immediate, innate response is predominantly dependent on leukocytes (white blood cells), such as neutrophils and macrophages that have the ability to phagocytose (see Section 1.4.2) and kill pathogens. Macrophages are specialized in the detection, engulfment, and destroying target cells and are evolutionary conserved phagocytes that evolved more than 500 million years ago [154].

Based on their origin, macrophages are classified into two general groups of tissue-resident and monocyte-derived macrophages [155]. Each tissue has its own composition of resident macrophages, originated from the early gestation period during embryonic development. In contrast, monocytes are a heterogeneous population of mononuclear phagocytes that arise from hematopoietic stem cells (HSCs) in the bone marrow and are constantly released into the bloodstream to patrol the vasculature throughout the body. Monocytes constitute 1-6% of total leukocytes in healthy peripheral blood with a half-life of approximately 70 hours [156]. These cells differentiate into macrophages or dendritic cells after migrating into tissues and to the sites of damage or infection in response to chemotactic signals.

Macrophages are also classified based on their phenotypic roles in pro- or anti-inflammatory responses. M1 macrophages, also known as classically activated phenotype, and M2 macrophages known as alternatively activated are the two ends of a wide spectrum of phenotypic variations [157]. Upon stimulation with pathogens, macrophages polarize toward M1 phenotype and secrete pro-inflammatory cytokines to recruit other immune cells. In response to wound healing cytokines, macrophages polarize toward M2 phenotype to alleviate inflammation, and to promote angiogenesis, cell proliferation, and ECM remodelling for tissue repair. The *in vitro* polarization of M1 macrophages is

typically induced by exposure to interferon-gamma (IFN- γ) and lipopolysaccharide (LPS), whereas M2 macrophages can be activated upon stimulation with interleukin-4 (IL-4) or IL-13 [158]. To identify their activation state, macrophages are commonly characterized based on the expression of cellular markers (M1 marker: CD86; M2 marker: CD163), cytokine profile (M1 releases IL1 β and tumor necrosis factor alpha (TNF α); M2 releases IL-10 and C-C motif chemokine ligand 18 (CCL18) [159].

1.4.2 Phagocytosis

The complex and versatile phagocytic process is central to elimination of pathogens as well as tissue homeostasis and remodelling. Phagocytosis is the ingestion of particles larger than 0.5 μm into membrane-bound vacuoles known as phagosomes. The phagocytic process begins with the engagement of receptor(s) with their cognate ligand(s) followed by clustering of receptors at the site of ligand. This process is accompanied by the disruption of cortical cytoskeleton and F-actin remodelling to create a specialized membrane structure known as phagocytic cup [160]. The cup will then wrap around the particle, fuse, and seal into a completely internalized phagosome. The phagosome experiences a process of maturation and acidification (the pH drops from 7.4 to \sim 6.5) [161], which results in the degradation of its contents as well as generation of peptides that can be presented to the cells of the adaptive arm of immunity [162]. Opsonic phagocytosis is referred to conditions where the ligand is coated with complement or immunoglobulin G (IgG) that involve the complement receptor 3 or Fc γ receptors. Phagocytosis is performed by both “professional” and “non-professional” phagocytes [163]; a classification that is based on the efficiency of the phagocytic function in a wide range of cells capable of engulfing particles. Professional phagocytes include neutrophils, monocytes, macrophages, dendritic cells, osteoclasts, and eosinophils [164]. Non-professional phagocytes are cells that normally do not phagocytose large particles but can develop the ability to internalize targets under certain conditions, such as engulfing proximal apoptotic and necrotic cells [165,166] as seen in epithelial, endothelial, fibroblast, and mesenchymal cells [164]. Professional phagocytes such as macrophages can be distinguished by their versatile repertoire of membrane-bound receptors that can recognize, engage, and initiate phagocytosis.

1.4.3 Plasma Membrane Receptors

Macrophages express a diverse range of plasma membrane receptors that regulate a variety of functions, including migration, adhesion, recognition of pathogens, phagocytosis, and activation of inflammatory responses [167]. Recognition is an essential component in generating the appropriate immune response against invading pathogens as well as in the elimination of altered host components such as damaged or apoptotic cells. Pattern recognition receptors (PRRs) are proteins that can identify two classes of invariant molecular patterns: pathogen associated molecular patterns (PAMPs) and damage associated molecular patterns (DAMPs). Upon activation, PRRs can signal danger to initiate early host defense by the innate immune system and can induce antigen presenting cells (APCs) to present antigens to the cells recruited for the adaptive immune response. Pattern recognition receptors in phagocytes are categorized into two main classes based on their role in phagocytic function or the activation of pro-inflammatory pathways [168,169]. In a comprehensive review by Taylor *et al.*, the receptor families in macrophages and their functions are explained in detail [167]. Here, we reiterate the structure and function of a transmembrane and a membrane-anchored receptor, which have been the main focus of the studies described in this thesis.

1.4.3-1 Toll-Like Receptors – TLR2

Toll-like receptors (TLR) are pattern recognition receptors that play a key role in the innate immune system by participating in the inflammatory responses accompanied by detection of pathogens and microbial internalization [170]. The receptor's name originated from its similarity to “Toll”, a gene first identified in the fruit fly *Drosophila melanogaster*. The gene received this name after Dr. Christiane Nusslein-Volhard exclaimed, “Toll!” (translated as “amazing” in German), when Eric Wieschaus showed her the abnormal ventral portion of the mutant fruit fly larva [171].

TLRs are type I transmembrane glycoproteins composed of extracellular, transmembrane, and intracellular signaling domains [172]. These receptors are able to distinguish between self and non-self molecules, and their ligands include LPS, lipopeptides, DNA, RNA, and other components of viruses, fungi, bacteria, and protozoa. To date, 13 TLRs (10 in human) have been identified that can activate a signaling cascade in response to structurally distinct stimuli: bacterial lipoproteins are

recognized by either TLR1/2 or TLR2/6 heterodimer complexes, viral double-stranded RNA is recognized by TLR3, the endotoxin LPS from Gram-negative bacteria is recognized by TLR4, TLR5 recognizes flagellin proteins from bacteria, and TLRs 7–9 detect nucleic acids of bacterial or viral origin [173]. In the absence of TLRs, other receptors cannot adequately cope with most infections [174].

Among TLR family, TLR2 is the main innate immune receptor responsible for detecting the anchor motif of bacterial lipoproteins, present on the surface of all bacteria [175]. TLR2 responds to lipid-containing PAMPs such as lipoteichoic acid from Gram-positive bacteria and di- and tri-acylated cysteine-containing lipopeptides [176]. TLR2 receptor forms a TLR-ligand complex and initiates signaling through dimerization with TLR1 and TLR6 [172]. Agonist-TLR2 interaction is also influenced by coreceptors such as the cluster of differentiation 14 (CD14), CD36, and integrins [177].

1.4.3-2 CD14 Receptor

Cluster of differentiation 14 (CD14), expressed primarily on the surface of myeloid cells, exhibits many characteristics of PRRs and binds components of both gram-negative and gram-positive bacterial membranes [178]. It is a member of the family of leucine-rich repeat proteins with three sites for N-glycosylation that are occupied by oligosaccharides essential for protein secretion. CD14 is expressed as glycosylphosphatidylinositol (GPI)-linked membrane or soluble glycoprotein.

CD14 is a coreceptor for TLR4, TLR2 and other TLRs. Both its soluble and membrane bound forms bind LPS and present it to TLR, although membrane-bound CD14 is more potent [179]. CD14 also activates other TLRs that are involved in the innate immune response to different microbial products [177]. For example, CD14 binding to triacylated lipopeptides enhances signaling through the TLR1/2 complex by reducing the physical proximity of the ligand to the heterodimers for more efficient delivery of the microbial component to the TLRs, without binding directly to the TLRs [180]. The membrane-bound CD14 has only a few amino acids in its GPI tail (C-terminal sequence 28-32 amino acids) and until recently was not believed to facilitate TLR signaling [181]. More recently it has been shown to facilitate internalization of TLR ligands [182].

1.5 Research Objectives

This thesis aims to answer three major research questions with regard to the lateral diffusion of TLR2 and CD14 on the plasma membrane of macrophages, in the context of fluorescence microscopy techniques, the interactions of cells with surface structures, and age-related changes in macrophages. These questions are:

- 1) What is the most appropriate technique to measure the lateral diffusion of TLR2 and CD14 on macrophage plasma membrane? Do these receptors have significantly different diffusion coefficients? Is there significant difference in their diffusion in the apical and basal membrane sections for adhered macrophages?
- 2) Does culturing macrophages on micro- and nanostructured surfaces impact the diffusion of TLR2 in the plasma membrane and their pro-inflammatory response? How does morphology and phagocytic capacity change when cells are cultured on different glassy surface topographies?
- 3) Does aging alter the lateral diffusion of TLR2 in the plasma membrane of macrophages? Is there any significant difference in the phagocytic capacity of young and aged macrophages?

1.6 Overview

The following chapters provide answers to the research questions listed in Section 1.5:

Chapter 2 addresses research question 1) through comparison of diffusion measurements obtained from two well-established microscopy techniques, single particle tracking and raster image correlation spectroscopy.

Chapter 3 focuses on the interactions of macrophages with glassy surface topographies and provides answers to research question 2) through complex analysis of cell morphology, phagocytic capacity, inflammatory responses, and plasma membrane receptor diffusion for macrophages cultured on micro- and nanostructured silica surfaces.

Chapter 4 answers research question 3) through focusing on age-associated changes in the diffusion of TLR2 and phagocytic ability of macrophages with regard to internalization of the bacteria *Streptococcus pneumoniae*.

Chapter 5 provides a summary of the key findings and the conclusions of this work, the contributions to the field, and future directions.

1.7 References

- [1] D. Sadava, H. C. Heller, G. H. Orians, W. K. Purves, and D. M. Hillis, *Life The Science of Biology 8th Edition*. 2008.
- [2] P. A. Janmey and P. K. J. Kinnunen, “Biophysical properties of lipids and dynamic membranes,” *Trends Cell Biol.*, vol. 16, no. 10, pp. 538–546, 2006.
- [3] E. Gorter, F. Grendel, “On bimolecular layers of lipoids on the chromocytes of the blood,” *J. Exp. Med.*, vol. 41, no. 4, pp. 439–443, 1925.
- [4] S. J. J. Singer and G. L. L. Nicolson, “The fluid mosaic model of the structure of cell membranes,” *Science*, vol. 175, no. 4023, pp. 720–731, 1972.
- [5] J. F. Danielli and H. Davson, “A contribution to the theory of permeability of thin films,” *J. Cell. Comp. Physiol.*, vol. 5, no. 4, pp. 495–508, 1935.
- [6] K. Simons and G. van Meer, “Lipid sorting in epithelial cells.,” *Biochemistry.*, vol. 27, pp. 6197–6202, 1988.
- [7] S. Munro, “Lipid Rafts: Elusive or Illusive?,” *Cell*, vol. 115, pp. 377–388, 2003.
- [8] G. M. Cooper, *The Cell: A Molecular Approach.*, 2nd ed. 2000.
- [9] J. Bigay and B. Antonny, “Curvature, Lipid Packing, and Electrostatics of Membrane Organelles: Defining Cellular Territories in Determining Specificity,” *Dev. Cell*, vol. 23, no. 5, pp. 886–895, 2012.
- [10] J. Middleton Boon and B. D. Smith, “Chemical control of phospholipid distribution across bilayer membranes,” *Med. Res. Rev.*, vol. 22, no. 3, pp. 251–281, 2002.
- [11] L. Frye and M. Edidin, “The Rapid Intermixing of Cell Surface Antigens After Formation of Mouse-Human Heterokaryons,” *J. Cell Sci.*, vol. 7, pp. 319–335, 1970.
- [12] A. Kusumi *et al.*, “Paradigm shift of the plasma membrane concept from the two-dimensional continuum fluid to the partitioned fluid: high-speed single-molecule tracking of membrane molecules.,” *Annu. Rev. Biophys. Biomol. Struct.*, vol. 34, pp. 351–78, 2005.
- [13] A. Ganguly, S; Pucadyil, T; Chattopadhyay, “Actin cytoskeleton-dependent dynamics of the human serotonin(1A) receptor correlates with receptor signaling.,” *Biophys. J.*, vol. 95, pp. 451–463, 2008.

- [14] I. Chung, R. Akita, R. Vandlen, D. Toomre, J. Schlessinger, & I. Mellman, “Spatial control of EGF receptor activation by reversible dimerization on living cells.,” *Nature*, vol. 464, pp. 783–787, 2010.
- [15] D. M. Dupuy, A.D. and Engelman, “Protein area occupancy at the center of the red blood cell membrane.,” *Proc. Natl. Acad. Sci. U.S.A.*, vol. 105, pp. 2848–2852, 2008.
- [16] S. McLaughlin and D. Murray, “Plasma membrane phosphoinositide organization by protein electrostatics.,” *Nature*, vol. 438, pp. 605–611, 2005.
- [17] W. S. Trimble and S. Grinstein, “Barriers to the free diffusion of proteins and lipids in the plasma membrane,” *J. Cell Biol.*, vol. 208, no. 3, pp. 259–271, 2015.
- [18] T. Fujiwara, K. Ritchie, H. Murakoshi, K. Jacobson, and A. Kusumi, “Phospholipids undergo hop diffusion in compartmentalized cell membrane.,” *J. Cell Biol.*, vol. 157, pp. 1071–1082, 2002.
- [19] K. Suzuki, T. Fujiwara, F. Sanematsu, R. Iino, M. Edidin, and A. Kusumi, “GPI-anchored receptor clusters transiently recruit Lyn and Ga for temporary cluster immobilization and Lyn activation: single-molecule tracking study,” *J. Cell Biol.*, vol. 177, pp. 717–730, 2007.
- [20] K. Ritchie, R. Iino, T. Fujiwara, K. Murase, and A. Kusumi, “The fence and picket structure of the plasma membrane of live cells as revealed by single molecule techniques (Review),” *Mol. Membr. Biol.*, vol. 20, no. 1, pp. 13–18, 2003.
- [21] D. Gulino-Debrac, “Mechanotransduction at the basis of endothelial barrier function,” *Tissue Barriers*, vol. 1, no. 2, p. e24180, 2013.
- [22] S. Carrasco and T. Meyer, “STIM proteins and the endoplasmic reticulum-plasma membrane junctions,” *Annu. Rev. Biochem.*, vol. 80, pp. 973–1000, 2011.
- [23] A. A. Rowland and G. K. Voeltz, “Endoplasmic reticulum-mitochondria contacts: function of the junction.,” *Nat. Rev. Mol. Cell Biol.*, vol. 13, pp. 607–625, 2012.
- [24] C. Hönscher and C. Ungermann, “A close-up view of membrane contact sites between the endoplasmic reticulum and the endolysosomal system: from yeast to man.,” *Crit. Rev. Biochem. Mol. Biol.*, vol. 49, pp. 262–268, 2014.
- [25] M. J. Paszek *et al.*, “The cancer glycocalyx mechanically primes integrin-mediated growth and survival.,” *Nature*, vol. 511, pp. 319–325, 2014.

- [26] J. Lippincott-schwartz, E. Snapp, and A. Kenworthy, “Studying protein dynamics in living cells,” *Nat. Rev. Mol. Cell Biol.*, vol. 2, no. 6, pp. 444–456, 2001.
- [27] A. Carisey, M. Stroud, R. Tsang, and C. Ballestrem, “Fluorescence Recovery After Photobleaching,” *Methods Mol. Biol.*, vol. 769, pp. 387–402, 2011.
- [28] D. M. Soumpasis, “Brief Communication theoretical analysis of fluorescence photobleaching recovery experiments,” *Biophys. J.*, vol. 41, no. 1, pp. 95–97, 1983.
- [29] M. Radek, Y. H. Foo, and T. Wohland, “Article On the Equivalence of FCS and FRAP : Simultaneous Lipid Membrane Measurements,” pp. 152–161, 2016.
- [30] K. Hildick, I. González-González, F. Jaskolski, and J. Henley, “Lateral diffusion and exocytosis of membrane proteins in cultured neurons assessed using fluorescence recovery and fluorescence-loss photobleaching.,” *J. Vis. Exp.*, vol. 60, p. e3747, 2012.
- [31] J. R. Lakowicz, *Principles of Fluorescence Spectroscopy*, Third Edit. 2006.
- [32] D. Magde, E. Elson, and W. Webb, “Thermodynamic fluctuations in a reacting system: measurement by fluorescence correlation spectroscopy,” *Phys. Rev. Lett.*, vol. 29, pp. 705–8, 1972.
- [33] D. Magde, E. L. Elson, and W.W. Webb, “Fluorescence correlation spectroscopy. II. An experimental realization.,” *Biopolymers*, vol. 13, no. 1, pp. 29–61, 1974.
- [34] M. A. Digman and E. Gratton, “Lessons in Fluctuation Correlation Spectroscopy,” *Annu. Rev. Phys. Chem. Vol 62*, vol. 62, no. December, pp. 645–668, 2011.
- [35] É. Nagy *et al.*, “Membrane Potential Distinctly Modulates Mobility and Signaling of IL-2 and IL-15 Receptors in T Cells.,” *Biophys. J.*, vol. 114, no. 10, pp. 2473–2482, 2018.
- [36] E. Staaf, S. Bagawath-Singh, and S. Johansson, “Molecular Diffusion in Plasma Membranes of Primary Lymphocytes Measured by Fluorescence Correlation Spectroscopy,” *J. Vis. Exp.*, vol. 120, p. e54756, 2017.
- [37] Y. Takahashi *et al.*, “Detection of polyglutamine protein oligomers in cells by fluorescence correlation spectroscopy,” *J. Biol. Chem.*, vol. 282, no. 33, pp. 24039–48, 2007.
- [38] L. E. Kilpatrick and S. J. Hill, “The use of fluorescence correlation spectroscopy to

- characterize the molecular mobility of fluorescently labelled G protein-coupled receptors,” *Biochem. Soc. Trans.*, vol. 44, no. 2, pp. 624–9, 2016.
- [39] M. A. Digman, P. Sengupta, P. W. Wiseman, C. M. Brown, A. R. Horwitz, and E. Gratton, “Fluctuation correlation spectroscopy with a laser-scanning microscope: exploiting the hidden time structure.,” *Biophys. J.*, vol. 88, no. 5, pp. L33-6, 2005.
- [40] L. Vasconcelos *et al.*, “Simultaneous membrane interaction of amphipathic peptide monomers, self-aggregates and cargo complexes detected by fluorescence correlation spectroscopy.,” *Biochim. Biophys. Acta - Biomembr.*, vol. 1860, no. 2, pp. 491–504, 2018.
- [41] P. Simeonov, W. S. C. Haupt, M. Tanabe, and K. Bacia, “Membrane protein reconstitution into liposomes guided by dual-color fluorescence cross-correlation spectroscopy,” *Biophys. Chem.*, vol. 184, pp. 37–43, 2013.
- [42] A. J. García-Sáez, J. Ries, M. Orzáez, E. Pérez-Payà, and P. Schwille, “Membrane promotes tBID interaction with BCL(XL),” *Nat. Struct. Mol. Biol.*, vol. 16, no. 11, pp. 1178–1185, 2009.
- [43] J. Ries, Z. Petrášek, A. J. García-Sáez, and P. Schwille, “A comprehensive framework for fluorescence cross-correlation spectroscopy,” *New J. Phys.*, vol. 12, p. 113009(32), 2010.
- [44] J. Ries and P. Schwille, “New concepts for fluorescence correlation spectroscopy on membranes,” *Phys. Chem. Chem. Phys.*, vol. 10, pp. 3487–3497, 2008.
- [45] R. M. Dörlich *et al.*, “Dual-color dual-focus line-scanning FCS for quantitative analysis of receptor-ligand interactions in living specimens,” *Sci. Rep.*, vol. 5, p. 10149, 2015.
- [46] N. O. Petersen, “Scanning fluorescence correlation spectroscopy. I. Theory and simulation of aggregation measurements.,” *Biophys. J.*, vol. 49, pp. 809–815, 1986.
- [47] N. Petersen, P. L. Hddelius, P. W. Wiseman, and O. Seger, “Quantitation of Membrane Receptor Distributions by Image Correlation Spectroscopy : Concept and Application,” vol. 65, no. September, pp. 1135–1146, 1993.
- [48] N. O. Petersen, C. Brown, A. Kaminski, J. Rocheleau, M. Srivastave, and P. W. Wiseman, “Analysis of membrane protein cluster densities and sizes in situ by

- image correlation spectroscopy,” *Faraday Discuss*, vol. 111, pp. 289–305, 1998.
- [49] D. L. Kolin, D. Ronis, and P. W. Wiseman, “k-Space Image Correlation Spectroscopy: A Method for Accurate Transport Measurements Independent of Fluorophore Photophysics,” *Biophys. J.*, vol. 91, no. 8, pp. 3061–3075, 2006.
- [50] P. W. Wiseman, P. Höddelius, N. O. Petersen, and K.-E. Magnusson, “Aggregation of PDGF-beta receptors in human skin fibroblasts: characterization by image correlation spectroscopy (ICS),” *FEBS Lett.*, vol. 401, no. 1, pp. 43–48, 1997.
- [51] C. M. Brown and N. O. Petersen, “An image correlation analysis of the distribution of clathrin associated adaptor protein (AP-2) at the plasma membrane,” vol. 281, pp. 271–281, 1998.
- [52] P. W. Wiseman and K. R. Wilson, “Two-photon image correlation spectroscopy and image cross-correlation spectroscopy,” vol. 200, no. October, pp. 14–25, 2000.
- [53] P. W. Wiseman *et al.*, “Spatial mapping of integrin interactions and dynamics during cell migration by Image Correlation Microscopy,” 2004.
- [54] S. Costantino, J. W. Comeau, D. L. Kolin, and P. W. Wiseman, “Accuracy and dynamic range of spatial image correlation and cross-correlation spectroscopy,” *Biophys. J.*, vol. 89, pp. 251–260, 2005.
- [55] G. W. Ashdown and D. M. Owen, “Spatio-temporal image correlation spectroscopy and super-resolution microscopy to quantify molecular dynamics in T cells,” *Methods*, vol. 140–141, pp. 112–118, 2018.
- [56] B. Hebert, S. Costantino, and P. W. Wiseman, “Spatiotemporal Image Correlation Spectroscopy (STICS) Theory , Verification , and Application to Protein Velocity Mapping in Living CHO Cells,” vol. 88, no. May, 2005.
- [57] M. Srivastava and N. O. P. U, “Diffusion of transferrin receptor clusters,” no. July, pp. 201–211, 1998.
- [58] D. L. Kolin and P. W. Wiseman, “Advances in Image Correlation Spectroscopy : Measuring Number Densities , Aggregation States , and Dynamics of Fluorescently labeled Macromolecules in Cells,” pp. 141–164, 2007.
- [59] C. Di Rienzo, E. Gratton, F. Beltram, and F. Cardarelli, “Fast spatiotemporal correlation spectroscopy to determine protein lateral diffusion laws in live cell

- membranes,” vol. 110, no. 30, pp. 12307–12312, 2013.
- [60] M. J. Rossow, J. M. Sasaki, M. A. Digman, and E. Gratton, “Raster image correlation spectroscopy in live cells,” *Nat. Protoc.*, vol. 5, no. 11, pp. 1761–1774, 2010.
- [61] S. Mikuni, J. Yamamoto, T. Horio, and M. Kinjo, “Negative Correlation between the Diffusion Coefficient and Transcriptional Activity of the Glucocorticoid Receptor,” *Int. J. Mol. Sci.*, vol. 18, no. 9, 2017.
- [62] M. A. Digman, C. M. Brown, P. Sengupta, P. W. Wiseman, A. R. Horwitz, and E. Gratton, “Measuring fast dynamics in solutions and cells with a laser scanning microscope,” *Biophys. J.*, vol. 89, no. 2, pp. 1317–1327, 2005.
- [63] J. R. Lakowicz, *Principles of Fluorescence Spectroscopy*, Third Edit. 2006.
- [64] E. Gielen *et al.*, “Diffusion of myelin oligodendrocyte glycoprotein in living OLN-93 cells investigated by raster-scanning image correlation spectroscopy (RICS),” *J. Fluoresc.*, vol. 18, no. 5, pp. 813–819, 2008.
- [65] C. M. Brown, R. B. Dalal, B. Hebert, M. A. Digman, A. R. Horwitz, and E. Gratton, “Raster image correlation spectroscopy (RICS) for measuring fast protein dynamics and concentrations with a commercial laser scanning confocal microscope,” *J. Microsc.*, vol. 229, no. 1, pp. 78–91, 2008.
- [66] E. Gielen *et al.*, “Measuring diffusion of lipid-like probes in artificial and natural membranes by raster image correlation spectroscopy (RICS): use of a commercial laser-scanning microscope with analog detection,” *Langmuir*, vol. 25, no. 9, pp. 5209–5218, 2009.
- [67] M. A. Digman, P. W. Wiseman, A. R. Horwitz, and E. Gratton, “Detecting protein complexes in living cells from laser scanning confocal image sequences by the cross correlation raster image spectroscopy method,” *Biophys. J.*, vol. 96, no. 2, pp. 707–716, 2009.
- [68] M. A. Digman and E. Gratton, “Analysis of diffusion and binding in cells using the RICS approach,” *Microsc. Res. Tech.*, vol. 72, no. 4, pp. 323–332, 2009.
- [69] S. Makaremi *et al.*, “The Topography of Silica Films Modulates Primary Macrophage Morphology and Function,” *Adv. Mater. Interfaces*, vol. 6, no. 21, p. 1900677, 2019.

- [70] M. A. Digman, R. Dalal, A. F. Horwitz, and E. Gratton, “Mapping the number of molecules and brightness in the laser scanning microscope.,” *Biophys. J.*, vol. 94, no. 6, pp. 2320–2332, 2008.
- [71] J. Brewer, M. Bloksgaard, J. Kubiak, J. A. Sørensen, and L. A. Bagatolli, “Spatially resolved two-color diffusion measurements in human skin applied to trans- dermal liposome penetration,” *J. Invest. Dermatol.*, vol. 133, pp. 1260–1268, 2013.
- [72] J. Hendrix, T. Dekens, W. Schrimpf, and D. C. Lamb, “Arbitrary-Region Raster Image Correlation Spectroscopy,” *Biophys. J.*, vol. 111, no. 8, pp. 1785–1796, 2016.
- [73] E. Sezgin *et al.*, “Measuring nanoscale diffusion dynamics in cellular membranes with super-resolution STED – FCS,” *Nat. Protoc.*, vol. 14, no. April, pp. 1054–1083, 2019.
- [74] R. Maraschini, O. Beutel, and A. Honigmann, “Circle scanning STED fluorescence correlation spectroscopy to quantify membrane dynamics and compartmentalization,” *Methods*, vol. 140–141, pp. 188–197, 2018.
- [75] P. N. Hedde *et al.*, “Stimulated emission depletion-based raster image correlation spectroscopy reveals biomolecular dynamics in live cells,” *Nat. Commun.*, vol. 4, p. 2093, 2013.
- [76] S. J. Sahl, S. W. Hell, and S. Jakobs, “Fluorescence nanoscopy in cell biology,” *Nat. Rev. Mol. Cell Biol.*, vol. 18, no. 11, pp. 685–701, 2017.
- [77] C. Eggeling *et al.*, “Direct observation of the nanoscale dynamics of membrane lipids in a living cell.,” *Nature*, vol. 457, no. 7233, pp. 1159–1162, 2009.
- [78] D. M. Andrade *et al.*, “Cortical actin networks induce spatio-temporal confinement of phospholipids in the plasma membrane--a minimally invasive investigation by STED-FCS.,” *Sci. Rep.*, vol. 5, p. 11454, 2015.
- [79] F. Schneider *et al.*, “Diffusion of lipids and GPI-anchored proteins in actin-free plasma membrane vesicles measured by STED-FCS,” *Mol. Biol. Cell*, vol. 28, no. 11, pp. 1507–1518, 2017.
- [80] G. I. Mashanov, D. Tacon, A. E. Knight, M. Peckham, and J. E. Molloy, “Visualizing single molecules inside living cells using total internal reflection fluorescence microscopy,” *Methods*, vol. 29, pp. 142–152, 2003.

- [81] A. L. Mattheyses, S. M. Simon, and J. Z. Rappoport, “Imaging with total internal reflection fluorescence microscopy for the cell biologist,” *J. Cell Sci.*, vol. 123, no. 21, pp. 3621–3628, 2010.
- [82] J. Irudayaraj, *Biomedical Nanosensors*. 2013.
- [83] N. Chenouard *et al.*, “Objective comparison of particle tracking methods,” *Nat. Methods*, vol. 11, pp. 281–289, 2014.
- [84] S. M. Anthony, L. Zhang, and S. Granick, “Methods to Track Single-Molecule Trajectories,” *Langmuir*, vol. 22, pp. 5266–5272, 2006.
- [85] D. Alcor, G. Gouzer, and A. Triller, “Single-particle tracking methods for the study of membrane receptors dynamics,” *Eur. J. Neurosci.*, vol. 30, pp. 987–97, 2009.
- [86] M. K. Cheezum, W. F. Walker, and W. H. Guilford, “Quantitative Comparison of Algorithms for Tracking Single Fluorescent Particles,” *Biophys. J.*, vol. 81, no. 4, pp. 2378–2388, 2001.
- [87] B. C. Carter, G. T. Shubeita, and S. P. Gross, “Tracking single particles: a user-friendly quantitative evaluation,” *Phys. Biol.*, vol. 2, pp. 60–72, 2005.
- [88] C. Manzo and M. F. Garcia-parajo, “A review of progress in single particle tracking : from methods to biophysical insights,” *Rep. Prog. Phys.*, vol. 78, p. 124601, 2015.
- [89] K. Shafiqe and M. Shah, “A noniterative greedy algorithm for multiframe point correspondence,” *IEEE Trans. Pattern Anal. Mach. Intell.*, vol. 27, no. 1, pp. 51–65, 2005.
- [90] L. Liang, H. Shen, P. De Camilli, and J. S. Duncan, “Tracking clathrin coated pits with a multiple hypothesis based method Med. Image Comput. Comput. Assist. Interv.,” *Med. Image Comput. Comput. Interv.*, vol. 13, pp. 315–322, 2010.
- [91] J. Verestóy, D. Csetverikov, and M. Nagy, “Digital particle image velocimetry: a challenge for feature based tracking Mach. Graph. Vis. 8,” *Mach. Graph. Vis.*, vol. 8, no. 4, pp. 553–69, 1999.
- [92] W. J. Godinez, M. Lampe, S. Wörz, B. Müller, R. Eils, and K. Rohr, “Deterministic and probabilistic approaches for tracking virus particles in time-lapse fluorescence microscopy image sequences,” *Med. Image Anal.*, vol. 13, pp.

- 325–42, 2009.
- [93] W. J. Godinez and K. Rohr, “Tracking multiple particles in fluorescence time-lapse microscopy images via probabilistic data association,” *IEEE Trans. Med. Imaging*, vol. 34, no. 2, pp. 415–32, 2015.
- [94] A. Jaiswal, W. J. Godinez, R. Eils, M. J. Lehmann, and K. Rohr, “Tracking Virus Particles in Fluorescence Microscopy Images Using Multi-Scale Detection and Multi-Frame Association,” *IEEE Trans. Image Process.*, vol. 24, no. 11, pp. 4122–36, 2015.
- [95] B. H. Lee and H. Y. Park, “HybTrack: A hybrid single particle tracking software using manual and automatic detection of dim signals,” *Sci. Rep.*, vol. 8, no. 1, p. 212, 2018.
- [96] X. Michalet, “Mean square displacement analysis of single-particle trajectories with localization error: Brownian motion in an isotropic medium,” *Phys Rev Stat Nonlin Soft Matter Phys*, vol. 82, no. 4, p. 041914, 2010.
- [97] V. Jaumouillé, Y. Farkash, K. Jaqaman, R. Das, C. A. Lowell, and S. Grinstein, “Actin cytoskeleton reorganization by Syk regulates Fc γ receptor responsiveness by increasing its lateral mobility and clustering,” *Dev. Cell*, vol. 29, no. 5, pp. 534–546, 2014.
- [98] J. Lin *et al.*, “TIRF imaging of Fc gamma receptor microclusters dynamics and signaling on macrophages during frustrated phagocytosis,” *BMC Immunol.*, vol. 17, no. 1, p. 5, 2016.
- [99] J. G. Bakker *et al.*, “Lateral mobility of individual integrin nanoclusters orchestrates the onset for leukocyte adhesion,” *PNAS*, vol. 109, no. 13, pp. 4869–4874, 2012.
- [100] C. Eich *et al.*, “Changes in membrane sphingolipid composition modulate dynamics and adhesion of integrin nanoclusters,” *Sci. Rep.*, vol. 6, p. 20693, 2016.
- [101] S. J. Sahl, M. Leutenegger, M. Hilbert, S. W. Hell, and C. Eggeling, “Fast molecular tracking maps nanoscale dynamics of plasma membrane lipids,” *Proc Natl Acad Sci USA*, vol. 107, no. 15, pp. 6829–6834, 2010.
- [102] S. A. Freeman *et al.*, “Transmembrane pickets connect cyto-and pericellular-skeletons forming barriers to receptor engagement,” *Cell*, vol. 172, no. 1–2, p. 305–317.e10, 2018.

- [103] S. A. Freeman *et al.*, “Integrins Form an Expanding Diffusional Barrier that Coordinates Phagocytosis,” *Cell*, vol. 164, no. 0, pp. 128–140, 2016.
- [104] B. Treanor *et al.*, “The Membrane Skeleton Controls Diffusion Dynamics and Signaling through the B Cell Receptor,” *Immunity*, vol. 32, no. 2, pp. 187–199, 2010.
- [105] D. F. Kucik, M. L. Dustin, J. M. Miller, and E. J. Brown, “Adhesion-activating phorbol ester increases the mobility of leukocyte integrin LFA-1 in cultured lymphocytes,” *J. Clin. Invest.*, vol. 97, no. 9, pp. 2139–2144, 1996.
- [106] T. Jin and J. Li, “Dynamitin controls 2 integrin avidity by modulating cytoskeletal constraint on integrin molecules,” *J. Biol. Chem.*, vol. 277, no. 36, pp. 32963–32969, 2002.
- [107] Y. Ito, K. Sakata-Sogawa, and M. Tokunaga, “A Facile Preparation of Glass-supported Lipid Bilayers for Analyzing Molecular Dynamics,” *Anal. Sci.*, vol. 30, no. 12, pp. 1103–1106, 2014.
- [108] T. J. Deerinck, “The Application of Fluorescent Quantum Dots to Confocal, Multiphoton, and Electron Microscopic Imaging,” *Toxicol Pathol*, vol. 36, no. 1, pp. 112–116, 2008.
- [109] Y. Ito, K. Sakata-Sogawa, and M. Tokunaga, “Multi-color single-molecule tracking and subtrajectory analysis for quantification of spatiotemporal dynamics and kinetics upon T cell activation,” *Sci. Rep.*, vol. 7, no. 1, p. 6994, 2017.
- [110] S. T. Low-Nam *et al.*, “ErbB1 dimerization is promoted by domain co-confinement and stabilized by ligand-binding,” *Nat Struct Mol Biol*, vol. 18, no. 11, pp. 1244–1249, 2011.
- [111] J. A. Torreno-Pina, B. M. Castro, C. Manzo, S. I. Buschow, A. Cambi, and M. F. Garcia-Parajo, “Enhanced receptor–clathrin interactions induced by N-glycan-mediated membrane micropatterning,” *Proc. Natl. Acad. Sci. USA*, vol. 111, no. 30, pp. 11037–11042, 2014.
- [112] C. Espenel *et al.*, “Single-molecule analysis of CD9 dynamics and partitioning reveals multiple modes of interaction in the tetraspanin web,” *J. Cell Biol.*, vol. 182, no. 4, pp. 765–776, 2008.
- [113] M. Tokunaga, N. Imamoto, and K. Sakata-Sogawa, “Highly inclined thin

- illumination enables clear single-molecule imaging in cells,” *Nat. Methods*, vol. 5, pp. 159–61, 2008.
- [114] M. P. Clausen and B. C. Lagerholm, “The Probe Rules in Single Particle Tracking,” *Curr. Protein Pept. Sci.*, vol. 12, pp. 699–713, 2011.
- [115] L. Guo, J. Y. Har, J. Sankaran, Y. Hong, B. Kannan, and T. Wohland, “Molecular Diffusion Measurement in Lipid Bilayers over Wide Concentration Ranges: A Comparative Study,” *Chem. Phys. Phys. Chem.*, vol. 9, no. 5, pp. 721–728, 2008.
- [116] N. Loren *et al.*, “Fluorescence recovery after photobleaching in material and life sciences: putting theory into practice,” *Q. Rev. Biophys.*, vol. 48, no. 3, pp. 323–387, 2015.
- [117] S. Semrau and T. Schmidt, “Particle Image Correlation Spectroscopy (PICS): Retrieving Nanometer-Scale Correlations from High-Density Single-Molecule Position Data,” vol. 92, no. January, 2007.
- [118] A. Dupont, K. Stirnagel, D. Lindemann, and D. C. Lamb, “Tracking Image Correlation : Combining Single-Particle Tracking and Image Correlation,” *Biophysj*, vol. 104, no. 11, pp. 2373–2382, 2013.
- [119] M. Longfils *et al.*, “Single particle raster image analysis of diffusion,” *J. Microsc.*, vol. 266, no. 1, pp. 3–14, 2017.
- [120] M. I. E. Harwardt, M. S. Dietz, M. Heilemann, and T. Wohland, “SPT and Imaging FCS Provide Complementary Information on the Dynamics of Plasma Membrane Molecules,” *Biophys. J.*, vol. 114, no. 10, pp. 2432–2443, 2018.
- [121] K. B. Im, U. Schmidt, M. S. Kang, J. Y. Lee, F. Bestvater, and M. Wachsmuth, “Diffusion and binding analyzed with combined point FRAP and FCS,” *Cytom. A*, vol. 83, no. 9, pp. 876–889, 2013.
- [122] K. C. Mudumbi, E. C. Schirmer, and W. Yang, “Single-point single-molecule FRAP distinguishes inner and outer nuclear membrane protein distribution,” *Nat. Commun.*, vol. 7, p. 12562, 2016.
- [123] S. Chiantia, N. Kahya, and P. Schwille, “Raft Domain Reorganization Driven by Short- and Long-Chain Ceramide: A Combined AFM and FCS Study,” *Langmuir*, vol. 23, no. 14, pp. 7659–7665, 2007.

- [124] B. Plochberger *et al.*, “HDL particles incorporate into lipid bilayers – a combined AFM and single molecule fluorescence microscopy study,” *Sci. Rep.*, vol. 7, p. 15886, 2017.
- [125] C. Manzo, T. S. van Zanten, and M. F. Garcia-Parajo, “Nanoscale Fluorescence Correlation Spectroscopy on Intact Living Cell Membranes with NSOM Probes,” *Biophys. J.*, vol. 100, pp. L8–L10, 2011.
- [126] Y. Wu and H. Shroff, “Faster, sharper, and deeper: structured illumination microscopy for biological imaging,” *Nat Methods*, vol. 15, pp. 1011–1019, 2018.
- [127] M. G. Gustafsson, “Surpassing the lateral resolution limit by a factor of two using structured illumination microscopy,” *J. Microsc.*, vol. 198, pp. 82–87, 2000.
- [128] P. Winkler *et al.*, “Optical Antenna-Based Fluorescence Correlation Spectroscopy to Probe the Nanoscale Dynamics of Biological Membranes,” *J. Phys. Chem. Lett.*, vol. 9, pp. 110–119, 2018.
- [129] H. G. Samiee, K. T., Moran-Mirabal, J. M., Cheung, Y. K., & Craighead, “Zero mode waveguides for single-molecule spectroscopy on lipid membranes,” *Biophys. Journal.*, vol. 90, pp. 3288–3299, 2006.
- [130] J. Wenger, H. Rigneault, J. Dintinger, D. Marguet, and P. F. Lenne, “Single-Fluorophore Diffusion in a Lipid Membrane over a Subwavelength Aperture,” *J. Biol. Phys.*, vol. 32, 2006.
- [131] C. I. Richards *et al.*, “Live-Cell Imaging of Single Receptor Composition Using Zero-Mode Waveguide Nanostructures,” *Nano Lett.*, vol. 12, p. 3690–3694., 2012.
- [132] J. M. Moran-Mirabal, A. J. Torres, K. T. Samiee, B. A. Baird, and H. G. Craighead, “Cell investigation of nanostructures: zero-mode waveguides for plasma membrane studies with single molecule resolution,” *Nanotechnology*, vol. 18, no. 19, 2007.
- [133] M. Rose, N. Hirmiz, J. M. Moran-Mirabal, and C. Fradin, “Lipid diffusion in supported lipid bilayers: A comparison between line-scanning fluorescence correlation spectroscopy and single-particle tracking,” *Membranes (Basel)*, vol. 5, no. 4, pp. 702–721, 2015.
- [134] P. Moens, “Fluorescence correlation spectroscopy, raster image correlation spectroscopy, and number and brightness on a commercial confocal laser scanning

- microscope with,” *Microsc. Res. Tech.*, vol. c, no. 4, pp. 377–388, 2011.
- [135] S. Nie, D. T. Chiu, and R. N. Zare, “Probing individual molecules with confocal fluorescence microscopy,” *Science*, vol. 266, pp. 1018–1021, 1994.
- [136] A. Kapanidis, T. Laurence, N. Lee, E. Margeat, X. Kong, and S. Weiss, “Alternating-laser excitation of single molecules,” *Acc. Chem. Res.*, vol. 38, pp. 523–33, 2005.
- [137] M. Howarth *et al.*, “Monovalent, reduced-size quantum dots for imaging receptors on living cells,” *Nat Methods*, vol. 5, pp. 397–9, 2008.
- [138] L. Abraham *et al.*, “Limitations of Qdot labelling compared to directly-conjugated probes for single particle tracking of B cell receptor mobility,” *Sci. Rep.*, vol. 7, p. 11379, 2017.
- [139] M. F. Engelke *et al.*, “Engineered kinesin motor proteins amenable to small-molecule inhibition,” *Nat. Commun.*, vol. 7, p. 11159, 2016.
- [140] S. A. Freeman *et al.*, “Toll-like receptor ligands sensitize B-cell receptor signalling by reducing actin-dependent spatial confinement of the receptor,” *Nat. Commun.*, vol. 6, no. May 2014, p. 6168, 2015.
- [141] K. Jaqaman *et al.*, “Cytoskeletal control of CD36 diffusion promotes its receptor and signaling function,” *Cell*, vol. 146, p. 593–606., 2011.
- [142] L. Kleine Borgmann, J. Ries, H. Ewers, M. Ulbrich, and P. Graumann, “The bacterial SMC complex displays two distinct modes of interaction with the chromosome,” *Cell Rep.*, vol. 3, no. 5, pp. 1483–92, 2013.
- [143] P. Zawadzki *et al.*, “The Localization and Action of Topoisomerase IV in Escherichia coli Chromosome Segregation Is Coordinated by the SMC Complex, MukBEF,” *Cell Rep.*, vol. 13, no. 11, pp. 2587–2596, 2015.
- [144] M. Stracy, C. Lesterlin, F. Garza de Leon, S. Uphoff, P. Zawadzki, and A. Kapanidis, “Live-cell superresolution microscopy reveals the organization of RNA polymerase in the bacterial nucleoid,” *Proc Natl Acad Sci USA*, vol. 112, no.32, 2015
- [145] A. Sanamrad, F. Persson, E. Lundius, D. Fange, A. Gynna, and J. Elf, “Single-particle tracking reveals that free ribosomal subunits are not excluded from the Escherichia coli nucleoid,” *Proc Natl Acad Sci USA*, vol. 111, no. 31, pp. 11413–8, 2014.

- [146] K. Schenk *et al.*, “Rapid turnover of DnaA at replication origin regions contributes to initiation control of DNA replication.,” *PLoS Genet*, vol. 13, no. 2, p. e1006561, 2017.
- [147] Y. Liao, J. Schroeder, B. Gao, L. Simmons, and J. Biteen, “Single-molecule motions and interactions in live cells reveal target search dynamics in mismatch repair,” *Proc Natl Acad Sci USA*, vol. 112, pp. 6898–6906, 2015.
- [148] C. Mullineaux, “Localization and mobility of bacterial proteins by confocal microscopy and fluorescence recovery after photobleaching,” *Methods Mol. Biol.*, vol. 390, pp. 3–15, 2007.
- [149] L. Zhang, Y. Chen, W. Chen, and C. Zhang, “Existence of periplasmic barriers preventing green fluorescent protein diffusion from cell to cell in the cyanobacterium *Anabaena* sp. strain PCC 7120,” *Mol. Microbiol.*, vol. 70, no. 4, pp. 814–823, 2008.
- [150] D. Chow, L. Guo, F. Gai, and M. Goulian, “Fluorescence correlation spectroscopy measurements of the membrane protein TetA in *Escherichia coli* suggest rapid diffusion at short length scales,” *PLoS One*, vol. 7, no. 10, p. e48600, 2012.
- [151] S. M. van den Wildenberg, Y. J. Bollen, and E. J. Peterman, “How to quantify protein diffusion in the bacterial membrane,” *Biopolymers*, vol. 95, no. 5, pp. 312–321, 2011.
- [152] X. Li, J. Xing, Z. Qiu, Q. He, and J. Lin, “Quantification of Membrane Protein Dynamics and Interactions in Plant Cells by Fluorescence Correlation Spectroscopy.,” *Mol. Plant*, vol. 9, no. 9, pp. 1229–1239, 2016.
- [153] M. Laňková *et al.*, “Determination of Dynamics of Plant Plasma Membrane Proteins with Fluorescence Recovery and Raster Image Correlation Spectroscopy,” *Microsc. Microanal.*, vol. 22, no. 2, pp. 290–299, 2016.
- [154] A. Tauber, “Metchnikoff and the phagocytosis theory.,” *Nat. Rev. Mol. Cell Biol.*, vol. 4, no. 11, pp. 897–901, 2003.
- [155] S. Epelman, K. J. Lavine, and G. J. Randolph, “Origin and Functions of Tissue Macrophages,” *Immunity*, vol. 41, no. 1, pp. 21–35, 2014.
- [156] G. Arango Duque and A. Descoteaux, “Macrophage cytokines: involvement in immunity and infectious diseases,” *Front. Immunol.*, vol. 5, p. 491, 2014.

- [157] C. D. Mills, K. Kincaid, J. M. Alt, M. J. Heilman, and A. M. Hill, “M-1/M-2 Macrophages and the Th1/Th2 Paradigm,” *J Immunol*, vol. 164, no. 12, pp. 6166–6173, 2000.
- [158] F. Y. Mcwhorter, T. Wang, P. Nguyen, T. Chung, and W. F. Liu, “Modulation of macrophage phenotype by cell shape.,” *Proc. Natl. Acad. Sci. U. S. A.*, vol. 110, no. 43, pp. 17253–8, 2013.
- [159] H. M. Rostam *et al.*, “The impact of surface chemistry modification on macrophage polarisation,” *Immunobiology*, vol. 221, no. 11, pp. 1237–1246, 2016.
- [160] S. A. Freeman and S. Grinstein, “Phagocytosis: receptors, signal integration, and the cytoskeleton,” *Immunol. Rev.*, vol. 262, pp. 193–215, 2014.
- [161] R. S. Flannagan, V. Jaumouillé, and S. Grinstein, “The cell biology of phagocytosis,” *Annu Rev Pathol*, vol. 7, pp. 61–98, 2012.
- [162] R. Botelho and S. Grinstein, “Phagocytosis,” *Curr Biol*, vol. 21, no. 14, pp. 533–538, 2011.
- [163] M. Rabinovitch, “Professional and non-professional phagocytes: an introduction,” *Trends Cell Biol.*, vol. 5, no. 3, pp. 85–87, 1995.
- [164] S. Gordon, “Phagocytosis: An Immunobiologic Process.,” *Immunity*, vol. 44, no. 3, pp. 463–475, 2016.
- [165] J. Monks *et al.*, “Epithelial cells as phagocytes: apoptotic epithelial cells are engulfed by mammary alveolar epithelial cells and repress inflammatory mediator release,” *Cell Death Differ.*, vol. 12, pp. 107–114, 2005.
- [166] T. Ichimura, E. Asseldonk, B. Humphreys, L. Gunaratnam, J. Duffield, and J. Bonventre, “Kidney injury molecule-1 is a phosphatidylserine receptor that confers a phagocytic phenotype on epithelial cells.,” *J. Clin. Invest.*, vol. 118, p. 1657–1668., 2008.
- [167] P. R. Taylor, L. Martinez-Pomares, M. Stacey, H. H. Lin, G. D. Brown, and S. Gordon, “Macrophage Receptors and Immune Recognition,” *Annu. Rev. Immunol*, vol. 23, pp. 901–44, 2005.
- [168] A. Aderem and R. J. Ulevitch, “the Innate Immune Response,” *Nature*, vol. 406, no. August, pp. 782–787, 2000.
- [169] A. Aderem and D. M. Underhill, “Mechanism of Phagocytosis in Macrophages,”

- Annu. Rev. Immunol.*, vol. 17, no. 1, pp. 593–623, 1999.
- [170] D. M. Underhill and A. Ozinsky, “Toll-like receptors: Key mediators of microbe detection,” *Curr. Opin. Immunol.*, vol. 14, no. 1, pp. 103–110, 2002.
- [171] K. Anderson, L. Bokla, and C. Nüsslein-Volhard, “Establishment of dorsal-ventral polarity in the *Drosophila* embryo: the induction of polarity by the Toll gene product.,” *Cell*, vol. 42, no. 3, pp. 791–798, 1985.
- [172] M. S. Jin and J. O. Lee, “Structures of the Toll-like Receptor Family and Its Ligand Complexes,” *Immunity*, vol. 29, no. 2, pp. 182–191, 2008.
- [173] S. Akira and S. Uematsu, “Toll-like receptors (TLRs) and Their Ligands,” *Toll-Like Recept. Innate Immun.*, pp. 6–8, 2007.
- [174] A. L. Blasius and B. Beutler, “Intracellular toll-like receptors,” *Immunity*, vol. 32, no. 3, pp. 305–15, 2010.
- [175] G. Gerold, K. Abu Ajaj, M. Bienert, H.-J. Laws, A. Zychlinsky, and J. L. de Diego, “A Toll-like receptor 2-integrin beta3 complex senses bacterial lipopeptides via vitronectin.,” *Nat. Immunol.*, vol. 9, no. 7, pp. 761–8, 2008.
- [176] S. Akira and K. Takeda, “Toll-like receptor signalling,” *Nat. Rev. Immunol.*, vol. 4, no. 7, pp. 499–511, 2004.
- [177] J. van Bergenhenegouwen *et al.*, “TLR2 & Co: a critical analysis of the complex interactions between TLR2 and coreceptors.,” *J Leukoc Biol*, vol. 94, no. 5, pp. 885–902, 2013.
- [178] J. Pugin, I. Heumann, A. Tomasz, and E. Al, “CD14 is a pattern recognition receptor,” *Immunity*, vol. 1, pp. 509–516, 1994.
- [179] D. Heumann *et al.*, “Control of lipopolysaccharide (LPS) binding and LPS-induced tumor necrosis factor secretion in human peripheral blood monocytes,” *J Immunol*, vol. 148, no. 11, pp. 3505–3512, 1992.
- [180] M. Jin *et al.*, “Crystal structure of the TLR1-TLR2 heterodimer induced by binding of a tri-acylated lipopeptide,” *Cell*, vol. 130, no. 6, pp. 1071–1082, 2007.
- [181] Z. Wu, Z. Zhang, Z. Lei, and P. Lei, “CD14: Biology and role in the pathogenesis of disease,” *Cytokine Growth Factor Rev.*, vol. 48, pp. 24–31, 2019.
- [182] I. Zanoni *et al.*, “CD14 controls the LPS-induced endocytosis of toll-like receptor 4,” *Cell*, vol. 147, no. 4, pp. 868–880, 2011.

Chapter 2

Lateral Diffusion of CD14 and TLR2

The aim of the study presented in this chapter was to obtain accurate diffusion coefficients of CD14 and TLR2 on the apical and basal membranes of macrophages using two common fluorescence-based methods: raster image correlation spectroscopy (RICS) and single-particle tracking (SPT). Our findings highlight the importance of selecting the appropriate membrane when measuring receptor diffusion in live cells. While RICS enables the study of the diffusion in different regions of membranes and cross sections through the cell body, SPT is suitable for tracking the motions of individual membrane-inserted proteins only in the basal membrane.

The content of this chapter is part of a manuscript prepared for submission to the journal *Communications Biology*.

2.1 Introduction

The plasma membrane is a highly fluid and dynamic environment, where lipids and proteins laterally diffuse within the lipid bilayer –a feature that enables key cellular processes involving the transport of biological species [1]. Several powerful fluorescence-based methods have been used to study the dynamics of membrane components, such as the diffusion and association of immunoreceptors [2–5]. These techniques are based on either ensemble measurements, where the diffusion coefficient is obtained from the average motion of groups of molecules, or single particle tracking where the mobility of individual particles is analyzed. Ensemble techniques include fluorescence recovery after photobleaching (FRAP), which irreversibly bleaches a small area of the fluorescently labeled membrane with a brief intense illumination pulse. The diffusion coefficient is then determined by monitoring the fluorescence recovery that results as bleached molecules migrate out of the illuminated area and are replaced by fluorescent ones [6,7]. A second ensemble method is fluorescence correlation spectroscopy (FCS) [8,9] which determines the diffusion by monitoring the fluctuations of the fluorescence signal in a fixed observation volume. FCS is used to measure fast (micro- to millisecond timescale) dynamics, binding and association kinetics, in a single fixed spot on the membrane [4].

Raster image correlation spectroscopy (RICS) [10,11] is in principle an extended version of FCS, with the addition of a spatial component using confocal laser-scanning microscope (CLSM), which uses raster scan to capture the fluctuations in the intensity caused by the movement of fluorescent molecules. By measuring the intensity at one pixel for a very brief period of time followed by measuring the intensity of adjacent pixels immediately after, the intensities of pixels in each frame can be correlated pair-wise to identify characteristic decay times corresponding to dynamic processes, such as the diffusion of fluorescent particles through the detection volume [12]. The spatial correlation depends on the rate of diffusion, the pixel dwell time, and the size of pixels. Since RICS is typically implemented using CLSM, the reduction of out-of-focus signal enables measurements that are confined to a narrow plane in the cell. Additionally, the ability of the RICS analysis routine to separate the slow and immobile fractions of particles makes it possible to monitor the diffusion of heterogeneous particles. Thus, this technique is frequently used to measure the diffusion coefficient of proteins in live cells

[13–16].

Single particle tracking (SPT) is commonly used to measure the diffusion of membrane components in live cells [2,17,18]. SPT provides information on the trajectories of individual particles with a spatial resolution < 20 nm. SPT is typically performed on images acquired with a total internal reflection fluorescence (TIRF) microscope, where the acquisition of the intensities of all the pixels in each frame is done simultaneously and isolated particles are captured for relatively long periods of time (seconds to minutes), with frame rates of up to 40 kHz. The images are then analyzed to precisely locate each fluorescent particle within the image and the trajectories are built by linking the positions of particles in consecutive frames.

The aim of the present study was to measure and compare the lateral diffusion of two key receptors involved in the recognition of pathogenic stimuli on the plasma membrane of macrophages, using two different fluorescence-based techniques for comparison: RICS and SPT. Transmembrane toll-like receptor 2 (TLR2) and glycosylphosphatidylinositol (GPI)-linked cluster of differentiation 14 (CD14) are two receptors expressed by macrophages, which are key in binding bacterial products and initiating inflammatory responses. TLRs are type I glycoproteins composed of extracellular, transmembrane, and intracellular signaling domains [19]. TLR2 binds the anchor motif of lipoproteins found on the surface of bacteria and responds to lipid-containing pathogen associated molecular patterns (PAMPs) such as lipoteichoic acid (LTA) from Gram-positive bacteria [20]. CD14, on the other hand, is a pattern-recognition receptor (PRR) that binds lipopolysaccharide (LPS) in Gram-negative and LTA in Gram-positive bacterial membranes [21].

The spatial distribution of immunoreceptors and their lateral mobility in the plasma membrane impact receptor-mediated signaling [22]. Lateral clustering of receptors is essential for their activation since an increased local density of receptors enhances the efficiency of signal transduction whenever cooperation between multiple molecular players is required [22]. For example, TLR2 forms TLR-ligand complexes and initiates signaling through dimerization with other TLRs [19]. CD14 serves as a coreceptor of many TLRs, including TLR2 [23], and activates the intracellular signaling cascade and the innate immune response with the help of transmembrane receptors. Extracting the

rates of diffusion of these and other related immunoreceptors can be invaluable in understanding their signaling mechanisms in response to bacterial products.

To our knowledge, this is the first study that measures the lateral diffusion of TLR2 and CD14 in the apical and basal plasma membranes of macrophages and directly compares the diffusion measurements with the aid of two fluorescence-based methods, SPT and RICS. Studying the dynamics of these receptors using two different techniques provides complementary insights into their diffusion behavior as well as a true comparison of the precision, advantages, and disadvantages of these techniques.

2.2 Experimental Section

2.2.1 Cell Culture

Macrophage cell line RAW 264.7 [24] from American Type Culture Collection (ATCC) was cultured using RPMI-1640 supplemented with 10% fetal bovine serum (FBS), 1% L-glutamine, and 1% penicillin/streptomycin. Twenty four hours before imaging, the cells were incubated with Trypsin/EDTA (Gibco™) for 5 min, then gently lifted using a cell lifter and plated at a density of 100,000 per Glass Bottom dish (35 mm dish, 20 mm Microwell, No. 1.5 coverglass, 0.16-0.19 mm thickness, MatTek, Ashland, MA). Fluorescent microspheres (FluoSpheres®, carboxylate-modified, 0.17 μm, excitation: 505 nm; emission: 515 nm, Life Technologies, Invitrogen Molecular Probes®, Eugene, OR) were mixed in 50% isopropanol in water and added to the imaging dishes at a density that guaranteed 1–3 microspheres per field of view to serve as the fiducial markers for drift correction. Prior to seeding the cells, the microspheres were fused to the coverglass by heating the dish containing microspheres in solution at 65°C for 10 min.

2.2.2 Fluorescence Staining

All imaging was performed in RPMI-1640 medium without phenol red (Life Technologies- Gibco™). TLR2 and CD14 were visualized in separate experiments using mouse anti-TLR2/CD282 antibody labeled with Alexa Fluor 647 (0.2 mg/mL, BD Biosciences) and mouse anti-CD14 antibody labeled with APC (excitation: 633-647 nm, emission: 660 nm, 0.2 mg/mL, eBioscience), at a 1:1000 dilution in imaging media. Antibody staining was performed at 4°C for 1 hr to prevent receptor internalization, after

which the samples were washed with PBS 3× and the media was replaced with RPMI including 5 mM ascorbic acid to minimize photobleaching during imaging.

2.2.3 Single Particle Tracking (SPT)

Total Internal Reflection Fluorescence Microscopy (TIRF)

SPT imaging was performed on an objective-based TIRF setup built on a Leica inverted microscope stand (Leica DMI6000 B, Germany) and outfitted with an oil-immersion objective of 100×/1.47NA (HCX PL APO, Leica Germany CORR TIRF). The excitation light source was a LMM5 solid state laser launch (Spectral Applied Research Inc., Richmond Hill, ON, Canada) with 488 and 647 nm emission lines. Single particle images were captured by an Andor iXon Ultra EMCCD camera (Andor Technology Ltd., Belfast, U.K). Time-lapse movies of 300 frames were acquired using Micro-Manager software (MMSStudio Version 1.4.22) at a frame rate of ~16.7 fps (acquisition time of $\tau_a = 60$ ms per frame), with a field of view of 512×512 pixels and pixel sizes of $97 \text{ nm} \times 97 \text{ nm}$. Live cell imaging was performed at 37°C using an objective heater (FCS2, Biopetechs Inc., Butler, PA).

Particle Detection & Tracking

The series of frames captured for each cell were analyzed using an in-house program written in Python, under the use of the packages numpy, scipy, pandas, tkinter, and scikit-images, using a single-particle detection and tracking algorithm [25–27]. Each raw image was first processed with a Gaussian and a top-hat filter. The local maxima, *i.e.*, approximate particle positions were determined and a threshold was applied to generate a binary map of the estimated positions for each particle, which were used as starting values in the particle fitting algorithm. All particles within the raw images were then fitted to a 2D Gaussian model function via least squares optimization. The width and eccentricity of the detections were analyzed from the fitted functions and were excluded if they exceeded predefined thresholds (4 standard deviations of the background). The fitting algorithm determined the particle (fluorescent antibodies) positions with an accuracy of ~20 nm [26]. Individual positions in consecutive frames were then linked to generate tracks for each particle using an appropriate search radius determined from

simulations (Supporting Information for Chapter 2 Figures S2.1-S2.5). Every link was associated with a cost, representing the travelled distance of the particle in a frame interval. The tracks of individual particles were generated by minimizing the global cost for all links.

To obtain the number of immobile particles, the step-size distribution of the shortest lag time was used from which the standard deviation was extracted. A threshold of three standard deviations (3σ) was used to determine the immobile fraction (stationary particle if end-to-end tracks $<$ threshold).

Measuring Diffusion Coefficient

Diffusion coefficients were calculated using three different methods from the generated tracks. We first used each individual track to calculate the mean-squared displacement (MSD) and the diffusion coefficient D from:

$$\langle (\Delta r)^2 \rangle (\tau) = 4D\tau. \quad (2.1)$$

In the second approach, all tracks generated within a single cell were concatenated to create a master trajectory and the combined-MSD (c-MSD) was used to determine D from Equation (2.1).

In the final approach, the distribution of displacements was analyzed using Equation (2.2) for all tracks. For a simple diffusion process, the probability density function for a particle in one dimension is Gaussian and its widths is time dependent according to:

$$P(\Delta x, \tau) = \frac{1}{\sqrt{4\pi D\tau}} \exp\left[-\frac{\Delta x^2}{4D\tau}\right], \quad (2.2)$$

where Δx is the displacement after a lag time τ . The diffusion coefficients were obtained for different lag times, by fitting to the distributions of displacements.

2.2.4 Raster Image Correlation Spectroscopy (RICS)

Confocal Imaging

Raster-scan images were collected using confocal laser-scanning microscopy (CLSM, Olympus FluoView FV1000, Central Valley, PA) on an inverted microscope stand outfitted with a $60\times/1.20\text{NA}$ UPLSAPO water-immersion objective. Excitation was from 647-nm laser line attenuated to 0.5-1.0% nominal power. For scanning the basal

membrane, the plane of focus was set as close as possible to the bottom membrane plane, where the cell was making contact with glass. The apical membrane was found by focusing on the highest observable plane through the cell.

For raster image correlation spectroscopy (RICS), 256×256 pixel images were collected using FluoView imaging software (Olympus FluoView 1.7a) at 16.4x zoom, corresponding to a pixel size of 50 nm. For raster-scanning live cells, the pixel dwell time was set to 40 $\mu\text{s}/\text{pixel}$ (line time 11.264 ms). Stacks of 50 images were captured with no delay between frames. Imaging of live cells was performed at 37°C using a stage-top incubator (Tokai Hit, Shizuoka, Japan).

RICS Diffusion Measurements

Diffusion data was obtained using the SimFCS software [12] (The Laboratory for Fluorescence Dynamics, University of California, Irvine; available at www.lfd.uci.edu). Regions of interest (ROI) were selected with sizes of 64×64 pixels ($3.2 \times 3.2 \mu\text{m}^2$) within each cell. The diffusion coefficient was measured using the known parameters of pixel dwell time, line time, size of each pixel, and the beam waist. A focal volume waist (ω_0) of 0.24 μm was measured according to the previously established methods [12]. For each stack of images, the RICS function was calculated as the average of all images of the stack. Data was obtained from 15 cells for each receptor, using a minimum of three separate ROIs measured in each of the apical and basal membranes.

Principles of RICS

The principles of RICS are explained in detail in the seminal papers by Gratton and Digman [10,11]. Here we briefly reiterate the autocorrelation functions for reference purposes. The scanning function that relates time with space, *i.e.* the spatio-temporal correlation is defined as:

$$\tau(\xi, \psi) = \tau_p \xi + \tau_l \psi, \quad (2.3)$$

where τ_p and τ_l denote pixel dwell time and line scan time, respectively. ξ and ψ are the spatial displacements (in pixels) in the horizontal and vertical direction of scan in the raster image, respectively. The normalized spatial correlation function of the pixel fluorescence intensity fluctuations is defined as:

$$G_s(\xi, \psi) = \frac{\langle \delta I(x, y) \delta I(x + \xi, y + \psi) \rangle_{x, y}}{\langle I(x, y) \rangle_{x, y}^2} = G(\xi, \psi) S(\xi, \psi), \quad (2.4)$$

where $I(x, y)$ is the detected fluorescence intensity at each pixel and $\delta I(x, y) = I(x, y) - \langle I(x, y) \rangle_{x, y}$ are the fluorescence intensity fluctuations around the mean intensity. The autocorrelation function for 3D diffusion is:

$$G(\xi, \psi) = \frac{\gamma}{N} \left(1 + \frac{4D(\tau_p \xi + \tau_l \psi)}{\omega_0^2} \right)^{-1} \left(1 + \frac{4D(\tau_p \xi + \tau_l \psi)}{\omega_z^2} \right)^{-1/2}, \quad (2.5)$$

where D is the diffusion coefficient, N is the average number of molecules in the observation volume, and ω_0 and ω_z are the lateral and axial waists of the laser beam at the point of focus. The γ factor accounts for the non-uniform illumination of the excitation volume and is equal to 0.3535 for 3D and 0.5 for 2D Gaussian point spread functions (PSF) [28]. For 2D diffusion, the last factor in equation (2.5) is omitted.

$G(\xi, \psi)$ is the autocorrelation function that results from molecular diffusion only. Since the PSF spans over several pixels in the imaging plane, the correlation for the contribution of the scan itself should be also taken into account. For square pixels with dimension $\delta r \times \delta r$ the correlation for the scan is given by:

$$S(\xi, \psi) = \exp \left(\frac{\left[\left(\frac{\xi \delta r}{\omega_0} \right)^2 + \left(\frac{\psi \delta r}{\omega_0} \right)^2 \right]}{1 + \frac{4D(\tau_p \xi + \tau_l \psi)}{\omega_0^2}} \right). \quad (2.6)$$

Statistical Analysis

Statistical analysis and plotting was performed using SPSS software (IBM SPSS Statistics 21) and Prism 7.0a (GraphPad Software Inc.), respectively. Differences were considered statistically significant at P values of < 0.05 .

2.3 Results

2.3.1 Single Particle Tracking

To measure the diffusion of membrane receptors using single particle tracking, time-lapse movies were acquired using total internal reflection fluorescence microscopy. Figure

2.1A shows the tracks obtained from a series of 300 frames capturing TLR2 diffusion on the basal membrane of a RAW 264.7 cell (full movie included in Supporting Information). SPT (*cf.* Experimental Section 2.2.3) was used to generate the tracks for each individual particle. First, the diffusion coefficient of each track was obtained from the mean-squared displacement data and the fit to Equation 2.1 (tracks ≥ 10 steps were analyzed). The mean diffusion coefficients calculated from this analysis for TLR2 and CD14 in 15 RAW 264.7 cells were $D_{\text{TLR2-Basal}} = 0.08 \pm 0.02 \mu\text{m}^2/\text{s}$ and $D_{\text{CD14-Basal}} = 0.13 \pm 0.02 \mu\text{m}^2/\text{s}$, respectively. A comparison of the diffusion coefficients versus track length did not reveal any correlation (Supporting Information for Chapter 2 Figure S2.6). This verified that the diffusion measurements were not skewed by the number of steps recorded for each particle. For a global diffusion analysis, we then created a combined track by concatenating the individual tracks randomly (Figure 2.1B), which did not reveal any overall drift or directed motion. The diffusion coefficient was then calculated by fitting Equation 2.1 to the MSD data for lag time $\tau \leq 0.5$ s (the mean single-track length for the data set), as shown in Figure 2.1C. The average diffusion coefficients calculated using this approach were $D_{\text{TLR2-Basal}} = 0.07 \pm 0.02 \mu\text{m}^2/\text{s}$ and $D_{\text{CD14-Basal}} = 0.11 \pm 0.02 \mu\text{m}^2/\text{s}$ for TLR2 and CD14, respectively. As shown in Figure 2.2, both MSD measurements (*i.e.*, individual and combined tracks) reveal that the mean diffusion coefficient of CD14 is higher than TLR2 in the basal membrane. Similarly, fitting Equation 2.2 to the step-size distribution data (Figure 2.1D) yielded average diffusion coefficients of $D_{\text{TLR2-Basal}} = 0.07 \pm 0.01 \mu\text{m}^2/\text{s}$ and $D_{\text{CD14-Basal}} = 0.11 \pm 0.02 \mu\text{m}^2/\text{s}$ for TLR2 and CD14, respectively, measured from the first lag time $\tau = 0.06$ s. In addition, the immobile fraction was not significantly different between receptors (19% in TLR2 vs. 20% in CD14).

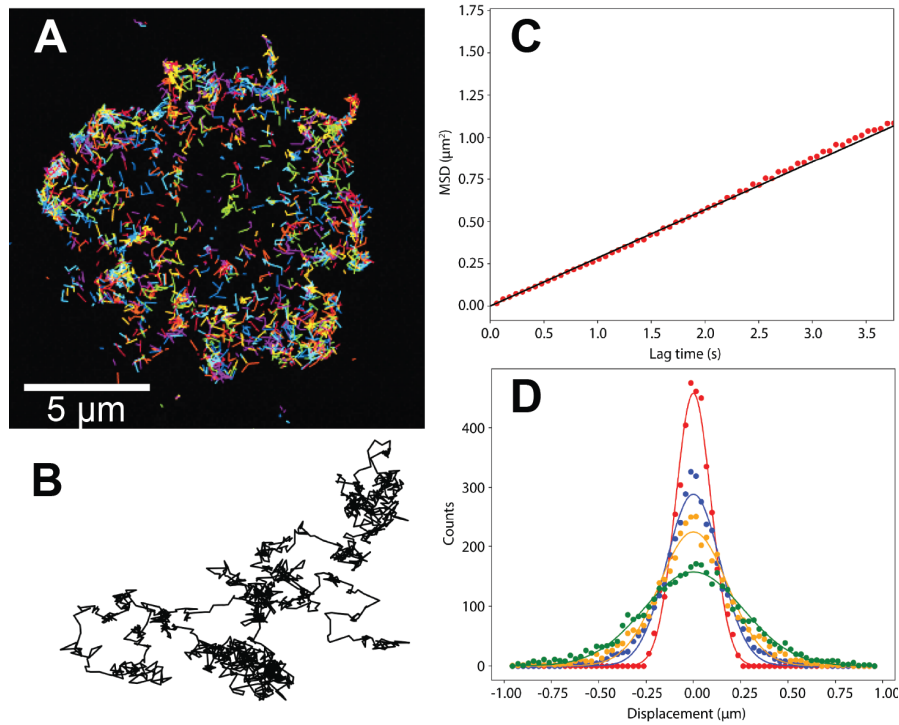


Figure 2.1 Single particle tracking analysis of diffusion in the plasma membrane of RAW 264.7 macrophages. (A) TIRF microscopy image of TLR2 on the basal membrane with tracks of individual particles generated from 300 frames (frame interval 60 ms). (B) Combined track generated from appending 134 individual trajectories. (C) Mean-squared displacement obtained from the combined track and the linear fit to equation $\langle (\Delta r)^2 \rangle (\tau) = 4D\tau$ to determine diffusion coefficient. (D) Distribution of displacements for all trajectories at different lag times (red: $\tau=0.06$ sec, blue: $\tau=0.30$ sec, yellow: $\tau=0.54$ sec, green: $\tau=1.01$ sec). Normal distribution is fitted (solid lines) using equation 2.2.

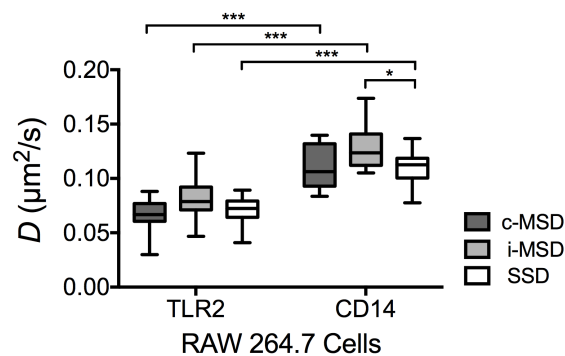


Figure 2.2 Diffusion measurements in the plasma membrane of RAW 264.7 macrophages obtained from single particle tracking and the mean-squared displacement analysis for individual (i-MSD) and combined (c-MSD) tracks and the step-size distribution (SSD). Data is from basal membranes of 15 cells for each type of receptor. Boxes show 25th-75th percentiles with whiskers extending to minimum and maximum values measured (* $P \leq 0.05$, *** $P \leq 0.001$). Statistical significance was analyzed using two-way ANOVA with P values adjusted using Holm-Sidak correction method.

2.3.2 Raster Image Correlation Spectroscopy

We also measured the lateral diffusion of TLR2 and CD14 in the plasma membrane of RAW 264.7 macrophages using raster image correlation spectroscopy. Receptor diffusion was measured in the apical and basal membranes for comparison (Figure 2.3A-B). The basal membrane was defined as the bottom membrane plane, where the cell was making contact with glass, whereas the apical membrane was defined by focusing on the highest observable plane through the cell. A minimum of three measurements in the regions of interest (ROI), in each of the two membrane sections, was acquired for 15 individual cells to determine the diffusion coefficient. Diffusion was obtained from fitting to the autocorrelation function (Figure 2.3C-E). Similar RICS analysis was performed to measure CD14 diffusion.

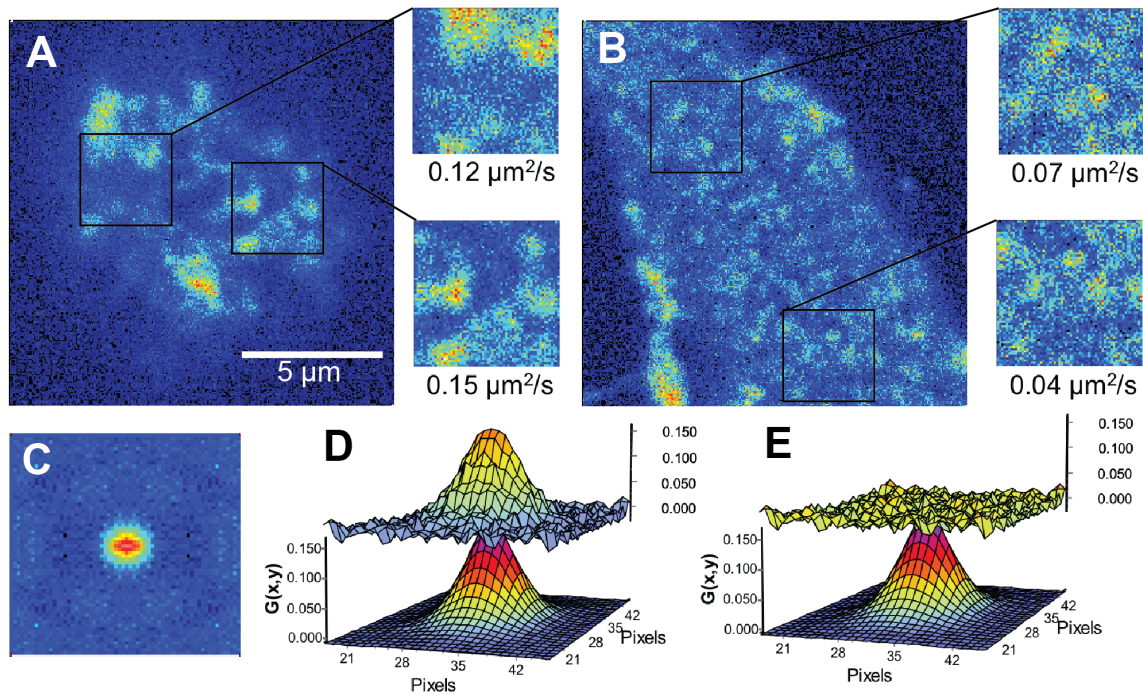


Figure 2.3 Diffusion measurement of TLR2 using RICS on a macrophage plasma membrane. (A) Apical and (B) basal membranes of RAW 264.7 macrophage expressing TLR2 receptor; two 64×64 frames ($3.2 \times 3.2 \mu\text{m}^2$) in each membrane show the regions of interest (ROI) and the diffusion coefficient calculated corresponding to each region. (C) 2D representation of RICS autocorrelation function, (D) Plot of the data (upper surface) and 3D representation of the fit to the function (lower surface), (E) Plot of the residues (upper surface) and the fit (lower surface).

Both TLR2 and CD14 receptors were found to have faster diffusion in the apical membrane ($D_{\text{TLR2-Apical}} = 0.12 \pm 0.03 \mu\text{m}^2/\text{s}$; $D_{\text{CD14-Apical}} = 0.18 \pm 0.03 \mu\text{m}^2/\text{s}$) than in the basal membrane ($D_{\text{TLR2-Basal}} = 0.04 \pm 0.02 \mu\text{m}^2/\text{s}$; $D_{\text{CD14-Basal}} = 0.10 \pm 0.03 \mu\text{m}^2/\text{s}$), as shown in Figure 2.4A-B. The paired comparison *t*-test confirmed the statistical significance of this difference for both CD14 ($P \leq 0.001$) and TLR2 ($P \leq 0.001$). Moreover, CD14 diffusion was faster than TLR2 ($P \leq 0.001$) when similar membrane sections were compared for mobility of these receptors. Figure 2.4C-D demonstrates the relative frequencies of diffusion coefficients for TLR2 and CD14 in the apical and basal membranes. Approximately 33% of measured ROIs for TLR2 and $\sim 3.5\%$ for CD14 had very slow diffusion ($D \leq 0.02 \mu\text{m}^2/\text{s}$) in the basal membrane. In contrast, similar range of diffusion coefficients was found in only $\sim 1.7\%$ and 0% of the ROIs analyzed in the apical membranes for TLR2 and CD14, respectively.

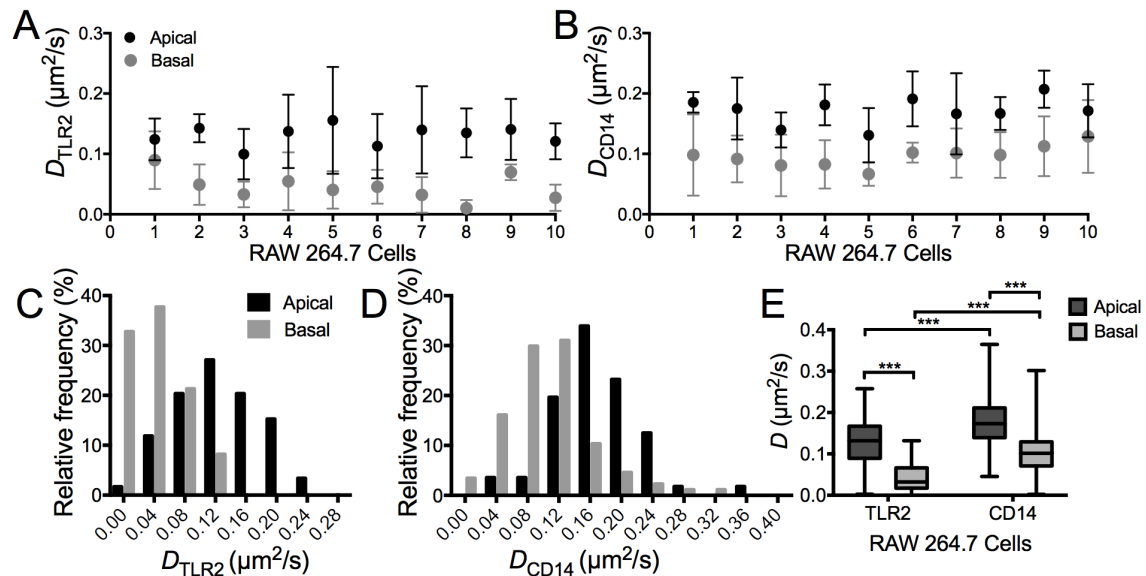


Figure 2.4 Diffusion coefficients of TLR2 and CD14 in the plasma membranes of RAW 264.7 macrophages obtained through raster image correlation spectroscopy. Diffusion D of (A) TLR2 and (B) CD14 in the apical and basal membranes measured from a minimum of three separate ROIs in each membrane section; mean \pm SD for a sample of 10 individual cells is presented. Relative frequency of diffusion coefficients measured for (C) TLR2 and (D) CD14 from a total of 15 cells for each receptor; bin centers shown in the x-axis. (E) Boxes show 25th-75th percentiles with whiskers extending to minimum and maximum values measured. Statistical analysis was performed using paired *t*-test for comparison of apical and basal diffusion, and independent *t*-test between the two receptors ($***P \leq 0.001$). Data is from 15 cells with at least 3 independent ROI measurements in each of the apical and basal membranes.

Table 2.1 Diffusion coefficients of TLR2 and CD14 in the plasma membrane of RAW 264.7 measured by RICS and SPT.

Experimental/Analysis Technique	Membrane Section	Receptor	D (Mean \pm SD) $\mu\text{m}^2/\text{s}$
RICS	Apical	TLR2	0.12 ± 0.03
	Basal	TLR2	0.04 ± 0.02
	Apical	CD14	0.18 ± 0.03
	Basal	CD14	0.10 ± 0.03
SPT/ MSD of individual tracks	Basal	TLR2	0.08 ± 0.02
SPT/ MSD of combined tracks	Basal	TLR2	0.07 ± 0.02
SPT/ Step-size distribution	Basal	TLR2	0.07 ± 0.01
SPT/ MSD of individual tracks	Basal	CD14	0.13 ± 0.02
SPT/ MSD of combined tracks	Basal	CD14	0.11 ± 0.02
SPT/ Step-size distribution	Basal	CD14	0.11 ± 0.02

2.4 Discussion

Among the broad repertoire of receptors on the plasma membrane of macrophages, TLRs and their coreceptors play significant roles in recognition of invading pathogens and initiation of inflammatory responses. TLR2 and CD14 are specifically involved in the detection of bacterial lipopeptides and lipoproteins [29]. The important role of TLR2 and CD14 is evident in the increased susceptibility to infections as a result of dysregulation of these receptors [30]. Consequently, diffusion measurements of these membrane receptors can provide fundamental insights into their behavior and uncover the underlying mechanisms leading to changes in TLR signaling.

Four major families of fluorescence-based microscopy techniques (*i.e.*, FRAP, FCS, ICS, and SPT) along with their extended modalities provide a versatile toolbox for analyzing the dynamics of membrane components. Each technique has their specific advantages, and the choice of method depends on the particular application. A number of comparative studies have been conducted to determine the accuracy and differences in diffusion measurements obtained from FCS and FRAP [31], FCS and SPT [32], FCS and RICS [33]. The results of these comparative studies can help with the selection of appropriate techniques for specific measurements on the membranes. The aim of this study was to obtain accurate diffusion coefficients for two types of plasma membrane receptors in macrophages, TLR2 and CD14, using two different fluorescence-based

imaging techniques. To our knowledge, this is the first study that has directly compared diffusion measurements from SPT and RICS.

Our experimental data shows similar results using SPT and RICS for the diffusion coefficients of CD14 in the basal membranes (Table 2.1). TLR2 diffusion obtained from RICS in the basal membrane was lower compared with SPT results, which could be associated with the ability of RICS to detect confinement within shorter timescales not accessible by SPT. The apical membrane cannot be analyzed using TIRF microscopy, as TIRF-SPT is limited to monitoring species close to the glass surface; therefore, only the basal membranes could be directly compared. To date, there are no previous reports of TLR2 diffusion in RAW 264.7. The diffusion coefficients we measured using RICS and SPT in the basal membrane are slightly lower than the reported value of $0.17 \pm 0.03 \mu\text{m}^2/\text{s}$ measured by FRAP in Chinese Hamster Ovary cells (CHO) transfected with TLR2 [34]. Whether this inconsistency is due to different types of cells, or the fluorescence imaging technique utilized is not clear and could be the subject of further comparative studies. However, similar to FRAP measurements, our MSD data shows simple Brownian diffusion for unstimulated TLR2. Our results are also in agreement with previous SPT measurements of CD14 on RAW 264.7. The diffusion coefficient we obtained from SPT and RICS (Table 2.1) is comparable to the reported value $0.14 \pm 0.02 \mu\text{m}^2/\text{s}$ with MSD plot showing no deviation from Brownian motion [35]. This data further confirms the compatibility of RICS with SPT, which is widely applied in diffusion measurements.

The GPI-anchored receptor CD14 had faster diffusion than the transmembrane receptor TLR2 in RAW 264.7 macrophages. This finding is in agreement with reported data on several chimeras of the two groups of membrane proteins (*i.e.*, transmembrane proteins that were converted to GPI-linked proteins, and the GPI-linked proteins that were transformed to membrane-spanning proteins) [36]. Early FRAP experiments performed on chimeric proteins, including the GPI-linked Thy-1, human placental alkaline phosphatase, and murine surface antigen Ly6E, resulted in diffusion coefficients ~2 to 5-fold faster than transmembrane proteins such as vesicular stomatitis virus G (VSV-G) [36]. However, not all GPI-linked proteins exhibit fast lateral mobility, such as PH-20, a GPI-linked surface antigen with highly restricted diffusion on testicular sperm

before maturation [37]. Whether CD14 diffuses faster than TLR2 to quickly occupy the transmembrane receptor-depleted regions or to compensate for the slow arrival of antigen-bound TLRs would require further investigation of the kinetics of receptor-ligand binding events.

SPT studies are typically performed using TIRF and therefore the reported diffusion coefficients are based on data acquired from the basal membrane in contact with glass. While these measurements can provide valuable insight into the dynamics of certain plasma membrane proteins that mostly reside in the basal membrane, such as those involved in adhesion to substrates or the extracellular matrix, many others have to be analyzed on the apical or lateral membrane to capture their true dynamic behavior. As an example, epithelial cells are polarized, with different parts of the cell responsible for performing distinct functions. Consequently, their plasma membranes are divided into distinct apical and basolateral domains that differ in protein composition, with specific proteins that are restricted to diffuse within only the apical or basolateral sections [38]. Although diffusion has been previously compared in the lateral and basal membranes of Madin-Darby Canine Kidney epithelial cells using combination of micropatterning and K-space image correlation spectroscopy [39], most diffusion measurements reported in the literature are from one membrane section; typically the basal membrane in SPT and only one of the apical or basal membranes in FRAP experiments, depending on the imaging apparatus.

Accurate diffusion measurements of key immunoreceptors such as TLR2 and CD14 can elucidate their binding and signaling mechanisms, which can in turn lead to rational development of potential therapeutic strategies to tune or amplify their response in cells that are impaired due to aging or disease.

2.5 Conclusion

In summary, we have obtained comparable diffusion measurements using RICS and SPT for the lateral movement of a GPI-anchored and a transmembrane receptor in the plasma membrane of RAW 264.7 macrophages. Both techniques revealed higher diffusion of CD14 compared with TLR2. While RICS allows measuring the diffusion in different planes through the cell body, SPT shows the trajectories of individual particles in

the nearest planar section of the membrane in contact with glass. Consequently, RICS and SPT can be used as complementary methods for studying membrane dynamics.

2.6 Reference

- [1] G. L. Nicolson, “The Fluid - Mosaic Model of Membrane Structure: Still relevant to understanding the structure, function and dynamics of biological membranes after more than 40 years,” *Biochim. Biophys. Acta - Biomembr.*, vol. 1838, no. 6, pp. 1451–1466, 2014.
- [2] C. Manzo and M. F. Garcia-parajo, “A review of progress in single particle tracking : from methods to biophysical insights,” *Rep. Prog. Phys.*, vol. 78, p. 124601, 2015.
- [3] J. Lippincott-schwartz, E. Snapp, and A. Kenworthy, “Studying protein dynamics in living cells,” vol. 2, no. June, 2001.
- [4] M. A. Digman and E. Gratton, “Lessons in Fluctuation Correlation Spectroscopy,” *Annu. Rev. Phys. Chem. Vol 62*, vol. 62, no. December, pp. 645–668, 2011.
- [5] D. L. Kolin and P. W. Wiseman, “Advances in Image Correlation Spectroscopy : Measuring Number Densities , Aggregation States , and Dynamics of Fluorescently labeled Macromolecules in Cells,” pp. 141–164, 2007.
- [6] A. Carisey, M. Stroud, R. Tsang, and C. Ballestrem, “Fluorescence Recovery After Photobleaching,” *Methods Mol. Biol.*, vol. 769, pp. 387–402, 2011.
- [7] D. M. Soumpasis, “Brief Communication Theoretical Analysis Of Fluorescence Photobleaching Recovery Experiments,” *Biophys. J.*, vol. 41, no. 1, pp. 95–97, 1983.
- [8] D. Magde, E. Elson, and W. Webb, “Thermodynamic fluctuations in a reacting system: measurement by fluorescence correlation spectroscopy,” *Phys. Rev. Lett.*, vol. 29, pp. 705–8, 1972.
- [9] D. Magde, E. L. Elson, and W. W. Webb, “Fluorescence correlation spectroscopy. II. An experimental realization.,” *Biopolymers*, vol. 13, no. 1, pp. 29–61, 1974.
- [10] M. A. Digman, P. Sengupta, P. W. Wiseman, C. M. Brown, A. R. Horwitz, and E. Gratton, “Fluctuation correlation spectroscopy with a laser-scanning microscope: exploiting the hidden time structure.,” *Biophys. J.*, vol. 88, no. 5, pp. L33-6, 2005.
- [11] M. A. Digman, C. M. Brown, P. Sengupta, P. W. Wiseman, A. R. Horwitz, and E. Gratton, “Measuring fast dynamics in solutions and cells with a laser scanning

- microscope.,” *Biophys. J.*, vol. 89, no. 2, pp. 1317–1327, 2005.
- [12] M. J. Rossow, J. M. Sasaki, M. A. Digman, and E. Gratton, “Raster image correlation spectroscopy in live cells.,” *Nat. Protoc.*, vol. 5, no. 11, pp. 1761–1774, 2010.
- [13] E. Gielen *et al.*, “Measuring diffusion of lipid-like probes in artificial and natural membranes by raster image correlation spectroscopy (RICS): use of a commercial laser-scanning microscope with analog detection,” *Langmuir*, vol. 25, no. 9, pp. 5209–5218, 2009.
- [14] M. A. Digman and E. Gratton, “Analysis of diffusion and binding in cells using the RICS approach.,” *Microsc. Res. Tech.*, vol. 72, no. 4, pp. 323–332, 2009.
- [15] C. M. Brown, R. B. Dalal, B. Hebert, M. A. Digman, A. R. Horwitz, and E. Gratton, “Raster image correlation spectroscopy (RICS) for measuring fast protein dynamics and concentrations with a commercial laser scanning confocal microscope,” *J. Microsc.*, vol. 229, no. 1, pp. 78–91, 2008.
- [16] M. A. Digman, P. W. Wiseman, A. R. Horwitz, and E. Gratton, “Detecting protein complexes in living cells from laser scanning confocal image sequences by the cross correlation raster image spectroscopy method,” *Biophys. J.*, vol. 96, no. 2, pp. 707–716, 2009.
- [17] C. Eich *et al.*, “Changes in membrane sphingolipid composition modulate dynamics and adhesion of integrin nanoclusters,” *Sci. Rep.*, vol. 6, p. 20693, 2016.
- [18] S. A. Freeman *et al.*, “Transmembrane pickets connect cyto-and pericellular-skeletons forming barriers to receptor engagement,” *Cell*, vol. 172, no. 1–2, p. 305–317.e10, 2018.
- [19] I. Botos, D. Segal, and D. Davies, “The structural biology of Toll-like receptors,” *Structure*, vol. 19, no. 4, pp. 447–459, 2011.
- [20] S. Akira and K. Takeda, “Toll-like receptor signalling,” *Nat. Rev. Immunol.*, vol. 4, no. 7, pp. 499–511, 2004.
- [21] J. Pugin, I. Heumann, A. Tomasz, and E. Al, “CD14 is a pattern recognition receptor,” *Immunity*, vol. 1, pp. 509–516, 1994.
- [22] K. Jaqaman and S. Grinstein, “Regulation from within: The cytoskeleton in transmembrane signaling,” *Trends Cell Biol.*, vol. 22, no. 10, pp. 515–526, 2012.

- [23] T. A. da Silva, A. L. V Zorzetto-Fernandes, N. T. Cecílio, A. Sardinha-Silva, F. F. Fernandes, and M. C. Roque-Barreira, “CD14 is critical for TLR2-mediated M1 macrophage activation triggered by N-glycan recognition,” *Sci. Rep.*, vol. 7, no. 1, p. 7083, 2017.
- [24] W. C. Raschke, S. Baird, P. Ralph, and I. Nakoinz, “Functional macrophage cell lines transformed by Abelson leukemia virus.,” *Cell*, vol. 15, no. 1, pp. 261–267, 1978.
- [25] M. Cheezum, W. Walker, and W. Guilford, “Quantitative comparison of algorithms for tracking single fluorescent particles.,” *Biophys. J.*, vol. 81, pp. 2378–2388, 2001.
- [26] R. E. Thompson, D. R. Larson, and W. W. Webb, “Precise nanometer localization analysis for individual fluorescent probes.,” *Biophys. J.*, vol. 82, pp. 2775–2783, 2002.
- [27] I. Smal, M. Loog, W. Niessen, and E. Meijering, “Quantitative Comparison of Spot Detection Methods in Fluorescence Microscopy,” *IEEE Trans. Med. Imaging*, vol. 29, no. 2, pp. 282–301, 2010.
- [28] J. R. Lakowicz, *Principles of Fluorescence Spectroscopy*, Third Edit. 2006.
- [29] J. van Bergenhenegouwen *et al.*, “TLR2 & Co: a critical analysis of the complex interactions between TLR2 and coreceptors.,” *J Leukoc Biol*, vol. 94, no. 5, pp. 885–902, 2013.
- [30] D. van Duin *et al.*, “Age-Associated Defect in Human TLR-1/2 Function,” *J. Immunol.*, vol. 178, pp. 970–975, 2007.
- [31] M. Radek, Y. H. Foo, and T. Wohland, “Article On the Equivalence of FCS and FRAP : Simultaneous Lipid Membrane Measurements,” pp. 152–161, 2016.
- [32] M. Rose, N. Hirmiz, J. M. Moran-Mirabal, and C. Fradin, “Lipid diffusion in supported lipid bilayers: A comparison between line-scanning fluorescence correlation spectroscopy and single-particle tracking,” *Membranes (Basel)*, vol. 5, no. 4, pp. 702–721, 2015.
- [33] P. D. Moens, E. Gratton, and I. L. Salvemini, “Fluorescence correlation spectroscopy, Raster image correlation spectroscopy and Number & Brightness on a commercial confocal laser scanning microscope with analog detectors (Nikon

- C1),” *Microsc. Res. Tech.*, vol. 74, no. 4, pp. 377–388, 2011.
- [34] M. Triantafilou, S. Morath, A. Mackie, T. Hartung, and K. Triantafilou, “Lateral diffusion of Toll-like receptors reveals that they are transiently confined within lipid rafts on the plasma membrane,” *J Cell Sci*, vol. 117, no. Pt 17, pp. 4007–4014, 2004.
- [35] L. Weimann *et al.*, “A Quantitative Comparison of Single-Dye Tracking Analysis Tools Using Monte Carlo Simulations,” *PLoS One*, vol. 8, no. 5, p. e64287, 2013.
- [36] F. Zhang *et al.*, “Lateral Diffusion of Membrane-spanning and Glycosylphosphatidylinositol-linked Proteins: Toward Establishing Rules Governing the Lateral Mobility of Membrane Proteins,” *J. Cell Biol.*, vol. 115, no. 1, pp. 75–84, 1991.
- [37] B. M. Phelps, P. Primakoff, D. E. Koppel, M. G. Low, and D. G. Myles, “Restricted lateral diffusion of PH-20, a PI-anchored sperm membrane protein,” *Science.*, vol. 240, pp. 1780–1782, 1988.
- [38] J. L. Lee and C. H. Streuli, “Integrins and epithelial cell polarity,” *J. Cell Sci.*, vol. 127, pp. 3217–3225, 2014.
- [39] S. Marlar, E. C. Arnspang, G. A. Pedersen, J. S. Koffman, and L. N. Nejsum, “Measuring localization and diffusion coefficients of basolateral proteins in lateral versus basal membranes using functionalized substrates and kICS analysis,” *Biochim. Biophys. Acta - Biomembr.*, vol. 1838, no. 10, pp. 2404–2411, 2014.

Chapter 3

Macrophages on Silica Films

Macrophages are major contributors to the rejection of foreign materials introduced to living tissues. Given that cell-surface interactions can have important effects on phagocytic capacity and cytokine production, changes in macrophage morphology have been reported for different materials and surface patterns. However, the details of how surface topography impacts morphology and function remain unclear. The study presented in this chapter investigates whether changes in surface topography of glassy substrates alter macrophage shape, phagocytic function, and pro-inflammatory response.

The content of this chapter is published in *Advanced Materials Interfaces*, 6 (21) 2019, 1900677. © Copyright 2019 WILEY-VCH Verlag GmbH & Co. KGaA, Weinheim

3.1 Introduction

Macrophages are sentinel cells of the innate immune system that have diverse functions including the initiation of inflammatory responses, phagocytosis of pathogens and foreign entities, maintaining homeostasis, and wound healing [1]. Macrophages often contribute to the rejection of implants as these cells adhere to foreign materials and initiate immune responses by producing pro-inflammatory cytokines [2]. Consequently, understanding how a material's properties alter the adherence, inflammatory responses, and phagocytic function of macrophages is essential for the development of appropriate materials for biomedical applications such as those for hip replacements [3] and cochlear implants [4].

Macrophages can sense topographical features at the submicron scale, which determines whether they will spread across the surface or initiate phagocytosis [5,6]. Adherent macrophages exhibit a wide range of cell shapes including amoeboid, elongated spindle-like, or round depending on their lamellipodial extensions [7]. Macrophages with spindle-like morphology are more likely to have a pro-healing phenotype, which contributes to tissue repair and wound healing, whereas the rounded "fried-egg" morphology shows pro-inflammatory behavior [8].

Surface topography has been proposed as a way to regulate the morphology and function of macrophages [9]. Surface patterns such as microgrooves [10–13], wrinkles [14], and concave/convex microstructures [15] have been reported to alter inflammatory responses of macrophages. For example, it has been observed that 2 and 10 μm -width grooves in fused silica result in the elongation of macrophages and improved phagocytosis of microbeads compared with flat surfaces [16]. In contrast, convex and concave patterns on poly(dimethylsiloxane) (PDMS) do not impact the expression of surface markers despite inducing significant changes in cell morphology [15]. Modification of surface chemistry such as charge and hydrophobicity can also impact macrophage phenotype [17–19]; however, topographical effects are believed to override the influence of surface chemistry [9]. The effect of a wide range of materials including titanium [11,17,20,21], polyvinylidene fluoride [22], perfluoropolyether [23], PDMS [10,14,15], fused silica [16], poly(ϵ -caprolactone) (PCL) and poly(lactic acid) (PLA) [10] with micro- and nanostructures have been investigated on macrophage morphology and inflammatory

responses with conflicting results. Consequently, the mechanisms by which topography alters macrophage phenotype and function remain unclear.

In this work, we investigated the morphology and function of murine bone marrow-derived macrophages cultured on glassy silica films with topographical features of different sizes. SiO₂ is a biocompatible, nontoxic, and inexpensive material that is used to coat implant surfaces to improve corrosion resistance [24,25]. To evaluate the impact of topography on macrophage morphology and function, micro- and nanostructured SiO₂ surfaces were fabricated using a previously established thermal shrinking technique [26]. We hypothesized that surface topography could impact macrophage morphology, phagocytic capacity, inflammatory responses, and plasma membrane receptor mobility. Thus, we investigated whether surface topography impacted phagocytosis of *Streptococcus pneumoniae*, pro-inflammatory cytokine IL-6 production, and lateral diffusion of toll like receptor 2 (TLR2). Our data indicates that structured SiO₂ films alter macrophage morphology and increase their phagocytic capacity; however, they do not change the production of pro-inflammatory cytokine IL-6 or the diffusion of the membrane receptor TLR2.

3.2 Experimental Section

3.2.1 Substrate Preparation

Micro- and nanostructured glassy SiO₂ substrates were fabricated using a method previously described [26]. Pre-stressed polystyrene (PS) sheets (Graphix Shrink Film, Graphix, Maple Heights, OH) were cut into 2×2 cm substrates with a Robo Pro CE5000-40-CRP cutter and CB15UB blade (Graphtec America Inc., Irvine, CA). The PS substrates were cleaned for 5 minutes in sequential isopropanol, ethanol, and water baths, under orbital agitation (70 rpm), and dried using a nitrogen stream. Thin SiO₂ films (2 and 50 nm-thick) were deposited onto clean PS substrates from a high purity silica target (LTS Chemical Inc., Chestnut Ridge, New York) using a Torr Compact Research Coater CRC-600 manual planar magnetron sputtering system (New Windsor, New York). The coated substrates were then thermally shrunken to produce micro- or nanostructured films using an Isotemp vacuum oven (Fisher Scientific, Ottawa, ON, Canada) at 160°C for 3 minutes. To investigate the effect of plasma oxidation, the SiO₂ substrates were treated in a plasma chamber (Harrick, Ithaca, NY) for 60 s at high power

(30 W) with a partial air pressure of 600 mTorr, 30-45 minutes before seeding the cells.

3.2.2 White Light Interferometry

The roughness of structured substrates was assessed through white light interferometry microscopy (WLIM) using a Zygo NewView5000 (Zygo Corporation, Middlefield, CT, USA). Measurements were taken with a CCD camera, with 50× objectives and additional 2× optical magnification, resulting in fields of view of 70 × 50 μm to obtain the root mean square (RMS) and peak-to-valley (P-V) values, respectively. A Fast Fourier Transform (FFT) band pass filter was applied for all measurements, using cut-off frequencies of 180.35 and 558.79 mm⁻¹. RMS and P-V values were obtained from MetroPro software for 3-5 areas on each sample and across triplicate substrates (Supporting Information Figure S3.1).

3.2.3 Water Contact Angle Measurements

The wettability was measured for all substrates using an OCA 35 video-based contact angle instrument (Future Digital Scientific, Garden City, NY, USA). Using the sessile drop method, 3 μL of water was dropped onto dry surfaces and a static image was captured immediately after contact. The contact angle was measured with the SCA 20 software (Future Digital Scientific) and was obtained for three replicate substrates.

3.2.4 Macrophage Culture

Bone marrow progenitors from 10-14 wk C57BL/6 mice (The Jackson Laboratory, Maine, USA) were isolated from spines according to previously published methods [27]. Progenitor cells were cultured for 7 days in RPMI-1640 supplemented with 10% fetal bovine serum (FBS), 1% L-glutamine, 1% penicillin/streptomycin, and 15% L929 fibroblast cell conditioned medium on 150 mm Petri dishes (Fisherbrand) as per standard protocols [27,28]. Differentiated macrophages were incubated with Accutase for 5 minutes and gently lifted using a cell lifter. Cells were then plated at a density of 50,000 cells/cm² on each SiO₂ substrate, 24 hrs before imaging. For each type of substrate, three technical replicates were performed. All animal manipulations were done according to protocols approved by McMaster's Animal Research Ethics Board.

3.2.5 Scanning Electron Microscopy

Substrates with adhered cells were fixed overnight using 2% (v/v) glutaraldehyde in 0.1 M phosphate buffer pH 7.4. The samples were rinsed two times in buffer solution, and the membranes were fixed using 1% osmium tetroxide in 0.1 M phosphate buffer for 1 hr, and dehydrated in a graded ethanol series increasing in concentration: 50, 70 (2×), 95 (2×), and 100% (2×). The samples were then dried using a Leica EM CPD300 critical point dryer (Leica Mikrosysteme GmbH, Wien, Austria) and coated with ~20 nm of gold using a Polaron Model E5100 sputter coater (Polaron Equipment Ltd., Watford, Hertfordshire). Images were captured using a Tescan Vega II LSU scanning electron microscope (Tescan USA, PA), operating at an accelerating voltage of 20kV.

3.2.6 Epifluorescence Imaging

Cell samples were washed 3× with PBS and fixed with 0.4% w/v *p*-formaldehyde and 0.1% v/v glutaraldehyde (Sigma Aldrich, Oakville, ON, Canada) in PBS for 15 min. After 3× washes with PBS, the fixation was quenched by incubation with a 25 mM glycine (Sigma Aldrich, Oakville, ON, Canada) solution in PBS for 10 min. The glycine solution was replaced by a 0.2% w/v fish gelatin and 0.2% w/v bovine serum albumin (BSA) (Sigma Aldrich, Oakville, ON, Canada) solution in PBS, and the samples were incubated for 15 min to block the surface from non-specific binding. All fixatives were added at room temperature. The fixed cells were stored in PBS at 4°C until imaging. For staining, the cell membrane was permeabilized using a 0.2% v/v Triton-X solution (Sigma Aldrich, Oakville, ON, Canada), according to the manufacturers' directions. The cell nuclei were stained with a 600 nM 4,6-diamidino-2-phenylindole dihydrochloride (DAPI) (Invitrogen, Burlington, ON, Canada), and the actin filaments were labeled with Alexa Fluor 488-phalloidin (Invitrogen, Burlington, ON, Canada). The fluorescent samples were then imaged in PBS with a Nikon Eclipse LV100N POL epifluorescence microscope (Nikon Instruments, Mississauga, ON, Canada) equipped with a 60×/0.9NA physiological objective and a Retiga 2000R camera (QImaging, Surrey, BC, Canada). Fluorescence images were captured using NIS Elements software (Nikon Instruments, Mississauga, ON, Canada).

3.2.7 Fractal Analysis

Fractal analysis based on the box counting method was used to quantitatively assess cellular morphology. This method determines the complexity of a geometrical figure by counting how many boxes of a given size are required to cover an area or perimeter, and doing this process for a range of box sizes [29]. Epifluorescence images of macrophages were converted into binary maps where the cell surface and background area were represented by ones and zeros, respectively (Supporting Information, Figure S3.7), and were cropped to contain mostly the cell. Each binary image was then introduced to our box counting algorithm written in MATLAB (MathWorks) and was placed on grids of box sizes from $s = 1$ to $s = \text{maximum width}/2$, where the width was defined as the smallest of the two dimensions of the image. The number of boxes contained in each cell (ones in the binary map) was counted. This method generated two graphs with the x-axis as $\log(N)$ and the y-axis as $\log(1/s^2)$, where N and s represent the number and size of the boxes, respectively. The slope of the graphs represents the fractal dimension F_{DA} for the area and F_{DP} for the perimeter. A sample of 10 cells was imaged and analyzed per substrate with three substrate replicates, yielding a total of 30 cells per treatment.

3.2.8 *Streptococcus pneumoniae* Internalization Assay

S. pneumoniae strain P1121 (clinical isolate, serotype 23F, provided by Dr. J. N. Weiser, University of Pennsylvania, PA, USA) with $OD_{600} = 0.5$ was heated for 10 min at 65°C to kill the bacteria, which was then digested with lysozyme and labeled with 20 ng/mL of TRITC (Invitrogen, Burlington, ON) for 30 min at 37°C. The fluorescent bacteria were then incubated with macrophages for 1.5 hr at a multiplicity of infection of 50 bacteria per cell (MOI 50) and washed with PBS subsequently. The internalized bacteria were measured on a SpectraMax i3 plate reader (Molecular Devices, San Jose, CA, USA) at 555 nm excitation and 580 nm emission wavelengths. Relative fluorescence values (rfu) were corrected for autofluorescence and nonspecific bacterial adsorption onto the substrates. All experiments were performed in triplicate. Macrophages were then fixed and stained for fluorescent imaging as previously described.

3.2.9 Interleukin-6 (IL-6) Enzyme-linked Immunosorbent Assay (ELISA)

BMDMs were seeded at a density of 1×10^5 cells/cm² and stimulated with 500 ng/mL of Pam3Csk4 (Invivogen, San Diego, CA, USA) for 24 hr. Supernatants were collected and frozen at -80°C until quantification of IL-6 secretion by ELISA (eBioscience, CA, USA), which was performed as per the manufacturer's directions.

3.2.10 Diffusion Measurements

All imaging was performed in RPMI-1640 Medium, without phenol red (Life Technologies- Gibco™). TLR2 was visualized using Alexa Fluor 647-conjugated anti-TLR2/CD282, by adding 1 μ L of the staining monoclonal antibody (0.2 mg/mL stock concentration) to 2 mL of the imaging media. Antibody staining was performed at 4°C for 1 hr to prevent receptor internalization, after which the samples were washed 3 \times with PBS and the media was replaced with RPMI containing 5 mM ascorbic acid to minimize photobleaching during imaging. The substrates were inverted on glass bottom dishes and imaging was performed on a heated stage set to 37°C.

Raster-scan images were collected using confocal laser-scanning microscopy (CLSM) (Nikon Microscope ECLIPSE LV100ND) on an inverted microscope fitted with a 60x/1.40NA Plan Apo λ oil-immersion objective. Excitation was from 647-nm laser line attenuated to 0.30-0.70% of the nominal laser power (20 mW). A pinhole size of 1.2 AU (47.3 μ m) was chosen for imaging. For scanning the basal membrane, the plane of focus was set as close as possible to the bottom membrane plane, where the cell was making contact with the substrate. The apical membrane was found by focusing on the highest observable plane through the cell.

For raster image correlation spectroscopy (RICS), 256 \times 256-pixel images were collected using NIS imaging software (NIS-Elements AR 4.30.02) at 16.66x zoom, corresponding to a pixel size of 50 nm. The pixel dwell time was set to 23.8 μ s/pixel, and the line time to 7.858 ms for raster-scanning live cells. Stacks of 50 images were captured with no delay between frames. Imaging of live cells was performed at 37°C using a stage top incubator (TOKAI HIT, INUBG2ATW-TIZW) in combination with a heated collar around the objective.

Diffusion data were extracted from the images using SimFCS software (Laboratory of Fluorescence Dynamics, University of California, Irvine) [30]. Regions of interest were selected with frame sizes of 64×64 pixels (3.2×3.2 μm²) for each cell (Supporting Information Figure S3.8). Diffusion was measured using the known parameters of pixel dwell time, line time, size of each pixel, and the beam waist. For each stack of images, the RICS function was calculated as the average of all images of the stack (Supporting Information Figure S3.9). Data were obtained from 20-25 cells for each of the SiO₂ conditions, using a minimum of three replicate samples per condition. A focal volume waist (ω_0) of 0.264 μm was estimated for the excitation beam by measuring the autocorrelation curve of a freely diffusing dUTP (SIGMA/19475, Aminoallyl-dUTP-Cy[®]5 triethylammonium salt solution, ≥95.0% HPLC). Further details on the calibration method are provided in the Supporting Information.

3.2.11 Cell Viability Test

Cell viability was measured for all SiO₂ conditions with Zombie Red™ (BioLegend, excitation: 600 nm, emission: 624 nm) added at 1:1000 dilution 30 min prior to imaging. Similar to the protocol used for the RICS experiments, the samples were incubated at 4°C for 1hr in RPMI-1640 without phenol red, followed by 120 min at 37°C on the stage top incubator of the microscope, in the imaging media containing 5 mM ascorbic acid. The samples were then washed with PBS and fixed with 2% paraformaldehyde in PBS (15 min incubation). The nuclei were then labeled with DAPI and the samples were imaged using the confocal microscope to count the viable cells. To verify the accuracy of the Zombie Red, the fixed samples were also stained. 100% of paraformaldehyde fixed cells stained positive with Zombie Red. Less than 5% of viable cells stained positive for all SiO₂ substrate conditions.

3.2.12 Statistical Analysis

Statistical analysis and plotting was performed using SPSS software (IBM SPSS Statistics 21) and Prism 7.0a (GraphPad Software Inc.), respectively. Differences were considered statistically significant at P values of < 0.05.

3.3 Results

3.3.1 Surface Characterization

Thermal shrinking of a shape-memory polymer substrate coated with thin SiO₂ films produced topographies that were dependent on the initial film thickness (Figure 3.1). The substrates coated with 2 nm-thick films (labeled as 2S) displayed nanoscale wrinkles after shrinking, while the 50 nm-thick (50S) substrates formed micrometer ones. The wrinkles were randomly distributed on both substrates. Quantitative information on the height/depth of the topographic features was acquired using white light interferometry microscopy – WLIM (Supporting Information Figure S1). Roughness measurements showed P-V values of $2.0 \pm 0.2 \mu\text{m}$ and $9 \pm 1 \mu\text{m}$ for 2S and 50S substrates, respectively, and RMS values of $250 \pm 10 \text{ nm}$ and $860 \pm 90 \text{ nm}$ for 2S and 50S substrates, respectively. The topographies of the structured materials were much larger than those of the flat SiO₂ films, which had RMS roughness values of $0.657 \pm 0.008 \text{ nm}$, as calculated from AFM images (Supporting Information Figure S3.2). The surface wrinkles on 2S substrates were shown by WLIM to be on the order of hundredths of nanometers and were seen by SEM to be decorated with small corrugations (Figure 3.1B). In contrast, film cracking on the order of microns was observed for 50S substrates (Figure 3.1C).

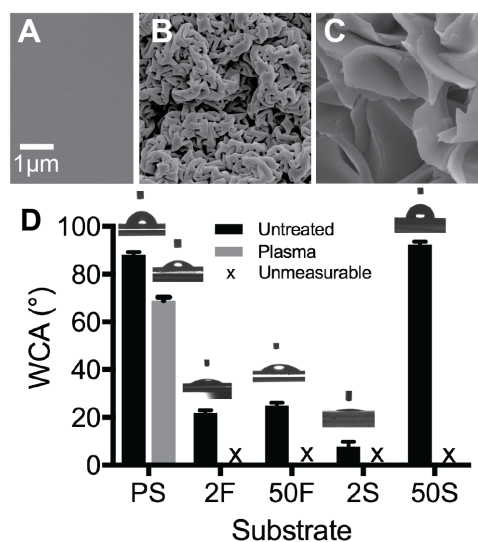


Figure 3.1 Characterization of fabricated substrates. SEM images of (A) flat, (B) 2 nm, and (C) 50 nm SiO₂ films after thermal shrinking. (D) WCA measurements of untreated and plasma treated polystyrene (PS), 2 nm flat SiO₂ (2F), 50 nm flat SiO₂ (50F), 2 nm structured SiO₂ films (2S), and 50 nm structured SiO₂ films (50S). Bars represent the mean of three independent experiments \pm SEM. Unmeasurable: plasma treated films were super-hydrophilic.

The wettability of all substrates and the impact of plasma treatment on hydrophilicity were assessed using water contact angle (WCA) (Figure 3.1D). Untreated PS was hydrophobic (WCA > 90°) whereas the flat 2 and 50 nm SiO₂ substrates (labeled as 2F and 50F) were hydrophilic and had similar contact angles (~20°- 30°). Upon shrinking the substrates, a significant decrease in the WCA of 2S (from 22° to 8°) and a significant increase in the WCA of 50S (from 25° to 92°) were observed. In an effort to render the test surfaces hydrophilic, all substrates were oxidized with air plasma. PS became more hydrophilic (WCA of 69° vs. 88°), and SiO₂ substrates became super-hydrophilic with WCAs that could not be measured.

3.3.2 Cell Morphology

The adhesion and morphology of cells cultured on the SiO₂ substrates with different topographies were qualitatively evaluated through SEM imaging. In general, macrophages exhibited heterogeneous morphologies; nevertheless, certain morphologies were more predominant on specific structured substrates. While no significant difference was observed in the number of cells adhered to the different surface topographies (as assessed through cell staining and counting, Supporting Information Figure S3.3), SEM images (Figure 3.2) revealed differences in cell morphology in response to changes in the surface topography from flat to rougher SiO₂. Macrophages on the flat SiO₂ and 2 nm SiO₂ structured surfaces displayed either elongated or “fried egg” shapes (as typically seen in cell culture dishes) with numerous filopodial extensions, although a more uniform spreading of the basal cell membrane between filopodia was seen in the flat substrate. On the rougher substrate (50S), macrophages were more frequently star-shaped with several anchor points on the ridges of the wrinkles, and very few filopodia. Moreover, the surface of most cells appeared smoother with less prominent membrane ruffling. Similarly, plasma treatment did not result in any obvious changes in the attachment and morphology of the cells compared to untreated samples (Supporting Information Figure S3.4).

Cell morphology changes were quantitatively assessed by calculating the area and perimeter fractal dimensions as measures of the complexity of the cell shape. A fractal dimension analysis in general reports on the complexity of the object across length scales.

The fractal dimension for the perimeter (FDP) reports on the complexity of the cell boundary, regardless of whether this is for filipodia, lamellipodia or any other cellular extension. Similarly, the fractal dimension for the area (FDA) reports on the complexity of the area covered by a 2-dimensional object. As illustrative examples, one can consider circle, rectangle, and star shapes and calculate their FDA and FDP (Supporting Information, Figure S3.5). Since 2D images are analyzed, the fractal dimension values expected would lie between 1 and 2, representing the dimensions of a line and square, respectively. The reader will see that the FDA of these sample figures increases as the area becomes less isotropic (in increasing order: star, rectangle, circle), while, the FDP increases as the perimeter deviates from a straight line (in increasing order: rectangle, circle, star). A similar approach was used to determine the FDP and FDA for cells incubated on all surface conditions using the box-counting method (10 cells per substrate, with three replicates for a total of 30 cells per condition). Macrophages cultured on 50S substrates exhibited significantly lower FDA and FDP values compared to those cultured on 2S substrates, for both plasma-treated and untreated substrates (Figure 3.3). The FDP value was significantly higher for cells on 2S substrates compared with flat surfaces while their FDA values did not show any significant difference. Additionally, when looking at individual conditions, the plasma treatment did not significantly change the FDA and FDP of the adherent macrophages, consistent with the qualitative observation that plasma treatment does not significantly change cell morphology.

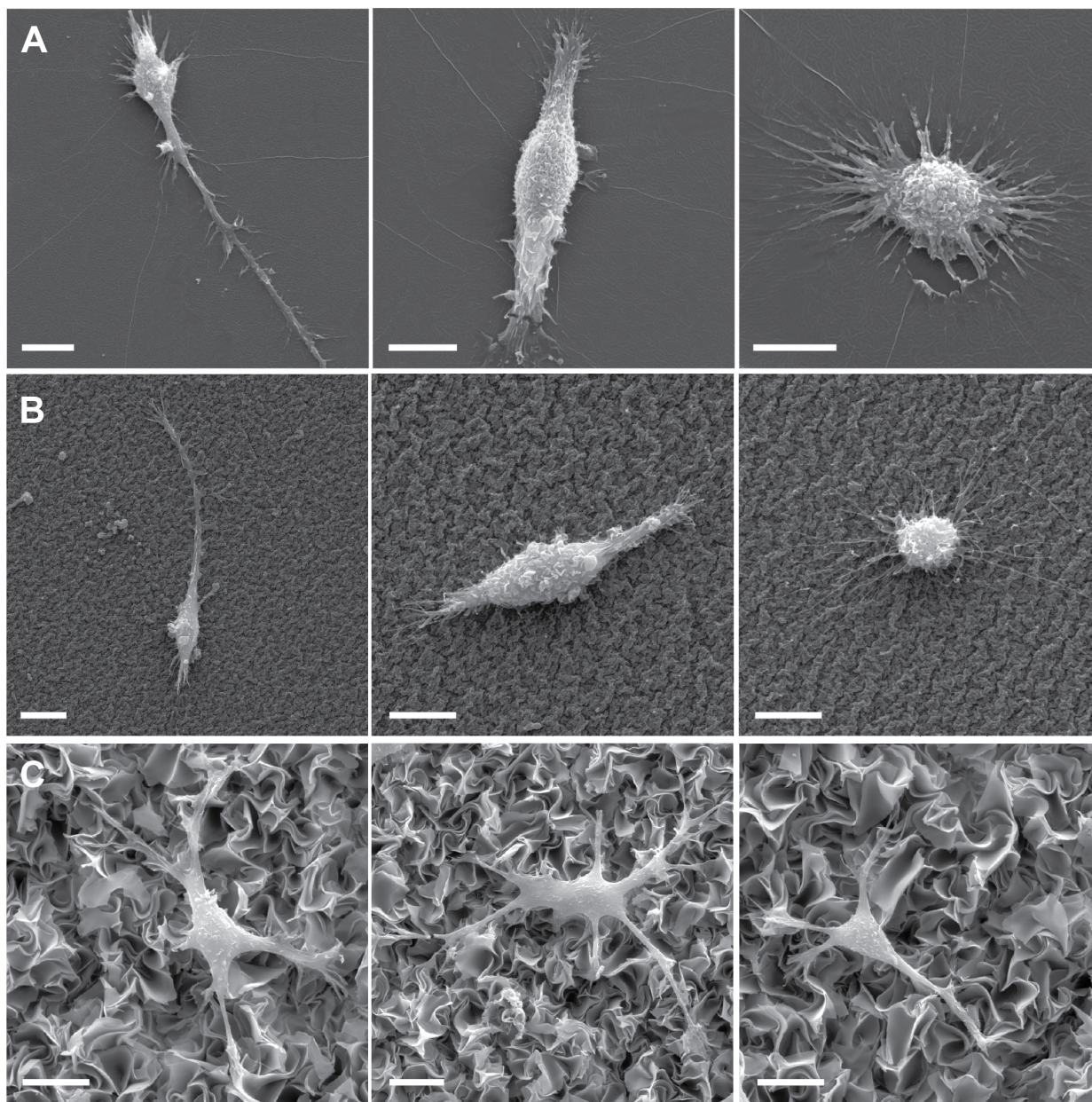


Figure 3.2 Representative SEM images of macrophages adhered to SiO₂ substrates, showing differences in cell morphology in response to rougher topography. (A) 50F control, (B) 2S, (C) 50S. All scale bars represent 10 μ m.

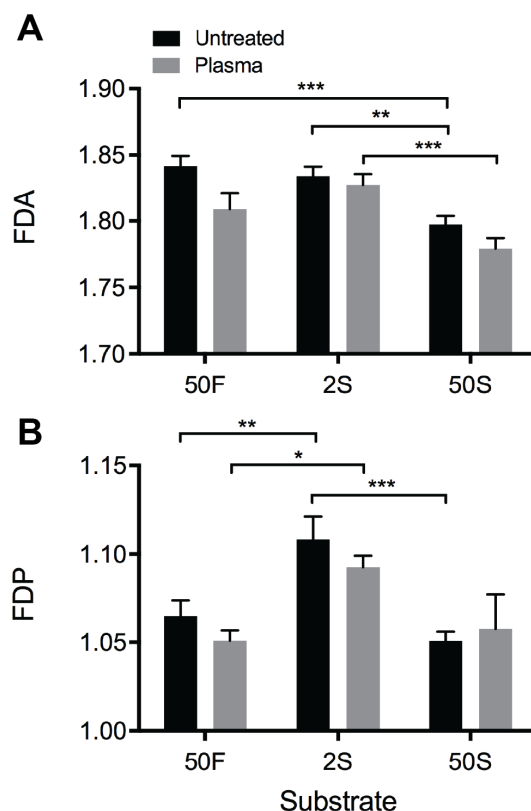


Figure 3.3 Quantitative assessment of cell morphology using fractal dimension. (A) Fractal dimension area (FDA) and (B) Fractal dimension perimeter (FDP) values for BMDMs on different substrates: plasma treated vs. untreated 50 nm flat SiO₂ (50F), 2 nm structured SiO₂ (2S), and 50 nm structured SiO₂ (50S). Bars represent the mean ± SEM, for n = 30 cells evaluated (from three substrate replicates with 10 cells per substrate). One-way ANOVA with Tukey’s post hoc test for comparison between substrates, and multiple *t*-tests between untreated and plasma-treated substrates with *P* values adjusted using Holm-Sidak correction method (**P* ≤ 0.05, ***P* ≤ 0.01, ****P* ≤ 0.001).

3.3.3 *Streptococcus pneumoniae* Internalization Assay

As the substrates fabricated in this study were shown to change macrophage morphology, we further evaluated their impact on phagocytosis. Specifically, we assessed the internalization of heat-killed TRITC-labeled *S. pneumoniae* by BMDMs on the flat and structured substrates. Fluorescence images (Figure 3.4A-C) were used to qualitatively assess the phagocytic function of macrophages, which revealed higher bacteria uptake on 2S and 50S compared with flat surfaces. This observation was verified by quantitative measurements (Figure 3.4D), where the relative fluorescence unit (RFU) value is proportional to the number of bacteria internalized by the cells on each substrate.

Macrophages on the structured SiO₂ substrates internalized more bacteria compared with those on flat surfaces. This difference was more pronounced when comparing 50F with 50S, suggesting that topography significantly alters phagocytic function, particularly on larger microstructures. Moreover, it was observed that plasma treatment did not significantly change phagocytic function in this experiment.

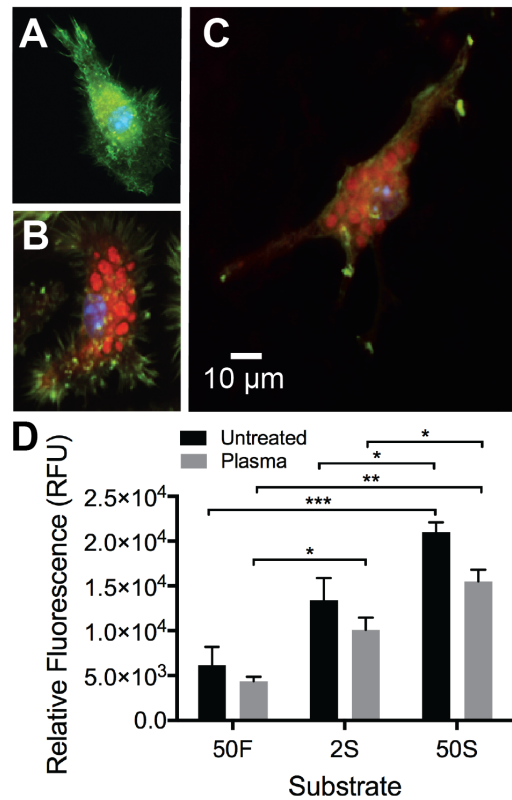


Figure 3.4 Phagocytosis of heat-killed, TRITC-labeled *S. pneumoniae* by BMDMs. Representative fluorescence images of BMDMs (green) and the internalized bacteria (red) on (A) 50 nm flat SiO₂ (50F), (B) 2 nm structured SiO₂ (2S), and (C) 50 nm structured SiO₂ (50S). (D) Relative fluorescence (RFU) values for BMDMs on plasma treated vs. untreated substrates. Bars represent the mean \pm SEM from $n = 3$ independently prepared samples. The RFU values have been normalized to the relative adhered cell density observed for each condition. Statistical analysis was done using one-way ANOVA with Tukey's post hoc test for comparison between substrates, and multiple t -tests between untreated and plasma-treated substrates with P value adjusted using Holm-Sidak correction method ($*P \leq 0.05$, $**P \leq 0.01$, $***P \leq 0.001$). The measured fluorescence is proportional to the amount of TRITC-labeled bacteria internalized. The scale bar is the same in A, B, and C.

3.3.4 IL-6 Cytokine Secretion

We next investigated whether substrates with micro- and nanostructured surfaces altered IL-6 cytokine secretion. Macrophages cultured on different substrates were stimulated with the TLR2 agonist Pam3Csk4, and the secretion of IL-6 was measured by ELISA. No significant difference in IL-6 secretion was observed for macrophages cultured on untreated substrates (Figure 3.5). In contrast, among plasma-treated surfaces, stimulation of cells on 50F resulted in significantly higher IL-6 secretion compared with plasma-treated 2S. Plasma-treatment also significantly decreased cytokine secretion by macrophages cultured on the 2S surfaces. In the absence of stimulation, IL-6 secretion was below the level of detection for all substrates.

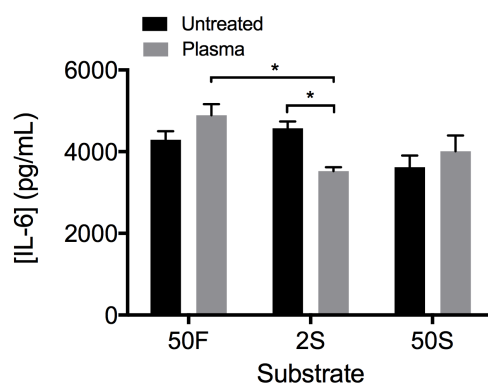


Figure 3.5 IL-6 secretion by BMDMs in response to stimulation with Pam3Csk4 on different substrates. Plasma treated vs. untreated comparison for substrates: 50 nm flat SiO₂ (50F), 2 nm structured SiO₂ (2S), and 50 nm structured SiO₂ (50S). Bars represent mean \pm SEM of $n = 3$ independently prepared samples. The IL-6 values have been normalized to the relative adhered cell density observed for each condition. Statistical analysis was done using one-way ANOVA with Tukey's post hoc test for comparison between substrates, and multiple *t*-tests between untreated and plasma-treated substrates with *P* values adjusted using Holm-Sidak correction method (* $P \leq 0.05$).

3.3.5 Membrane Diffusion – TLR2

We measured the lateral diffusion of TLR2 in the plasma membrane of macrophages using raster image correlation spectroscopy (RICS) to investigate whether surface topographies could impact membrane fluidity and receptor diffusion. The average TLR2 diffusion was higher in the apical membrane than the basal membrane for macrophages cultured on all substrate conditions (Supporting Information Figure S3.6). Among the six

substrate conditions, the average TLR2 diffusion was highest ($0.15 \pm 0.03 \mu\text{m}^2 \cdot \text{s}^{-1}$, mean \pm SD) on the apical membranes of macrophages on untreated 50F, and lowest on the basal membranes of cells on 2S ($0.10 \pm 0.04 \mu\text{m}^2 \cdot \text{s}^{-1}$). Figure 3.6 shows the comparison of TLR2 receptor diffusion for plasma membranes of cells on all structured substrates. Differences in TLR2 diffusion on the apical and basal membranes were determined by one-way ANOVA with 95% confidence interval. No significant difference was observed for the mean TLR2 diffusions obtained from apical ($F_{5,123}=1.547$, $P=0.18$) and basal ($F_{5,123}=1.887$, $P=0.101$) membranes on the six different substrate conditions.

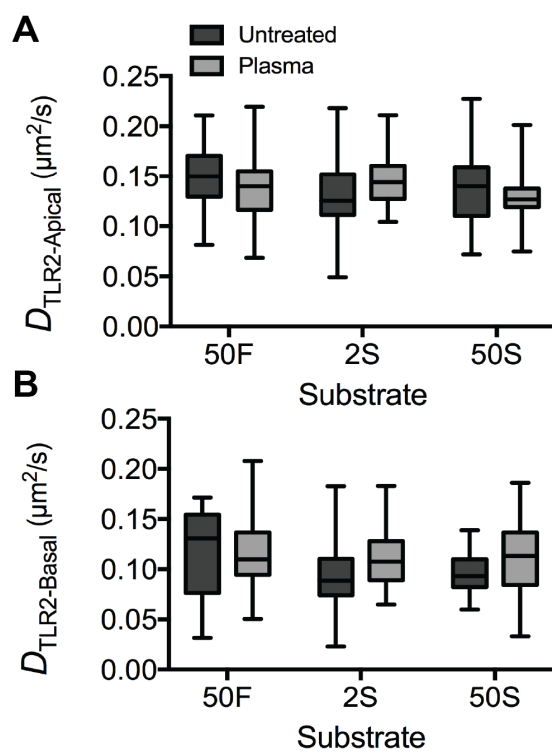


Figure 3.6 Lateral diffusion of TLR2 obtained from raster image correlation spectroscopy. (A) apical and (B) basal membranes of BMDMs cultured on different substrates. Plasma treated vs. untreated comparison for substrates: 50 nm flat SiO₂ (50F), 2 nm structured SiO₂ (2S), and 50 nm structured SiO₂ (50S). Data is from a minimum of 20 cells from at least 3 independent replicate experiments. Boxes show 25th-75th percentiles with whiskers extending to minimum and maximum values measured. Statistical analysis was done using one-way ANOVA with 95% confidence interval for apical and basal membranes in separate groups, which did not show any statistically significant differences.

3.4 Discussion

Despite differences in topographical features, materials used, and the source of macrophages, most studies report that macrophage shape is altered on structured surfaces [11,12,14,15]; however, the mechanisms by which surface topographies impact macrophage function are not yet fully understood. In this work, we investigated how surface topography and wettability alter macrophage shape, phagocytosis of *Streptococcus pneumoniae*, production of pro-inflammatory IL-6 cytokine, and TLR2 receptor mobility within the membrane.

The structured substrates fabricated in this study had significantly larger topographical features for 50 nm-thick sputtered SiO₂ film (50S) compared to the 2 nm-thick films (2S). This is in line with previous reports that have shown that the wrinkle size is dependent on the thickness and modulus of the deposited film [26,31], and follows from the wavelength of the buckling instability induced upon compression of a stack of films with mismatched elastic moduli [32,33]. We observed film cracking for 50S substrate that results from the low fracture toughness (0.8 ± 0.2 MPa m^{1/2}) [34] of the SiO₂ film. The roughness measurements obtained for film thicknesses > 50 nm showed a plateau for RMS roughness values, indicating that film fracture places an upper limit to the sizes of the topographical structures that this structuring method can produce. The WCA measurements for the 2S substrate are consistent with the Wenzel model [35], where the surface appeared homogeneously hydrophilic and water filled the voids between the wrinkles. In contrast, the 50S substrate with topographical features in the micron range followed the Cassie-Baxter model [36], where the surface appeared heterogeneous and air pockets filled the voids between the wrinkles such that water could not reach the whole surface, resulting in a higher contact angle [37]. The observed differences in wettability disappeared when the substrates were plasma oxidized, which rendered the surfaces superhydrophilic.

Macrophage morphology is typically quantified by measuring the long axis of the cell divided by the width across the nucleus, a ratio known as the “elongation factor” [10], [11,14]. Although this is instructive for measuring the elongation that occurs on unidirectional patterns, it is less useful for evaluating changes in membrane complexity such as those observed on random micro- and nanostructured surfaces, where, in

addition to changes in the overall shape and elongation of the cell, changes in the complexity of the cell boundary also occur (*cf.* Figure 3.2B). In contrast, fractal analysis can yield more information about cell geometry, beyond description of cell size and gross morphology [38]. To our knowledge, this is the first study on macrophage morphology that applies the fractal dimension to quantitatively assess morphological changes for the cell boundary and area.

Macrophages cultured on 50S substrates adopted a flattened star-shaped morphology, which was not observed on the flat and 2S surfaces and was independent of plasma treatment. These findings are consistent with previous studies that demonstrated morphological changes become more pronounced when the size of surface features reaches a certain scale. For example, it has been reported that macrophages are relatively insensitive to topographical features < 500 nm for substrates made of PCL, PLA, and PDMS [10], while macrophages adhered to polyethylene substrates presenting wrinkles with heights of a few microns do not display morphological changes compared with those on flat surfaces [14], although morphology was not quantified in these prior studies. In our work, macrophages did not align along or conform to the topographical features of 2S and 50S substrates, as previously observed for 3T3 fibroblasts in wrinkled polymer films [39], which was attributed to the relatively small spaces between surface features compared to the size of the cell bodies. There were no gross differences in macrophage morphology between the flat and 2S surfaces as seen in SEM images (Figure 3.2) and the FDA values (Figure 3.3A) that were not statistically different. However, we observed an increase in the number of filopodia, *i.e.*, finger-like membrane protrusions, which translated into higher FDP values (Figure 3.3B).

The increased phagocytic capacity of macrophages on the 2S and 50S substrates indicates that both micro- and nanostructured SiO₂ films impact macrophage function. Our findings are consistent with the general trend of increased phagocytosis reported for structured surfaces with parallel grooves. For example, P388D1 macrophages cultured on 2 and 10 μm fused silica microgrooves had more “microspikes” and phagocytosed more microbeads on the grooves than on plain surfaces [16]. Similarly, macrophages on GelMA hydrogel micropillars were found to phagocytose significantly less (~50%) zymosan particles than macrophages cultured on microgrooves/ridges, where the cells

adopted an elongated morphology [13]. In contrast, the macrophages on our 50S substrates did not develop elongated morphology or increased number of microspikes; yet their higher phagocytic capacity is evident as shown in Figure 3.4, suggesting that a different mechanism is at play for the enhanced phagocytosis. In our experiments, plasma treatment did not alter the phagocytic function of macrophages on flat, 2S, and 50S SiO₂ films. In contrast, it has been reported that human monocyte-derived macrophages cultured on flat hydrophilic O₂ plasma-etched polystyrene surfaces engulf significantly more zymosan particles compared with untreated polystyrene [18]. Whether these inconsistencies are due to differences in the species phagocytosed, the source of macrophages (bone marrow vs. monocyte-derived), substrate material, or methodological differences is not clear and could be the subject of further comparative studies.

Although the interaction of macrophages with the structured surfaces resulted in increased phagocytosis, it had no effect on the pro-inflammatory IL-6 secretion in the absence of stimulation. IL-6 secretion in response to Pam3Csk4 did not change for macrophages on untreated surfaces with different topographies, suggesting that topography of SiO₂ materials alone might not induce a pro-inflammatory response. In contrast, it has been reported that human monocyte-derived macrophages cultured on fibrous expanded polyfluoroethylene (PTFE) substrates, without additional stimulation, secrete pro-inflammatory cytokines, including the IL-6, that increases as the micron-scale distance between the PTFE fibers is increased [40]. While in our experiments IL-6 provides a first indication that flat and structured SiO₂ substrates do not induce a pro-inflammatory response, a full evaluation of the impact of these substrates on the overall inflammatory response of macrophages requires further investigation with a broader range of receptors and cytokines.

We hypothesized that since the incubation on structured surfaces led to significant changes in macrophage morphology and function, it could also lead to changes in transport within the plasma membrane. To test this hypothesis, lateral diffusion of TLR2 was measured quantitatively using RICS for macrophages on all substrate conditions. Our RICS measurements yielded diffusion coefficients of 0.12 ± 0.04 and 0.15 ± 0.03 $\mu\text{m}^2 \cdot \text{s}^{-1}$ for TLR2 receptors on the basal and apical membranes, respectively, of macrophages adhered to flat SiO₂ substrates. To our knowledge, there are no previous

reports of diffusion measurements of TLR2 on the plasma membrane of macrophages; however, these numbers are comparable to those reported for the diffusion coefficient measured by FRAP of TLR2 receptors in Chinese hamster ovary cells ($0.17 \pm 0.03 \mu\text{m}^2 \cdot \text{s}^{-1}$) [41]. In our experiments, the lower diffusion observed for the basal membrane is likely due to membrane-substrate interactions. Although significant differences in TLR2 lateral diffusion were observed between the apical and basal membranes on all surface conditions, there was no statistically significant difference in TLR2 diffusion in the basal membrane of macrophages attached to different substrates. Therefore, in spite of significant morphological changes in macrophages bound to the rougher surface topographies, no association was found between TLR2 diffusion and the surface conditions used, *i.e.*, structure size and plasma treatment. This finding suggests that the increased phagocytic ability shown by macrophages cultured on 2S and 50S substrates (Figure 3.4) does not correlate with any changes in IL-6 secretion or the membrane mobility as reported by TLR2 diffusion.

3.5 Conclusion

In summary, the present study shows that nano- and microstructured surfaces of SiO₂ alter the morphology of macrophages, by increasing filopodia generation or modifying the overall cell shape, and increase their phagocytic capacity. In contrast, these morphological changes do not alter the pro-inflammatory IL-6 cytokine secretion and the lateral diffusion of the transmembrane receptor TLR2; although plasma treatment changes cytokine secretion for some conditions. Further research is needed to identify the molecular mechanisms underlying the effect of surface treatment on IL-6 secretion. Understanding the biological outcome of this type of structured thin films with tunable interfacial properties can aid in the rational development of appropriate implant materials and interfaces, as well as in novel cell culture devices for the diagnosis of impaired phagocytic capacity in macrophages.

Supporting Information

Supporting Information is available from the Wiley Online Library or from the author.

3.6 References

- [1] S. Epelman, K. J. Lavine, and G. J. Randolph, “Origin and Functions of Tissue Macrophages,” *Immunity*, vol. 41, no. 1, pp. 21–35, 2014.
- [2] Z. Sheikh, P. J. Brooks, O. Barzilay, N. Fine, and M. Glogauer, “Macrophages, foreign body giant cells and their response to implantable biomaterials,” *Materials*, 2015.
- [3] C. Nich *et al.*, “Macrophages—Key cells in the response to wear debris from joint replacements,” *J. Biomed. Mater. Res. Part A*, vol. 101, no. 10, pp. 3033–3045, Oct. 2013.
- [4] W. Liu, M. Molnar, C. Garnham, H. Benav, and H. Rask-Andersen, “Macrophages in the human cochlea: saviors or predators—A study using super-resolution immunohistochemistry,” *Front. Immunol.*, vol. 9, Feb. 2018.
- [5] M. E. Ogle, C. E. Segar, S. Sridhar, and E. A. Botchwey, “Monocytes and macrophages in tissue repair: Implications for immunoregenerative biomaterial design,” *Exp. Biol. Med.*, vol. 241, no. 10, pp. 1084–1097, May 2016.
- [6] J. A. Champion and S. Mitragotri, “Role of target geometry in phagocytosis,” *Proc. Natl. Acad. Sci.*, vol. 103, no. 13, pp. 4930–4934, Mar. 2006.
- [7] H.-S. Lee, S. J. Stachelek, N. Tomczyk, M. J. Finley, R. J. Composto, and D. M. Eckmann, “Correlating macrophage morphology and cytokine production resulting from biomaterial contact,” *J. Biomed. Mater. Res. Part A*, vol. 101A, no. 1, pp. 203–212, Jan. 2013.
- [8] E. J. Vereyken, P. D. Heijnen, W. Baron, E. H. de Vries, C. D. Dijkstra, and C. E. Teunissen, “Classically and alternatively activated bone marrow derived macrophages differ in cytoskeletal functions and migration towards specific CNS cell types,” *J. Neuroinflammation*, vol. 8, no. 1, p. 58, 2011.
- [9] R. Sridharan, A. R. Cameron, D. J. Kelly, C. J. Kearney, and F. J. O’Brien, “Biomaterial based modulation of macrophage polarization: A review and suggested design principles,” *Mater. Today*, vol. 18, no. 6, pp. 313–325, 2015.
- [10] S. Chen, J. A. Jones, Y. Xu, H.-Y. Low, J. M. Anderson, and K. W. Leong, “Characterization of topographical effects on macrophage behavior in a foreign body response model,” *Biomaterials*, vol. 31, no. 13, pp. 3479–3491, May 2010.

- [11] T. U. Luu, S. C. Gott, B. W. K. Woo, M. P. Rao, and W. F. Liu, “Micro- and nanopatterned topographical cues for regulating macrophage cell shape and phenotype,” *ACS Appl. Mater. Interfaces*, vol. 7, no. 51, pp. 28665–28672, 2015.
- [12] F. Y. Mcwhorter, T. Wang, P. Nguyen, T. Chung, and W. F. Liu, “Modulation of macrophage phenotype by cell shape.,” *Proc. Natl. Acad. Sci. U. S. A.*, vol. 110, no. 43, pp. 17253–8, 2013.
- [13] S. Singh *et al.*, “Unbiased analysis of the impact of micropatterned biomaterials on macrophage behavior provides insights beyond predefined polarization states,” *ACS Biomater. Sci. Eng.*, vol. 3, no. 6, pp. 969–978, 2017.
- [14] T. Wang, T. U. Luu, A. Chen, M. Khine, and W. F. Liu, “Topographical modulation of macrophage phenotype by shrink-film multi-scale wrinkles,” *Biomater. Sci.*, vol. 4, pp. 0–4, 2016.
- [15] V. Malheiro, F. Lehner, V. Dinca, P. Hoffmann, and K. Maniura-Weber, “Convex and concave micro-structured silicone controls the shape, but not the polarization state of human macrophages,” *Biomater. Sci.*, vol. 4, no. 11, pp. 1562–1573, 2016.
- [16] B. Wójciak-Stothard, A. Curtis, W. Monaghan, K. MacDonald, and C. Wilkinson, “Guidance and activation of murine macrophages by nanometric scale topography.,” *Exp. Cell Res.*, vol. 223, no. 223, pp. 426–435, 1996.
- [17] K. M. Hotchkiss, G. B. Reddy, S. L. Hyzy, Z. Schwartz, B. D. Boyan, and R. Olivares-Navarrete, “Titanium surface characteristics, including topography and wettability, alter macrophage activation,” *Acta Biomater.*, vol. 31, pp. 425–434, 2016.
- [18] H. M. Rostam *et al.*, “The impact of surface chemistry modification on macrophage polarisation,” *Immunobiology*, vol. 221, no. 11, pp. 1237–1246, 2016.
- [19] J. M. Brodbeck, W. G., Nakayama, Y., Matsuda, T., Colton, E., Ziats, N. P., & Anderson, “material surface chemistry dictates adherent monocyte/macrophage cytokine expression in vitro. Cytokine,” *JM. Bio*, vol. 18, no. 6, pp. 311–9, 2002.
- [20] S. Lee *et al.*, “Analysis on migration and activation of live macrophages on transparent flat and nanostructured titanium,” *Acta Biomater.*, vol. 7, no. 5, pp. 2337–2344, 2011.

- [21] C. Christian, G. Moura, D. Zanetta-barbosa, and P. Dechichi, “Effects of titanium surfaces on the developmental profile of monocytes / macrophages,” vol. 25, pp. 96–103, 2014.
- [22] N. E. Paul *et al.*, “Topographical control of human macrophages by a regularly microstructured polyvinylidene fluoride surface,” *Biomaterials*, vol. 29, no. 30, pp. 4056–4064, 2008.
- [23] M. Bartneck, V. A. Schulte, N. E. Paul, M. Diez, M. C. Lensen, and G. Zwadlo-Klarwasser, “Induction of specific macrophage subtypes by defined micro-patterned structures,” *Acta Biomater.*, vol. 6, no. 10, pp. 3864–3872, 2010.
- [24] D. Ke, S. F. Robertson, W. S. Dernell, A. Bandyopadhyay, and S. Bose, “Effects of MgO and SiO₂ on plasma-sprayed hydroxyapatite coating: an in vivo study in rat distal femoral defects,” *ACS Appl. Mater. Interfaces*, vol. 9, no. 31, pp. 25731–25737, Aug. 2017.
- [25] W. Walke *et al.*, “Evaluation of physicochemical properties of SiO₂-coated stainless steel after sterilization,” *Mater. Sci. Eng. C*, vol. 63, pp. 155–163, Jun. 2016.
- [26] C. M. Gabardo, Y. Zhu, L. Soleymani, and J. M. Moran-Mirabal, “Bench-top fabrication of hierarchically structured high-surface-area electrodes,” *Adv. Funct. Mater.*, vol. 23, no. 24, pp. 3030–3039, 2013.
- [27] J. Q. Davies, & S. Gordon, “Isolation and culture of murine macrophages.,” *Methods Mol. Biol.*, vol. 290, pp. 91–103, 2005.
- [28] J. Weischenfeldt, & B. Porse, “Bone marrow-derived macrophages (BMM): isolation and applications.,” *CSH Protoc.*, vol. 3, pp. 1–7, 2008.
- [29] J. M. Moran-Mirabal, D. M. Aubrecht, and H. G. Craighead, “Phase separation and fractal domain formation in phospholipid/diacetylene-supported lipid bilayers,” *Langmuir*, vol. 23, no. 21, pp. 10661–10671, Oct. 2007.
- [30] M. J. Rossow, J. M. Sasaki, M. A. Digman, and E. Gratton, “Raster image correlation spectroscopy in live cells.,” *Nat. Protoc.*, vol. 5, no. 11, pp. 1761–1774, 2010.
- [31] U. Gill *et al.*, “Beyond buckling: humidity-independent measurement of the mechanical properties of green nanobiocomposite films,” *Nanoscale*, vol. 9, no. 23, pp. 7781–7790, 2017.

- [32] J. Groenewold, "Wrinkling of plates coupled with soft elastic media," *Phys. A Stat. Mech. its Appl.*, vol. 298, no. 1–2, pp. 32–45, Sep. 2001.
- [33] C. M. Stafford *et al.*, "A buckling-based metrology for measuring the elastic moduli of polymeric thin films," *Nat. Mater.*, vol. 3, no. 8, pp. 545–550, Aug. 2004.
- [34] V. Hatty, H. Kahn, and A. H. Heuer, "Fracture toughness, fracture strength, and stress corrosion cracking of silicon dioxide thin films," *J. Microelectromechanical Syst.*, vol. 17, no. 4, pp. 943–947, Aug. 2008.
- [35] R. N. Wenzel, "Resistance of solid surfaces to wetting by water," *Ind. Eng. Chem.*, vol. 28, no. 8, pp. 988–994, Aug. 1936.
- [36] A. B. D. Cassie and S. Baxter, "Wettability of porous surfaces," *Trans. Faraday Soc.*, vol. 40, p. 546, 1944.
- [37] A. Shahraz, A. Borhan, and K. A. Fichthorn, "A theory for the morphological dependence of wetting on a physically patterned solid surface," *Langmuir*, vol. 28, no. 40, pp. 14227–14237, Oct. 2012.
- [38] K. M. Keough, P. Hyam, D. A. Pink, and B. Quinn, "Cell surfaces and fractal dimensions," *J. Microsc.*, vol. 163, no. Pt 1, pp. 95–9, Jul. 1991.
- [39] C. Zhou, J. Zhao, S. Saem, U. Gill, H. D. H. Stöver, and J. Moran-Mirabal, "Self-cross-linking p(APM- co -AA) microstructured thin films as biomimetic scaffolds," *ACS Appl. Bio Mater.*, vol. 1, no. 5, pp. 1512–1522, Nov. 2018.
- [40] P. C. S. Bota *et al.*, "Biomaterial topography alters healing in vivo and monocyte/macrophage activation in vitro," *J. Biomed. Mater. Res. Part A*, vol. 95A, no. 2, pp. 649–657, Aug. 2010.
- [41] M. Triantafilou, S. Morath, A. Mackie, T. Hartung, and K. Triantafilou, "Lateral diffusion of Toll-like receptors reveals that they are transiently confined within lipid rafts on the plasma membrane," *J Cell Sci*, vol. 117, no. Pt 17, pp. 4007–4014, 2004.

Chapter 4

Age-Related Changes in Macrophages

The prevalence of chronic illnesses increases with age and elderly are more susceptible to infectious diseases due to impaired immune system. To date, several age-related changes in the innate immune cells have been identified; however, the reported data related to changes in macrophage phenotypes are inconclusive.

This chapter presents a preliminary comparison of macrophages derived from the bone marrow of young and old mice, with focus on their phagocytic capacity to internalize the bacteria *Streptococcus pneumoniae* and the lateral diffusion of TLR2 in the apical plasma membrane.

4.1 Introduction

The innate and adaptive immune systems decline with age, leading to increased susceptibility to infections and inflammatory diseases [1,2,3]. Age-related changes in innate immunity include variations in the number of specific leukocytes present in circulation, receptor expression and signaling pathways, cytokine production, and phagocytic function, among others [4]. Studies on macrophage function in age-related inflammatory diseases have revealed impaired phagocytosis in older individuals [5], as well as reduced chemotaxis, reduced expression of MHC class II, lower capacity for antigen presentation [6,7], higher production of reactive oxygen species [8], and alterations in M1/M2 activation and polarization [9] that are associated with aging. Furthermore, previous investigations in aged mice have revealed an increase in the number of bone marrow-derived macrophages that have impaired ability to produce or release cytokines, suggesting that higher number of macrophages may compensate for their reduced function [10].

Macrophages are professional phagocytes and their phagocytic function is central to the clearance of apoptotic cells and invading pathogens. Reports on age-associated changes in macrophage function indicate reduced phagocytic capacity in macrophages of different tissue origins. Peritoneal macrophages [11], alveolar macrophages [12], Kupffer cells (specialized liver macrophages) [13], and microglia (specialized macrophages in the central nervous system) [14], all exhibit an age-related decline in phagocytosis. However, comparison of young and old bone marrow-derived macrophages (BMDMs) have shown inconsistent results with regard to their phagocytic capacity. While there are reports that BMDMs derived from old mice take up fewer apoptotic granulocytes [15], others have shown no age-related changes [16]. However, it is unclear if these inconsistencies are due to differences in the type of particles phagocytosed by macrophages or in the experimental methodologies applied.

Macrophages express transmembrane toll-like receptors (TLRs), which bind bacterial products and initiate inflammatory responses. TLR2, for example, binds the anchor motif of bacterial lipoproteins found on the surface of bacteria, and responds to lipid-containing pathogen associated molecular patterns (PAMPs) such as lipoteichoic acid (LTA) from Gram-positive bacteria [17]. Changes in TLR signaling not only

increase susceptibility to infections but can also trigger other conditions such as atherosclerosis and autoimmune diseases [18]. Although the existing reports on TLR changes are not conclusive, most investigations have shown TLR2-mediated pro-inflammatory signaling pathways in macrophages are impaired with age, while cell-surface expression of this receptor is not changed [19].

Deficiencies in TLR function contribute to susceptibility to infectious diseases in the elderly [20], as in the case of infection caused by *Streptococcus pneumoniae* (the pneumococcus) [21]. Pneumococcal cell wall and the toxin pneumolysin cause inflammation by binding to TLR1/TLR2 [22] and TLR4 [23] on the macrophage cell surface, respectively, which in turn initiates a cell-signaling cascade that activates the transcription nuclear factor kappa B. (NF- κ B). NF- κ B is a major regulator of innate immunity, and its activation results in the transcription of pro-inflammatory cytokines. However, the mechanisms leading to age-associated dysregulation in TLR2 signaling have yet to be elucidated.

The aim of this chapter is to compare the phagocytic capacity and TLR2 diffusion in macrophages derived from young and aged mice. We have assessed the internalization capacity of macrophages using polystyrene microspheres and *S. pneumoniae*. We have also investigated whether TLR2 diffusion is different in the plasma membrane of macrophages from young and old groups, both in their resting state and after stimulation with *S. pneumoniae*.

Considering the essential role of macrophages in innate immunity, identifying the age-related changes that appear in macrophages can help in the rational development of effective therapeutic strategies to fight infections.

4.2 Experimental Section

4.2.1 Macrophage Culture

Bone marrow progenitors from 5 young (10-14 wk) and 5 old (19-22 months) C57BL/6 male mice (The Jackson Laboratory, Maine, USA) were isolated from spines according to previously published methods [24]. Progenitor cells were cultured for 7 days in RPMI-1640 supplemented with 10% fetal bovine serum (FBS), 1% L-glutamine, 1% penicillin/streptomycin, and 15% L929 fibroblast cell conditioned medium on 150 mm

Petri dishes (Fisherbrand, Fisher Scientific, Pittsburgh, PA) per standard protocols [24,25]. Differentiated macrophages were incubated with Accutase for 5 minutes and gently lifted using a cell lifter. Cells were counted and pooled from 5 mice (20% contribution from each mouse) for each young and old group. Cells were plated 24 hrs before imaging, at a density of 100,000 per Glass Bottom Microwell dishes (35 mm dish, 20 mm Microwell, No. 1.5 coverglass, 0.16-0.19 mm thickness, MatTek, Ashland, MA). All animal manipulations were done according to protocols approved by McMaster's Animal Research Ethics Board.

4.2.2 Polystyrene Beads/Bacterial Internalization Assay

Fluorescently conjugated polystyrene beads (Fluoresbrite® YG Microspheres 0.50 µm, Polysciences Inc., Warrington, PA), and *S. pneumoniae* strain P1547 (clinical isolate, serotype 6A, provided by Dr. Jeff. N. Weiser, New York University, NY, USA) were used in separate experiments for the internalization assay. The *S. pneumoniae* culture ($OD_{600} = 0.5$) was heated for 10 min at 65°C to kill the bacteria, which was then digested with lysozyme and labeled using 20 ng/mL of TRITC (Invitrogen, Burlington, ON, Canada) for 30 min at 37°C. The fluorescent bacteria or polystyrene beads were then incubated with macrophages in suspension on a nutator mixer for 1.5 hr at 37°C with a multiplicity of infection (MOI) of 320 beads per cell or 50 bacteria per cell, in separate experiments with three replicates for each of the young and old groups. The samples were subsequently washed 3× with PBS and centrifugation. The internalized beads and bacteria were then measured on a SpectraMax i3 plate reader (Molecular Devices, San Jose, CA, USA) at 555 nm excitation and 580 nm emission wavelengths for detection of bacteria, and 441 nm excitation and 486 nm emission wavelengths for beads. Relative fluorescence values (RFU) were corrected for autofluorescence and nonspecific adsorption. Macrophages from young and old mice were then seeded on separate MatTek imaging dishes, incubated at 37°C for 1 hr, and finally fixed with 2% paraformaldehyde for 15 min at room temperature. The fixed cells were stored in PBS at 4°C until staining and imaging.

4.2.3 Cell Staining and Counting

For staining, the cell membrane was permeabilized using a 0.2% v/v Triton-X solution (Sigma Aldrich, Oakville, ON, Canada), according to the dye manufacturers' directions. The cell nuclei for all samples were stained with a 600 nM solution of 4,6-diamidino-2-phenylindole dihydrochloride (DAPI, Invitrogen, Burlington, ON, Canada). The cells with internalized polystyrene microspheres were stained with Zombie Red™ (BioLegend, excitation: 600 nm, emission: 624 nm) added at 1:1000 dilution for 30 min and subsequently washed 3× with PBS. The fluorescent samples were then imaged in PBS with a Nikon Eclipse LV100N POL epifluorescence microscope (Nikon Instruments, Mississauga, ON, Canada) equipped with a 60×/0.9NA physiological objective and a Retiga 2000R camera (QImaging, Surrey, BC, Canada). Fluorescence images were captured using NIS Elements software (Nikon Instruments, Mississauga, ON, Canada) to quantify the number of internalized microspheres and bacteria within each cell for 600 macrophages from young and old mice (three replicates, 200 cells per dish).

4.2.4 Diffusion Measurements

All staining and imaging were performed in RPMI-1640 Medium, without phenol red (Life Technologies- Gibco™). TLR2 was labeled using mouse anti-TLR2/CD282 antibody conjugated with Alexa Fluor 647 using 1:1000 dilution of the monoclonal antibody (0.2 mg/mL stock concentration) in the imaging media. Antibody staining was performed at 4°C for 1 hr to prevent receptor internalization, after which the samples were washed 3× with PBS and the media was replaced with RPMI containing 5 mM ascorbic acid to minimize photobleaching during imaging. To investigate the impact of stimulation with bacteria, heat-killed *S. pneumoniae* were labeled with rabbit anti-*Streptococcus pneumoniae* (4 mg/mL IgG stock concentration, dilution 1:1500) conjugated with FITC (AbD Serotec, Hercules, CA, USA). FITC-labeled bacteria were added to the imaging dish at a MOI of 50 per cell together with TLR2 antibody and were incubated with macrophages in suspension on a nutator mixer for 1 hr at 4°C. The samples were subsequently washed 3× with PBS and live cell imaging was performed immediately after at 37°C using a stage top incubator (TOKAI HIT, INUBG2ATW-TIZW).

Raster-scan images were collected using confocal laser-scanning microscopy (CLSM, Nikon Microscope ECLIPSE LV100ND) on an inverted microscope fitted with a 60x/1.40NA Plan Apo λ oil-immersion objective. Excitation was from 647-nm laser line attenuated to 0.30-0.70% of the nominal laser power (20 mW). A pinhole size of 1.2 AU (47.3 μm) was chosen for imaging. The apical membrane was found by focusing on the highest observable plane through the cell.

For raster image correlation spectroscopy (RICS), 256 \times 256-pixel images were collected using NIS imaging software (NIS-Elements AR 4.30.02) at 16.66x zoom, corresponding to a pixel size of 50 nm. The pixel dwell time was set to 23.8 μs /pixel, and the line time to 7.858 ms for raster-scanning live cells. Stacks of 50 images were captured with no delay between frames.

Diffusion data were extracted from the images using SimFCS software (Laboratory of Fluorescence Dynamics, University of California, Irvine) [26]. Regions of interest were selected with frame sizes of 64 \times 64 pixels (3.2 \times 3.2 μm^2) for each cell. Diffusion was measured using the known parameters of pixel dwell time, line time, size of each pixel, and the beam waist. For each stack of images, the RICS function was calculated as the average of all images of the stack. Data were obtained from 60 cells for each of the young and old groups (120 cells in total) for unstimulated condition and 30 cells for each group (60 cells in total) for the stimulated state. A minimum of three replicate samples per condition was used.

4.2.5 Statistical Analysis

Statistical analysis and plotting were performed using SPSS software (IBM SPSS Statistics 21) and Prism 7.0a (GraphPad Software Inc.), respectively. Differences were considered statistically significant at $P < 0.05$.

4.3 Results

4.3.1 Internalization Assay

We assessed the internalization of fluorescently conjugated polystyrene beads (0.5 μm in diameter) and heat-killed TRITC-labeled *S. pneumoniae* by young and old BMDMs in separate experiments. Figure 4.1A-B shows the relative fluorescence (RFU)

measurements, which are proportional to the number of beads or bacteria internalized by the cells within each group. The relative fluorescence revealed no significant difference between young and old macrophages with regard to internalization of beads ($P=0.082$) and bacteria ($P=0.194$). This observation was verified by fluorescence images (Figure 4.1C-F) that were used for quantification of the number of beads and bacteria taken up by individual cells for 600 young and 600 old murine BMDMs in three replicate samples (200 cells per imaging dish). No significant difference was observed between young and old groups with regard to the average number of beads (young: 21 ± 24 ; old: 18 ± 28) and bacteria (young: 8 ± 6 ; old: 9 ± 7) that were internalized. However, macrophages derived from old mice had more variation in their phagocytic capacity. While more than 50% of old macrophages contained < 20 beads, we found higher number of macrophages in the old than young group with over 100 beads inside the cell bodies (Figure 4.1G-H).

4.3.2 TLR2 Diffusion

The lateral diffusion of TLR2 in the plasma membrane of macrophages derived from young and old mice was measured using raster image correlation spectroscopy (RICS) to investigate whether aging impacts receptor diffusion. Diffusion was compared between young and old groups in the absence of any stimulation and after stimulation with *S. pneumoniae*. Diffusion was measured in the apical membranes rather than basal membranes, based on our previous findings on RAW 264.7 macrophage cell line (Chapter 2, Section 2.3.2) and primary macrophages cultured on SiO₂ surface topographies (Chapter 3, Section 3.3.5). Figure 4.2A-B shows the TLR2 visualized on the apical membrane (red) and the FITC-labeled bacteria (green) inside the same macrophage cell from young group. Diffusion coefficients were averaged from at least three ROIs in the apical membranes (Figure 4.2C-E). As shown in Figure 4.3, the average TLR2 diffusion was comparable in macrophages derived from young ($0.20 \pm 0.03 \mu\text{m}^2\text{s}^{-1}$, mean \pm SD) and old ($0.19 \pm 0.04 \mu\text{m}^2\text{s}^{-1}$) mice. In macrophages stimulated with *S. pneumoniae* the diffusion of TLR2 was significantly faster both in young ($0.23 \pm 0.05 \mu\text{m}^2\text{s}^{-1}$) and old ($0.26 \pm 0.04 \mu\text{m}^2\text{s}^{-1}$) groups compared with unstimulated resting state. However, no significant difference was observed between the young and old groups.

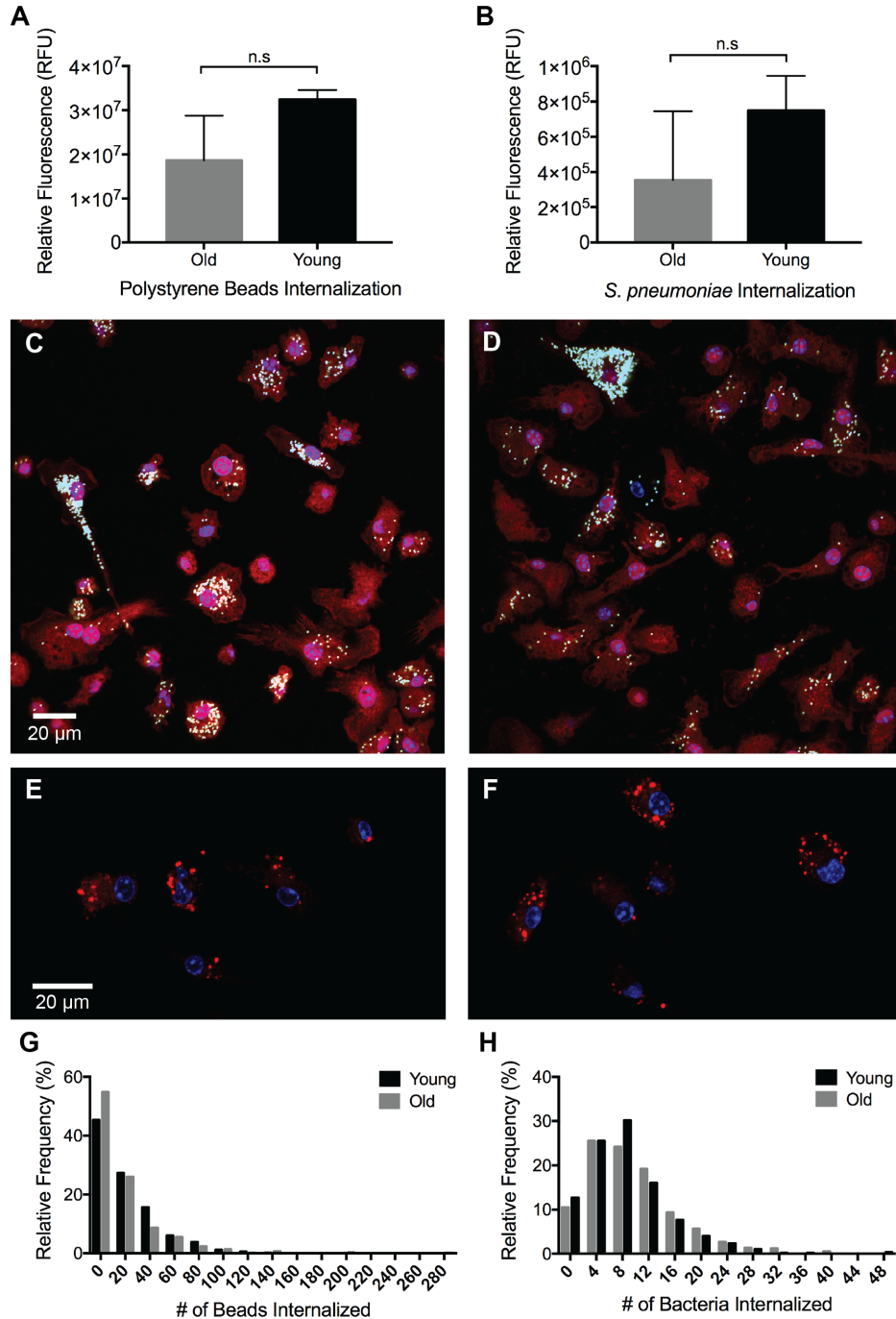


Figure 4.1 Internalization of polystyrene microspheres and bacteria by young and old BMDMs. Relative fluorescence (RFU) values measured for beads (A) and *S. pneumoniae* bacteria (B) internalized by young and old BMDMs. Bars represent the mean \pm SD from $n = 3$ independently prepared samples. Representative fluorescence images of young (C,E) and old (D,F) BMDM cells (red) with internalized beads (yellow) and heat-killed TRITC-labeled *S. pneumoniae* (red), respectively. Relative frequency of the number of internalized beads (G) and *S. pneumoniae* (H) found within individual macrophages; $n = 600$ cells were evaluated for each of the young and old groups from three replicate samples (200 cells per dish). Statistical analysis was performed using independent samples *t*-test; n.s. = no significance. The scale bar is the same in C-D, and in E-F.

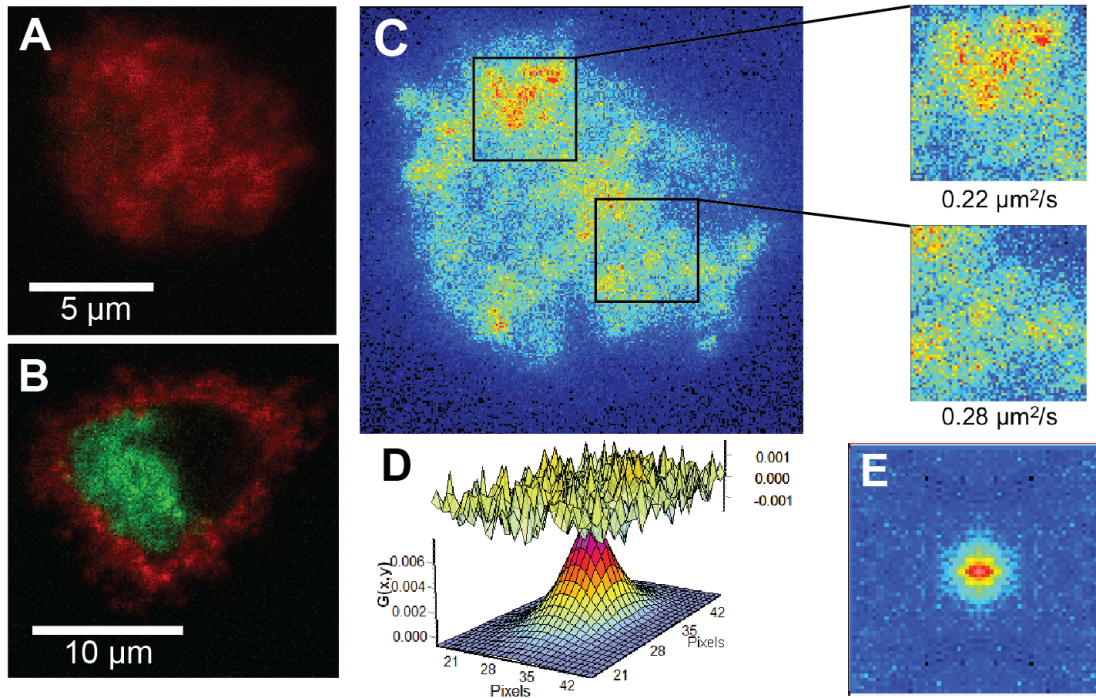


Figure 4.2 Lateral diffusion of TLR2 in BMDM plasma membrane obtained from raster image correlation spectroscopy. (A) TLR2 (red) visualized in the apical membrane of a macrophage. (B) TLR2 (red) and FITC-labeled *S. pneumoniae* (green) in a cross section image of the cell in (A). (C) TLR2 diffusion coefficient measured in the apical membrane shown in (A) with two ROIs of 64×64 frames ($3.2 \times 3.2 \mu\text{m}^2$). (D) Plot of the residues (upper surface) and the fit (lower surface). (E) 2D autocorrelation function from RICS.

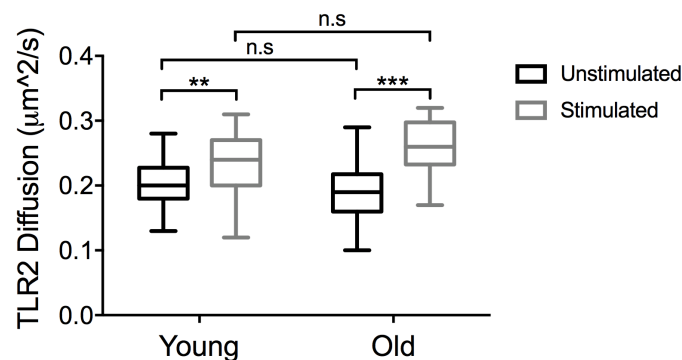


Figure 4.3 TLR2 diffusion coefficients obtained from RICS in the apical membrane of BMDMs from young and old mice. Measurements are from a minimum of three separate ROIs per cell, for 60 macrophages in each of the young and aged groups (unstimulated) and 30 macrophages per age group (stimulated with *S. pneumoniae*). Boxes show 25th–75th percentiles with whiskers extending to minimum and maximum values measured. Statistical analysis was performed using two-way ANOVA with 95% confidence interval (n.s = not statistically significant, ** $P \leq 0.01$, *** $P \leq 0.001$).

4.4 Discussion

The pathogenesis and establishment of *S. pneumoniae* infection is accompanied by phagocytosis of the bacteria by macrophages and neutrophils and initiation of the pro-inflammatory response that is mediated primarily by TLRs [27,28]. Therefore, understanding these two complex events can help uncover the age-associated susceptibility to *S. pneumoniae* infection. In this work, we investigated whether the phagocytic ability of BMDMs as well as the diffusion of plasma membrane TLR2 differ in aged versus young mice.

The phagocytosis assays did not reveal any significant difference in the internalization capacity of macrophages derived from young and old mice. However, the variation in the number of beads per cell was higher in macrophages from old mice. While 55% of macrophages from aged mice contained 20 or fewer beads (compared to 45% in young group), there was a small percentage (~3%) that internalized > 100 beads in the old group. In a similar study by Linehan *et al.* on BMDMs, no significant difference was observed in the amount of polystyrene beads phagocytosed by macrophages from young and old mice [29]. In contrast, phagocytosis of apoptotic Jurkat T cells by BMDMs was reported to be significantly lower in macrophages derived from old than young mice [30]. This inconsistency could be due to engagement of different group of receptors in the internalization of cells versus non-biological particles. While class A scavenger receptors including macrophage receptor with collagenous structure (MARCO) recognizes polystyrene nanoparticles [31], the recognition and uptake of apoptotic cells are carried out via a different repertoire of phagocytic receptors such as lectins and integrins, as well as other types of class A and class B scavenger receptors [32]. In contrast to BMDMs, comparative studies on tissue-resident macrophages of young and old mice have shown more consistent declining trend in their phagocytic capacity due to aging. Our group has previously shown that age-associated changes in tissue microenvironments contribute to alterations in phenotype for macrophages of multiple tissue origins [33,34]. Although there is evidence from other *in vivo* experiments that age-related changes in tissue specific microenvironments can impact macrophage function [29], the details of whether extrinsic factors in tissues or cell-intrinsic mechanisms contribute to reduced capacity for phagocytosis in macrophages is still not clearly understood.

The mobility of a number of plasma membrane receptors on macrophages has been studied, including the phagocytic receptor Fc γ [35–38], scavenger receptor CD36 [39], protein tyrosine phosphatases CD45 [40], adhesion molecule CD44 [38], and CD14 as a coreceptor of TLRs [41]. Measuring the diffusion of these receptors has provided valuable insights into the complex mechanisms of receptor-ligand binding, clustering and interaction of multiple receptors, and the role of cytoskeleton and lipid rafts in receptor diffusion and downstream signaling pathways; however, the diffusion of membrane receptors has not been investigated in the context of aging. Our TLR2 diffusion measurements in macrophages from aged mice did not reveal any significant difference compared with their young counterparts. Stimulation with *S. pneumoniae* resulted in significantly faster diffusion of TLR2, which was similar in both young and old groups. While these preliminary results can provide information on how diffusion of TLR2 changes in the context of infection with *S. pneumoniae*, a more complete understanding of changes in TLR2 mobility and signaling requires time-sensitive examinations of receptor diffusion at the site of binding in the plasma membrane and at the onset of bacteria internalization. It should be taken into account that our TLR2 diffusion measurements in the apical membrane were obtained after bacteria were internalized by macrophages. To facilitate diffusion measurements during binding, the stimulated cells need to be incubated at 4°C for delayed internalization of bacteria until imaging is performed. Furthermore, comparison of TLR2 surface expression and the pro-inflammatory cytokine secretions including IL-6 in response to stimulation can help to identify age-related changes in TLR2 signaling.

4.5 Conclusion

In summary, the present study provides preliminary results to identify potential age-related changes in bone marrow-derived macrophages from young and aged mice. No significant difference was observed in macrophages of the two age groups with regard to phagocytosis of polystyrene beads and the bacteria *S. pneumoniae*. Similarly, the diffusion rate of TLR2 was comparable in the two age groups, and was significantly faster during stimulation with *S. pneumoniae*.

4.6 References

- [1] N. P. Weng, “Aging of the immune system: how much can the adaptive immune system adapt?,” *Immunity*, vol. 24, pp. 495–499, 2006.
- [2] C. R. Gomez, E. D. Boehmer, and E. Kovacs, “The aging innate immune system,” *Curr. Opin. Immunol.*, vol. 17, pp. 457–462, 2005.
- [3] L. Ginaldi, M. F. Loreto, M. P. Corsi, M. Modesti, and M. De Martinis, “Immunosenescence and infectious diseases,” *Microbes. Infect.*, vol. 3, pp. 851–857, 2001.
- [4] S. Rafael, T. Raquel, G. Inmaculada, L. Olivier, D. Gilles, and F. Tamas, “Innate immunosenescence: Effect of aging on cells and receptors of the innate immune system in humans,” *Semin. Immunol.*, vol. 24, pp. 331–341, 2012.
- [5] A. Hearps *et al.*, “Aging is associated with chronic innate immune activation and dysregulation of monocyte phenotype and function. Aging Cell,” *Aging Cell*, vol. 11, pp. 867–875, 2012.
- [6] C. Herrero, L. Marques, J. Lloberas, and A. Celada, “IFN-gamma-dependent transcription of MHC class II IA is impaired in macrophages from aged mice,” *J. Clin. Invest.*, vol. 107, pp. 485–93, 2001.
- [7] J. Villanueva, R. Solana, M. Alonso, and J. Pena, “Changes in the expression of HLA-class II antigens on peripheral blood monocytes from aged humans,” *Dis. Markers*, vol. 8, pp. 85–91, 1990.
- [8] C. Vida, I. M. de Toda, J. Cruces, A. Garrido, M. Gonzalez-Sanchez, and M. De la Fuente, “Role of macrophages in age-related oxidative stress and lipofuscin accumulation in mice,” *Redox Biol.*, vol. 12, pp. 423–437, 2017.
- [9] S. Mahbub, C. Deburghgraeve, and E. Kovacs, “Advanced age impairs macrophage polarization,” *J. Interf. Cytokine Res*, vol. 32, pp. 18–26, 2012.
- [10] C. Wang, K. Udupa, H. Xiao, and D. Lipschitz, “Effect of age on marrow macrophage number and function.,” *Ageing*, vol. 7, pp. 379–84, 1995.
- [11] V. Khare, A. Sodhi, and S. Singh, “Effect of aging on the tumoricidal functions of murine peritoneal macrophages,” *Nat. Immunol.*, vol. 15, p. 285–294., 1996.
- [12] Z. Li *et al.*, “Aging-Impaired Filamentous Actin Polymerization Signaling Reduces

- Alveolar Macrophage Phagocytosis of Bacteria,” *J Immunol*, vol. 199, pp. 3176–3186, 2017.
- [13] L. Videla, G. Tapia, and V. Fernandez, “Influence of aging on Kupffer cell respiratory activity in relation to particle phagocytosis and oxidative stress parameters in mouse liver.,” *Redox Rep.*, vol. 6, pp. 155–159, 2001.
- [14] C. Bliederhaeuser *et al.*, “Age-dependent defects of alpha-synuclein oligomer uptake in microglia and monocytes,” *Acta Neuropathol*, vol. 131, pp. 379–391, 2016.
- [15] H. . Arnardottir, J. Dalli, R. . Colas, M. Shinohara, and C. . Serhan, “Aging delays resolution of acute inflammation in mice: reprogramming the host response with novel nano-proresolving medicines,” *J Immunol*, vol. 193, pp. 4235–4244, 2014.
- [16] D. J. M. Albright, M. R. C. Dunn, D. J. A. Shults, M. D. M. Boe, D. M. Afshar, and D. E. Kovacs, “Advanced age alters monocyte and macrophage responses,” *Antioxid. Redox Signal.*, vol. 25, no. 15, pp. 805–815, 2016.
- [17] S. Akira and S. Uematsu, “Toll-like receptors (TLRs) and Their Ligands,” *Toll-Like Recept. Innate Immun.*, pp. 6–8, 2007.
- [18] D. N. Cook, D. S. Pisetsky, and D. A. Schwartz, “Toll-like receptors in the pathogenesis of human disease,” *Nat. Immunol.*, vol. 5, pp. 975–979, 2004.
- [19] E. D. Boehmer, M. J. Meehan, B. T. Cutro, and E. J. Kovacs, “Aging negatively skews macrophage TLR2- and TLR4-mediated pro-inflammatory responses without affecting the IL-2-stimulated pathway,” *Mech. Ageing Dev.*, vol. 126, no. 12, pp. 1305–1313, 2005.
- [20] C. R. Dunston and H. R. Griffiths, “The effect of ageing on macrophage Toll-like receptor-mediated responses in the fight against pathogens,” *Clin. Exp. Immunol.*, vol. 161, pp. 407–416, 2010.
- [21] E. Hinojosa, A. R. Boyd, and C. J. Orihuela, “Age-Associated Inflammation and Toll-Like Receptor Dysfunction Prime the Lungs for Pneumococcal Pneumonia,” *J. Infect. Dis.*, vol. 200, pp. 546–554, 2009.
- [22] J. Weber *et al.*, “Recognition of pneumococcal peptidoglycan: an expanded, pivotal role for LPS binding protein,” *Immunity*, vol. 19, pp. 269–279, 2003.
- [23] R. Malley *et al.*, “Recognition of pneumolysin by Toll-like receptor 4 confers resistance to pneumococcal infection,” *Proc Natl Acad Sci USA*, vol. 100, pp. 1966–

- 1971, 2003.
- [24] J.Q. Davies, and S. Gordon, “Isolation and culture of murine macrophages.,” *Methods Mol. Biol.*, vol. 290, pp. 91–103, 2005.
- [25] J. Weischenfeldt, and B. Porse, “Bone marrow-derived macrophages (BMM): isolation and applications.,” *CSH Protoc.*, vol. 3, pp. 1–7, 2008.
- [26] M. J. Rossow, J. M. Sasaki, M. a Digman, and E. Gratton, “Raster image correlation spectroscopy in live cells.,” *Nat. Protoc.*, vol. 5, no. 11, pp. 1761–1774, 2010.
- [27] S. H. Gillespie and I. Balakrishnan, “Pathogenesis of pneumococcal infection,” *J. Med. Microbiol.*, vol. 49, pp. 1057–1067, 2000.
- [28] N. W. J. Schroder *et al.*, “Lipoteichoic Acid (LTA) of *Streptococcus pneumoniae* and *Staphylococcus aureus* Activates Immune Cells via Toll-like Receptor (TLR)-2, Lipopolysaccharide-binding Protein (LBP), and CD14, whereas TLR-4 and MD-2 Are Not Involved,” *J. Biol. Chem.*, vol. 278, no. 18, pp. 15587–15594, 2003.
- [29] E. Linehan, Y. Dombrowski, R. Snoddy, P. Fallon, A. Kissenpennig, and D. Fitzgerald, “Aging impairs peritoneal but not bone marrow-derived macrophage phagocytosis,” *Aging Cell*, vol. 13, pp. 699–708, 2014.
- [30] O. Kim *et al.*, “Impaired phagocytosis of apoptotic cells causes accumulation of bone marrow-derived macrophages in aged mice,” *BMB Rep.*, vol. 50, no. 1, pp. 43–48, 2017.
- [31] S. Kanno, A. Furuyama, and S. Hirano, “A murine scavenger receptor MARCO recognizes polystyrene nanoparticles,” *Toxicol Sci*, vol. 97, no. 2, pp. 398–406, 2007.
- [32] V. A. Fadok, D. L. Bratton, and P. M. Henson, “Phagocyte receptors for apoptotic cells: recognition, uptake, and consequences,” *J Clin Invest*, vol. 108, no. 7, pp. 957–962, 2001.
- [33] N. Thevaranjan *et al.*, “Age-Associated Microbial Dysbiosis Promotes Intestinal Permeability, Systemic Inflammation, and Macrophage Dysfunction,” *Cell Host Microbe*, vol. 21, no. 4, p. 455–466.e4, 2017.
- [34] D. Loukov, A. Naidoo, A. Puchta, J. L. A. Marin, and D. M. E. Bowdish, “Tumor necrosis factor drives increased splenic monopoiesis in old mice,” *J. Leukoc. Biol.*,

- vol. 100, no. 1, pp. 121–129, 2016.
- [35] R. S. Flannagan, R. E. Harrison, C. M. Yip, K. Jaqaman, and S. Grinstein, “Dynamic macrophage ‘probing’ is required for the efficient capture of phagocytic targets,” *J. Cell Biol.*, vol. 191, no. 6, pp. 1205–1218, 2010.
- [36] J. Lin *et al.*, “TIRF imaging of Fc gamma receptor microclusters dynamics and signaling on macrophages during frustrated phagocytosis.,” *BMC Immunol.*, vol. 17, no. 1, p. 5, 2016.
- [37] V. Jaumouillé, Y. Farkash, K. Jaqaman, R. Das, C. . Lowell, and S. Grinstein, “Actin cytoskeleton reorganization by Syk regulates Fc γ receptor responsiveness by increasing its lateral mobility and clustering,” *Dev. Cell*, vol. 29, no. 5, pp. 534–546, 2014.
- [38] S. A. Freeman *et al.*, “Transmembrane pickets connect cyto- and pericellular-skeletons forming barriers to receptor engagement,” *Cell*, vol. 172, no. 1–2, p. 305–317.e10, 2018.
- [39] et al. Jaqaman K, “Cytoskeletal control of CD36 diffusion promotes its receptor and signaling function.,” *Cell*, vol. 146, p. 593–606., 2011.
- [40] S. A. Freeman *et al.*, “Integrins Form an Expanding Diffusional Barrier that Coordinates Phagocytosis,” *Cell*, vol. 164, no. 0, pp. 128–140, 2016.
- [41] L. Weimann *et al.*, “A Quantitative Comparison of Single-Dye Tracking Analysis Tools Using Monte Carlo Simulations,” *PLoS One*, vol. 8, no. 5, p. e64287, 2013.

Chapter 5

Concluding Remarks

In this concluding chapter, the research findings are summarized and the future directions and potential avenues to explore the mechanisms of macrophage function and receptor mobility are proposed.

5.1 Summary and Conclusions

The aim of this work was to answer three major research questions regarding the lateral diffusion of two types of immunoreceptors in the plasma membrane of macrophages. The questions listed in Chapter 1, section 1.5 are divided into three main research areas: fluorescence microscopy techniques for capturing membrane dynamics, interactions of adhered macrophages with surface topographies, and functional changes in macrophages due to aging. Here, those questions are reviewed and the major findings are summarized:

1) What is the most appropriate technique to measure the lateral diffusion of receptors on macrophage plasma membranes? Do TLR2 and CD14 have significantly different diffusion coefficients? Is there significant difference in their diffusion in the apical and basal membrane sections for adhered macrophages?

As described in Chapter 2, we compared the diffusion coefficients of CD14 and TLR2 on the apical and basal membranes of macrophages using two common fluorescence-based methods: raster image correlation spectroscopy (RICS) and single-particle tracking (SPT). The diffusion coefficients obtained from SPT and RICS were similar for the basal membrane, and revealed significantly faster diffusion of CD14 compared with TLR2. In addition, RICS showed the diffusion of both receptors was significantly higher in the apical membrane than in the basal membrane, suggesting diffusion hindrance due to cell adhesion to the substrate. This finding highlights the importance of selecting the appropriate membrane when measuring receptor diffusion in live cells. While RICS enables the study of the diffusion in different regions of membranes and cross sections through the cell body, SPT is suitable for tracking the motions of individual membrane-inserted proteins only in the basal membrane.

2) How do micro- and nanostructured surfaces impact macrophages? Does diffusion of TLR2 in the plasma membrane and pro-inflammatory response change in macrophages adhered to surface topographies of different scale? Does surface topography alter macrophage morphology and phagocytic capacity?

The study presented in Chapter 3 aimed to investigate whether changes in the surface topography of glassy substrates alter macrophage shape, phagocytic function, inflammatory responses, and diffusion of membrane receptors. The morphology of

murine bone marrow derived macrophages cultured on micro- and nanostructured SiO₂ films was quantified through fractal analysis. We observed that membrane protrusions increased on nanostructured surfaces and macrophages adapted unique star-shaped morphologies on microstructured surfaces. Macrophages on both micro- and nanostructured surfaces displayed greater phagocytic capacity compared to those on flat controls. In contrast, their pro-inflammatory IL-6 secretion did not increase by substrate topographies of differing scale. Finally, the diffusion of TLR2 was measured using RICS, which revealed no impact of structuring or plasma treatment on receptor diffusion. These results suggest that surface topography does not alter macrophage inflammatory responses or membrane mobility but can significantly impact phagocytosis.

3) How does aging impact macrophage function? Does aging alter the lateral diffusion of TLR2 in the macrophage plasma membrane? Is there any significant difference in the phagocytic capacity of macrophages derived from young and aged mice?

The preliminary experiments included in Chapter 4 did not reveal any significant difference in macrophages derived from the bone marrow of young and aged mice. TLR2 diffusion rate in macrophages was comparable in the two age groups, and was significantly faster in both cases when measured after stimulation with *Streptococcus pneumoniae*. In addition, no significant difference was observed between the young and old groups with regard to phagocytosis of polystyrene beads and the bacteria *S. pneumoniae*; although, higher variation was evident in the number of beads internalized by macrophages from aged mice.

5.2 Future Directions

The work presented in this thesis has opened up new avenues for future studies on macrophages and immunoreceptors. Our findings have shown that accurate diffusion measurements of membrane receptors can help to answer different questions with regard to interactions of macrophages with biomaterials or bacteria.

In continuation of the work presented in Chapter 2, the field would benefit from simultaneous measurements of TLR2 and CD14 diffusion and their co-localization within the membrane using cross-correlation experiments with RICS and SPT, as described in Chapter 1 (section 1.2.3-4 and section 1.2.4). The addition of this

component could aid in understanding receptor interactions and would serve as a direct comparison of the imaging methods for monitoring co-localization events.

The study in Chapter 3 could be further expanded by investigation of cytoskeleton remodeling in macrophages adhered to surface topographies. Phagocytosis requires significant deformation in cell shape, and as a result the cytoskeleton plays a vital role in this process. To identify the precise molecular mechanisms that may impact the phagocytic ability of macrophages on certain surface topographies, direct measurement of actin filament and microtubule remodeling and their distribution in macrophages would be beneficial. In addition, the type of proteins adsorbed on different surfaces, their quantities and conformation all influence cell adhesion and behavior on a biomaterial surface which could alter phagocytosis.

To expand upon the basis established in Chapter 4 pertaining to identification of potential age-related changes in macrophage phenotype, future studies could aim to examine CD14 diffusion in relation to TLR2 function, given that CD14 is a coreceptor that plays a key role in TLR2 signaling in response to binding bacterial ligands. The biological context in which macrophages encounter bacteria such as *Streptococcus pneumoniae* is complex and involves pattern recognition receptors, phagocytic receptors, coreceptors, and cytokines among others. Therefore, further comparison of receptors' expression in macrophages from young and aged mice could shed light on possible mechanisms that may change macrophage inflammatory responses.

Supporting Information for Chapter 2

Search Radius Optimization for a Fixed Diffusion Coefficient

To determine the optimal search radius (SR) for track continuation in subsequent frames, different imaging and linking conditions were simulated and compared to the expected value of a restricted Gaussian step size distribution. For both simulation and theoretical considerations two diffusion coefficients of $D = 0.1 \mu\text{m}^2 \text{ s}^{-1}$ and $D = 0.15 \mu\text{m}^2 \text{ s}^{-1}$ was assumed. The pixel size of $0.1 \mu\text{m}$ and frame interval of $\tau = 60 \text{ ms}$ was kept constant.

To arrive at the expected value, 10^6 displacements (x_i, y_i) were sampled from a Gaussian distribution with zero mean and a variance of $2D\tau$ and restricted by a search radius $r_{\text{SR}} \geq \sqrt{x_i^2 + y_i^2}$. The accepted displacements were combined into a master track and the diffusion coefficient was obtained via a linear mean-squared displacement fit.

To see the dependence of the measured diffusion coefficient on the search radius, simulations for particle concentrations of $0.031 \mu\text{m}^{-2}$, $0.092 \mu\text{m}^{-2}$ and $0.153 \mu\text{m}^{-2}$ were created with continuous tracks, as well as emission state switching tracks to emulate blinking. Continuous tracks were created for negligible noise ($S/N > 700$), as well as a signal-to-noise ratio of 1.7. When blinking was active, the switching probabilities were chosen to be $p_{\text{on}} = 0.3$ and $p_{\text{off}} = 0.1$. All simulated videos had a length of 1000 frames. The videos were analyzed with the in-house single-particle-tracking algorithm [1] and the search radius was varied from 0.5 px to 10 px.

Introduction

When tracking a single particle in time, the algorithm will search for a particle within a similar location in subsequent frames. The location is defined as a circle of radius r_{SR} (Search Radius) centered on the previous particle localization. The choice of r_{SR} is crucial for an unbiased analysis. Confining the search area can be beneficial for analysis time, but can lead to premature track termination and lower measured diffusion coefficient values. For unreasonably large r_{SR} a particle that has terminated, *e.g.* due to photobleaching, might falsely be linked to another particle and bias the measured diffusion coefficient to larger values. Optimizing r_{SR} is therefore a requirement for valid diffusion coefficient

measurement.

Theory

Limiting the linking process with r_{SR} is in effect removing the tail ends of the Gaussian step size distribution for each displacement coordinate. To recreate this, 10^6 displacements $\vec{r}_j = (\Delta x_j, \Delta y_j)$ are sampled component-wise from a 1D Gaussian distribution of shape

$$\Theta[\Delta x_j] = \exp\left\{-\frac{\Delta x_j^2}{4D\tau}\right\}. \quad (1)$$

The introduction of r_{SR} represents a restriction of the displacements of $r_{SR}^2 \geq r_k^2$. Displacements that follow this restriction are then combined into a master track by appending displacements $\vec{r}(t|r_{SR}) = \sum_{k=1}^{t \leq k \cdot \tau} \vec{r}_k$. The resulting diffusion coefficient can be obtained from a linear MSD fit to the master track data

$$\langle \vec{\Delta r}^2(t) \rangle = \langle (\vec{r}(k\tau + t) - \vec{r}(k\tau))^2 \rangle_k = 4D_{SR}t. \quad (2)$$

Simulation

Videos were simulated by creating particle tracks for N particles with K steps for the diffusion coefficient D and step interval τ . The particle position in frame k of the video is given by

$$\vec{r}_n(k, \tau) = \vec{r}_n((k-1)\tau) + \Delta \vec{r}(D, \tau), \quad (3)$$

with components of $\Delta \vec{r}$ taken from (1).

Each image was created by adding the intensities of all visible N particles for each pixel.

$$I(\vec{r}_{px}) = \sum_{n=1}^N I_G(\vec{r}_n - \vec{r}_{px}) + B_{Gauss}(\vec{r}_{px}), \quad (4)$$

with the diffraction limited spot intensity

$$I_G(\vec{\Delta r}) = \exp\left\{-\frac{\vec{\Delta r}^2}{2\sigma^2}\right\}, \quad (5)$$

and a Gaussian background noise B_{Gauss} with a global average background intensity of B ,

a standard deviation σ_B of and a resulting distribution

$$\Phi[B_{Gauss}] = \frac{1}{\sqrt{4\pi\sigma_B^2}} \exp\left\{-\frac{(B_{Gauss}-B)^2}{2\sigma_B^2}\right\}. \quad (6)$$

The resulting images $I(\vec{r}_{px})$ were then converted to 16-bit integer values $i_{x,y}$ and modulated with Poisson noise resulting in the output image $j_{x,y}$ with distribution

$$\Psi[j_{x,y}] = e^{-i_{x,y}} \frac{(i_{x,y})^{j_{x,y}}}{j_{x,y}!}. \quad (7)$$

The signal-to-noise ratio is determined as the ratio of the squared signal and the background intensity variance. With the definition of the signal being the difference of average particle intensity value and the average background $S = I - B$

$$\frac{S}{N} = \frac{S^2}{\sigma_B^2} = \frac{(I_{av}-B)^2}{\sigma_B^2} \quad (8)$$

To reproduce the blinking behavior observed in fluorescence experiments, particles were given the ability to switch ‘on’ and ‘off’ with probabilities $p_{on} = 0.3$ and $p_{off} = 0.1$, respectively. The implementation sees the particles state described as an additional Markov chain of Boolean values $s_n(t)$, with $s_n(t)=1$ representing the ‘on’ state. This is a simple modification of (4) with the Markov chain

$$I(\vec{r}_{px}, t) = \sum_{n=1}^N I_G(\vec{r}_n(t) - \vec{r}_{px}) \cdot s_n(t) + B_{Gauss}(\vec{r}_{px}). \quad (9)$$

Simulation Setup and Considered Conditions

For all further considerations the pixel size of $0.1 \mu\text{m}$ and the frame interval of $\tau = 60 \text{ ms}$, as well as the assumed diffusion coefficient $D = 0.1 \mu\text{m}^2/\text{s}$, were kept constant.

In total, the simulation was carried out for nine situations. Each scenario of a continuous track with negligible noise ($I_{av} = 3000$, $B = 300$, $\sigma_B = 100$), a continuous track with $S/N \approx 1.7$ ($I_{av} = 3000$, $B = 1000$, $\sigma_B = 1500$) and a track with blinking and negligible noise was carried out for three particle concentrations of $0.031 \mu\text{m}^{-2}$ ($N = 20$ particles per 256×256 pixel), $0.092 \mu\text{m}^{-2}$ ($N = 60$ particles per 256×256 pixel), and $0.153 \mu\text{m}^{-2}$ ($N = 100$ particles per 256×256 pixel).

Detection and Tracking

The simulated data is detected and tracked using our in-house algorithms (Source: <https://github.com/MarkusRose/ParticleTracker>).

Each data set brings 5 observables: Number of Tracks (Num) (figure X) , Length of tracks (Len) (figure X), Diffusion coefficient of individual tracks via MSD (Dindiv) (figure X), Diffusion coefficient of the combined track via MSD (D) (figure X), and Diffusion coefficient of the combined track through Gaussian step size distribution (Dstep) (figure X). [1] <https://github.com/MarkusRose/ParticleTracker>

Simulation results for $D = 0.1 \mu\text{m}^2 \text{s}^{-1}$

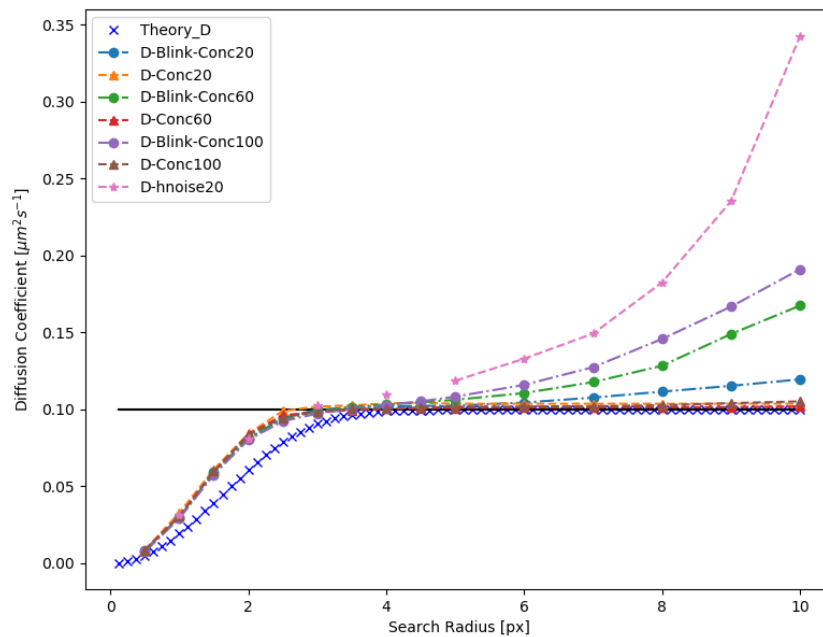


Figure S2.1 Simulation results showing the change in the diffusion coefficient obtained from MSD of combined tracks for a range of search radii.

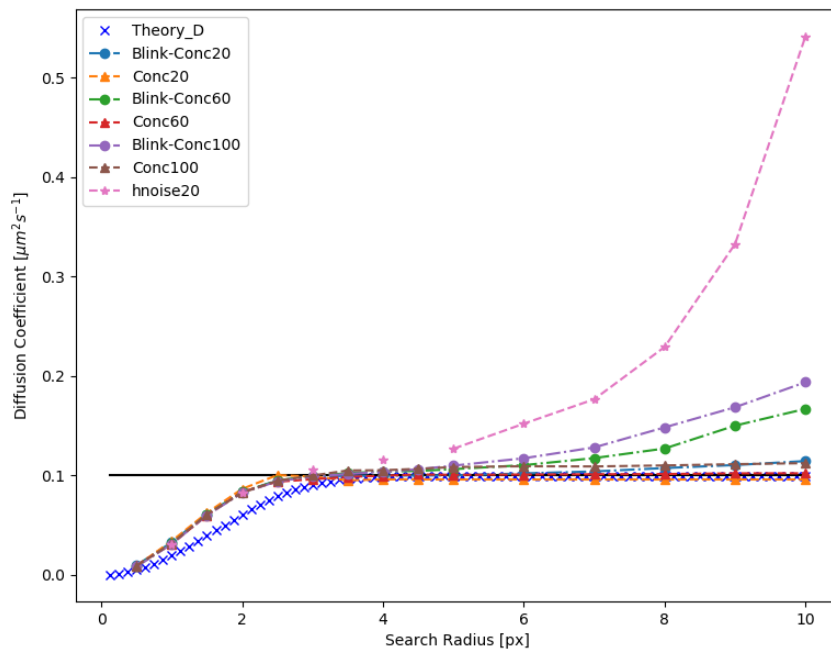


Figure S2.2 Simulation results showing the change in the diffusion coefficient obtained from MSD of individual tracks for a range of search radii.

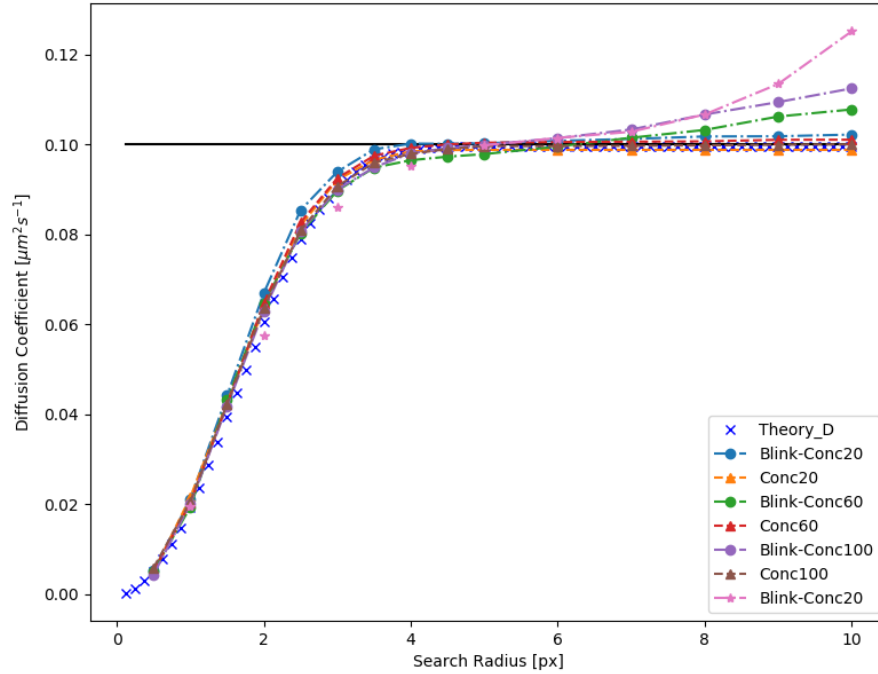


Figure S2.3 Simulation results showing the change in the diffusion coefficient obtained from step-size distribution for a range of search radii.

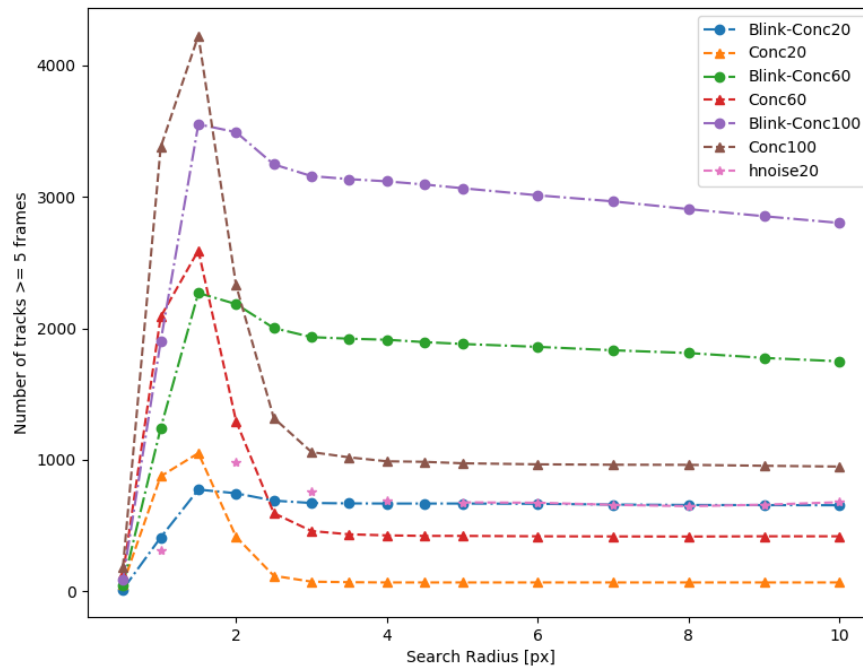


Figure S2.4 Simulation results showing the change in the number of generated tracks for a range of search radii.

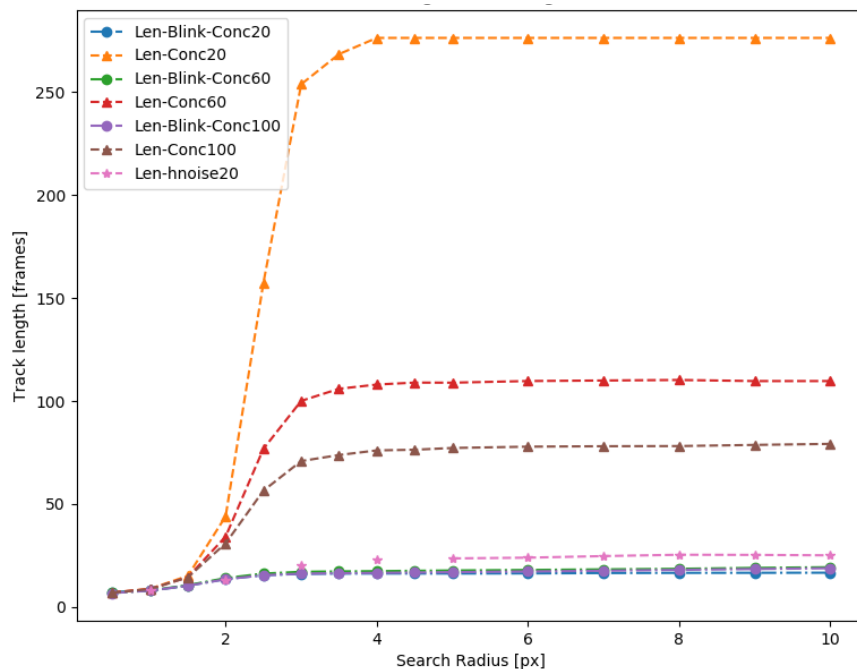


Figure S2.5 Simulation results showing the change in the average track length for a range of search radii.

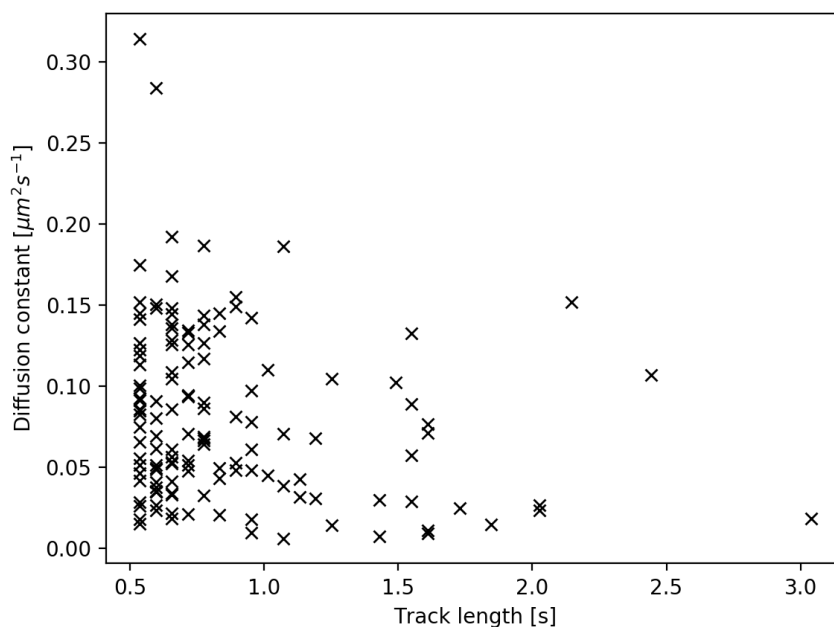


Figure S2.6 Dependence of measured diffusion on track length. The diffusion coefficients and track lengths for individual tracks obtained from tracking TLR2 in RAW 264.7 (cell shown in Figure 2.1A) do not show any correlation.

Supporting Information for Chapter 3

Atomic Force Microscopy

Atomic force microscopy (AFM) was used to measure the topography and surface roughness of 50 nm flat SiO₂ substrates. Measurements were performed using an Asylum MFP-3D AFM (Asylum Research, an Oxford Instrument Company, Santa Barbara, CA, USA). Images were collected in alternating current (AC) tapping mode under ambient conditions using rectangular NCHR cantilevers (NanoWorld, force constant 21-78 N/m, resonant frequency 250-390 kHz). Image analysis was performed and root-mean-squared (rms) roughness was calculated using Asylum Research AFM software (version 13.17).

Supplemental Figures

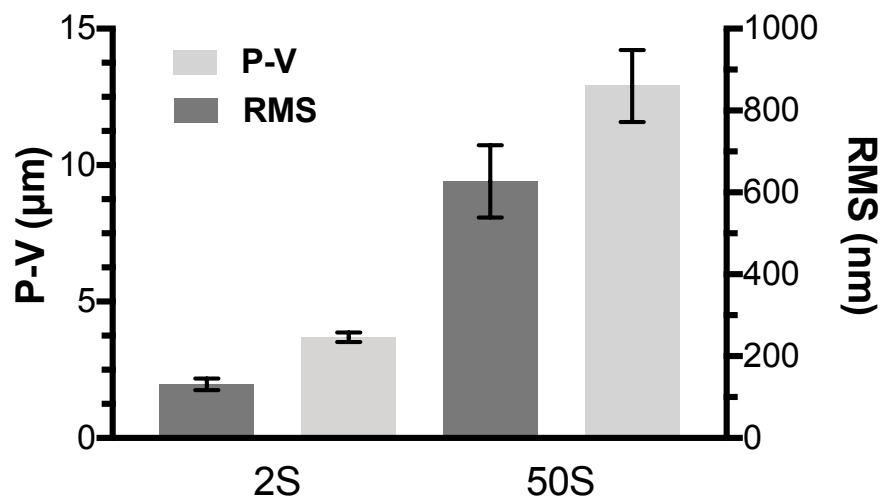


Figure S3.1 Surface roughness characterization of structured SiO₂ substrates with white light interferometry microscopy (WLIM). Peak-to-valley (P-V) and root mean square (RMS) roughness of structured SiO₂ films of varying thicknesses illustrating range of height data. Bars represent means and error bars represent the standard deviation of nine measurements on three independently prepared replicates.

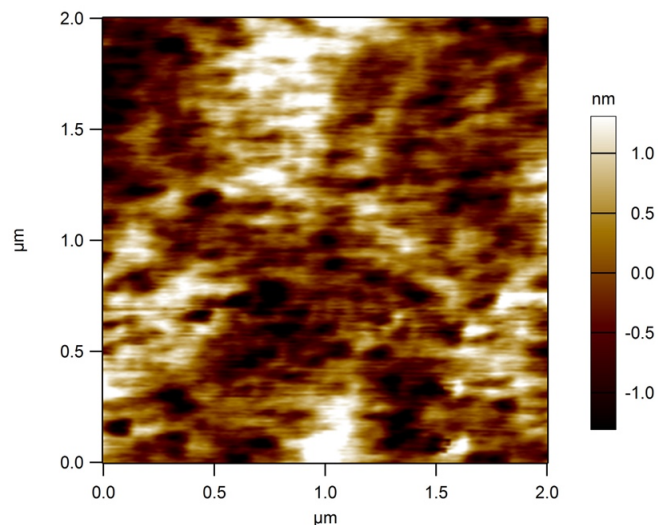


Figure S3.2 Representative atomic force microscopy image of flat 50 nm SiO₂ film. RMS roughness values calculated from AFM measurements on three replicate samples were 0.657 ± 0.008 nm

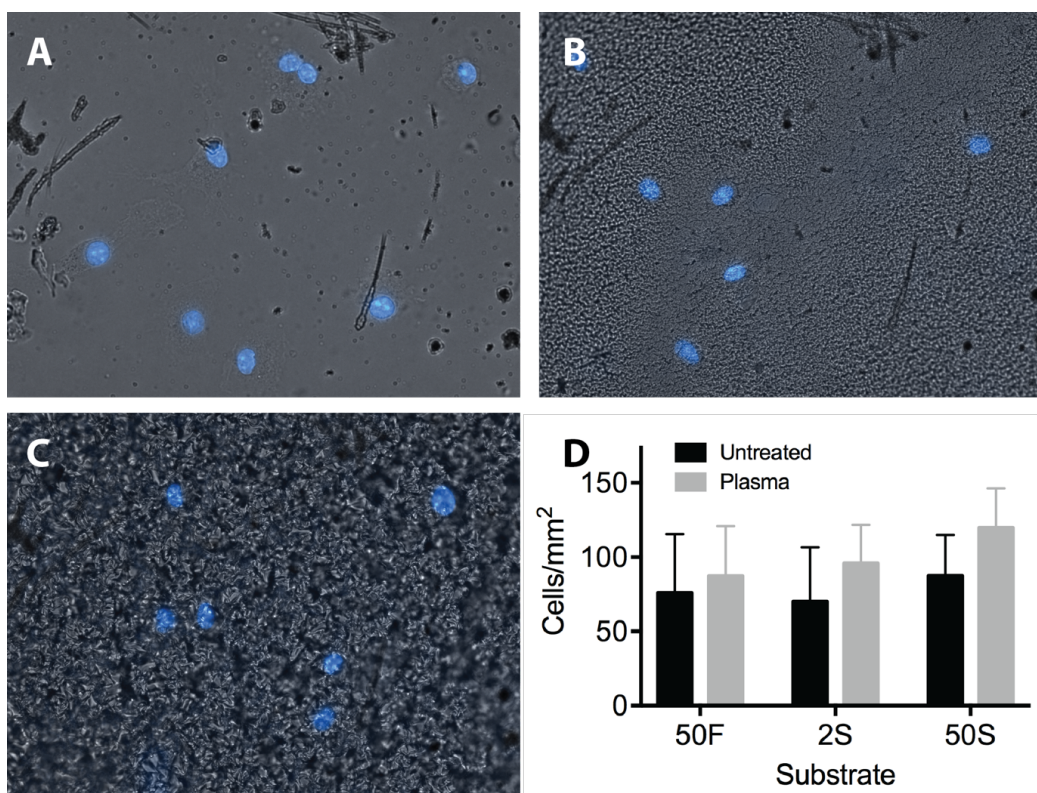


Figure S3.3 Quantification of cell adhesion to SiO₂ substrates. Overlay of brightfield and fluorescence (DAPI stained nuclei) for cells cultured on untreated (A) 50 nm flat, (B) 2 nm structured and (C) 50 nm structured SiO₂ surfaces. (D) Comparison of the density of macrophages adhered to untreated and plasma treated 50 nm flat SiO₂ (50F), 2 nm structured SiO₂ films (2S), and 50 nm structured SiO₂ films (50S). Images (A), (B), and (C) taken at the same magnification, with a field of view 200 μ m across.

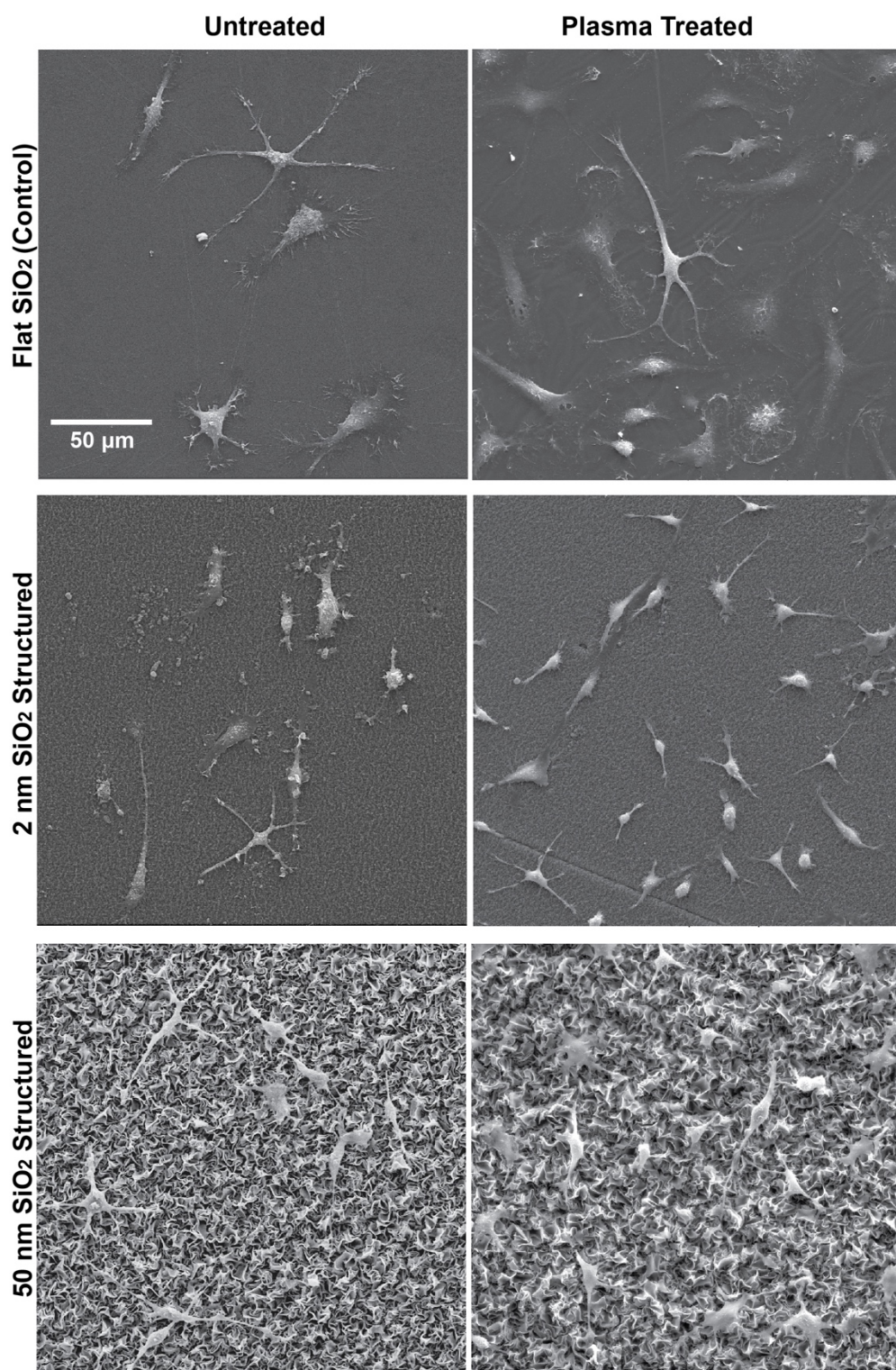


Figure S3.4 Representative SEM images of macrophages on SiO₂ substrates with different surface topographies, in the absence of surface treatment vs. plasma treated condition.

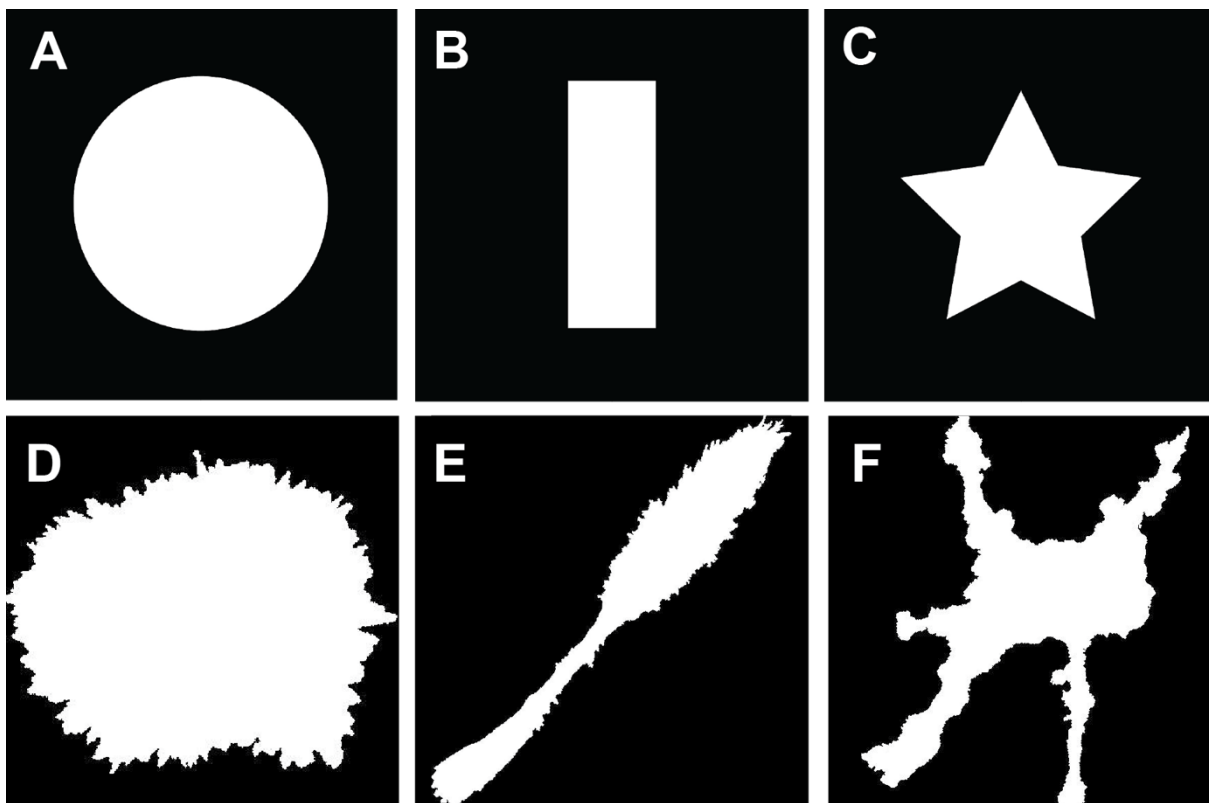


Figure S3.5 Six geometries of different complexities – circle, rectangle, star, “fried-egg” cell, “elongated” cell, and “star-shaped” cell – analyzed with box-counting method for fractal analysis, yield fractal dimension area (FDA) values of (A) 1.926 (B) 1.898, (C) 1.861, (D) 1.891, (E) 1.816, and (F) 1.767; and fractal dimension perimeter (FDP) values of (A) 0.996, (B) 0.999, (C) 1.003, (D) 1.137, (E) 1.096, and (F) 1.087.

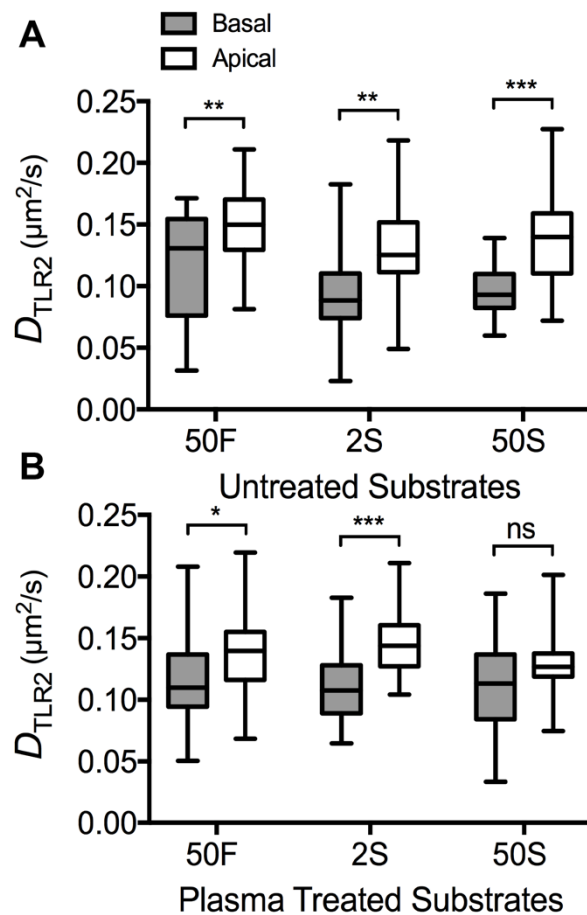


Figure S3.6 Lateral diffusion of TLR2 on the apical and basal membranes of macrophages on (A) untreated and (B) plasma treated 50 nm flat SiO₂ (50F), 2 nm structured SiO₂ films (2S), and 50 nm structured SiO₂ films (50S). Statistical significance was determined from paired *t*-test with 95% confidence interval (**P* ≤ 0.05, ***P* ≤ 0.01, ****P* ≤ 0.001).

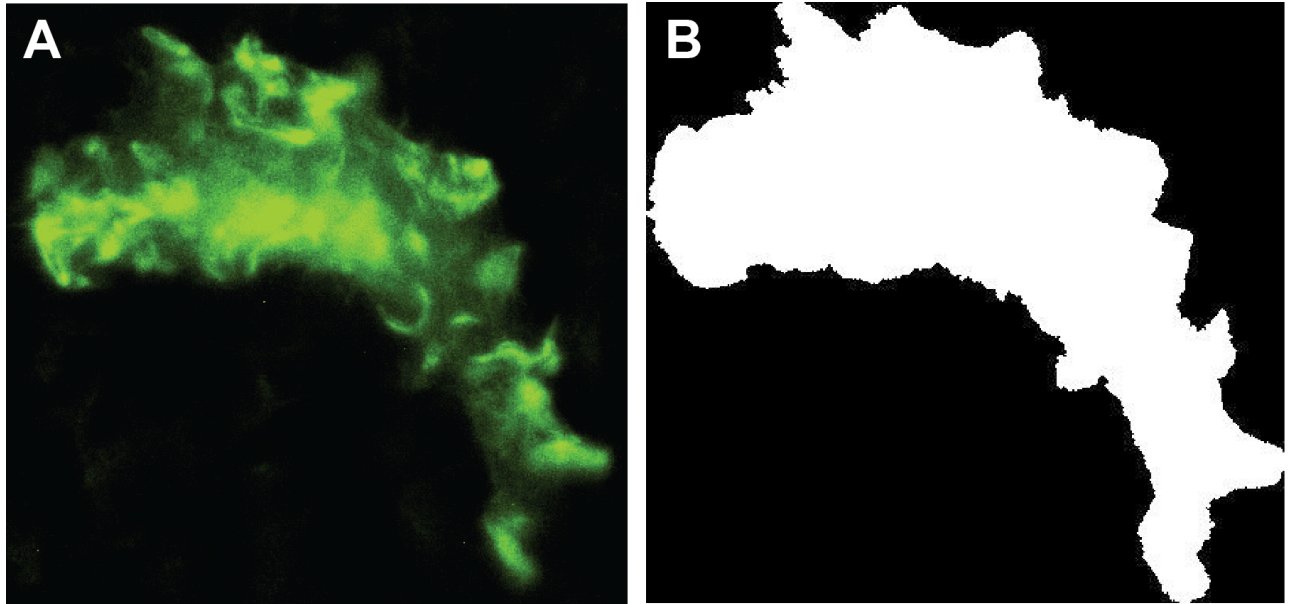


Figure S3.7 Representative (A) epifluorescence image of a bone marrow derived macrophage cultured on 50 nm structured SiO₂ substrate, and (B) binary image used for fractal analysis.

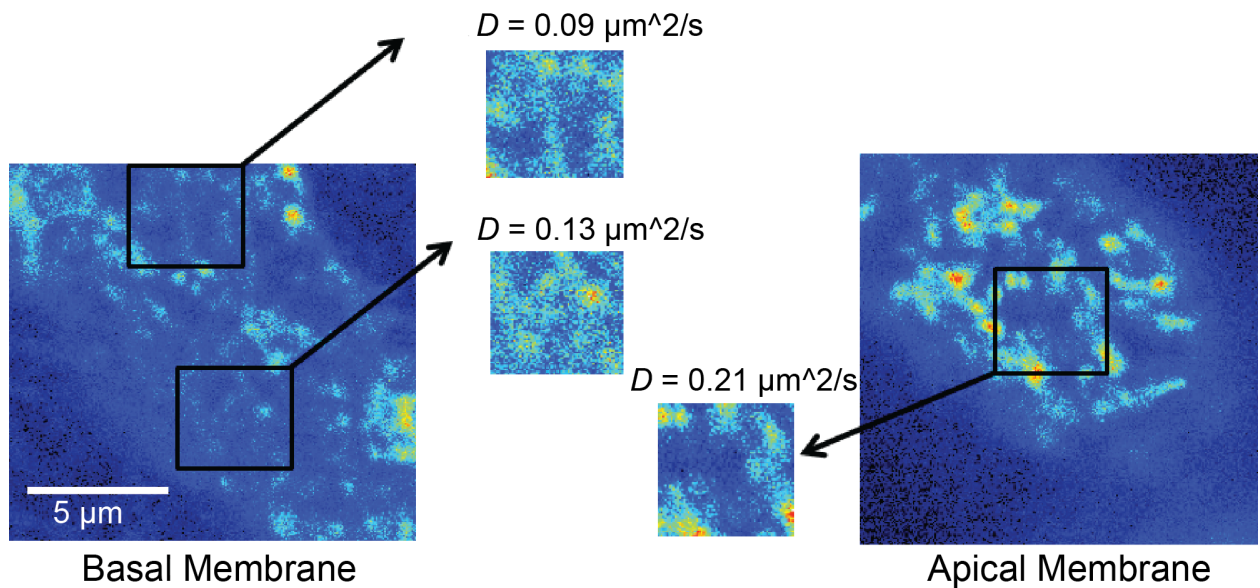


Figure S3.8 Confocal microscopy image of the basal and apical membranes of a macrophage expressing TLR2 receptors. 64×64 pixel frames show the regions of interest and the diffusion coefficient corresponding to each region as calculated through RICS. Images taken with conditions used for RICS measurements.

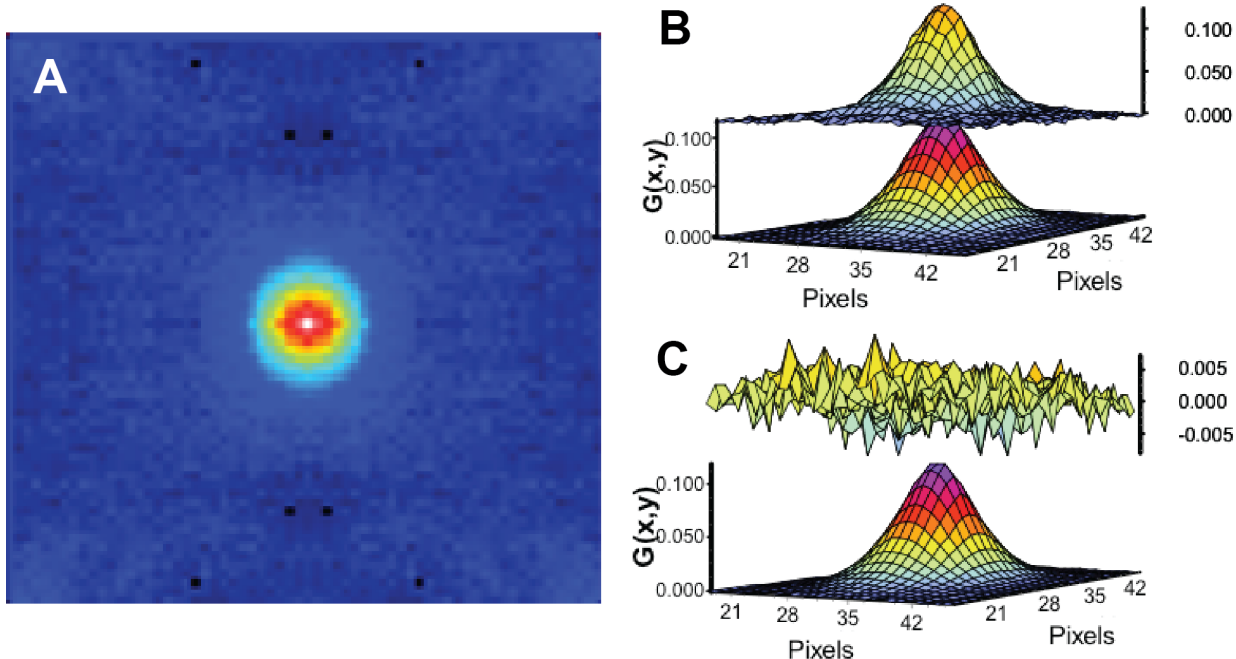


Figure S3.9 Diffusion measurement of TLR2 on a macrophage plasma membrane using RICS analysis. (A) 2D representation of RICS autocorrelation function, (B) plot of the data (upper surface) and 3D representation of the fit to the function (lower surface), (C) plot of the residues (upper surface) and the fit (lower surface).